Analysis of Hydrodynamic Transport Phenomena in a Fluidized Bed for Thermochemical Hydrogen Production

by

Yousef Haseli

A Thesis Submitted in Partial Fulfillment
of the Requirements for the Degree of

Master of Applied Science

in

The Faculty of Engineering and Applied Science

Program: **Mechanical Engineering**

University of Ontario Institute of Technology

April 2008

ABSTRACT

This thesis examines transport phenomena involving the reaction of cupric chloride ($CuCl_2$) particles and superheated steam within a fluidized bed as part of a thermochemical hydrogen production plant. The study is carried out by performing hydrodynamics and mass transport analysis. This is necessary for analyzing the mass transport of the reaction in a fluidized bed. In the first part, the effects of superficial velocity, bed inventory, particle diameter and spherecity on bed height, average bubble diameter and bed voidage are investigated through a newly developed solution procedure. In the second step, the conversion of steam as a fluidizing gas and conversion of $CuCl_2$ are numerically investigated using a new non-catalytic gas-solid reaction model, proposed in past literature but here updated for the purposes of the present study. The results are illustrated considering two cases of kinetics for the consumption of particles: Volumetric Model (VM) and Shrinking Core Model (SCM). Consistent results in terms of the conversion of reactants versus superficial velocity, bed inventory and bed temperature are obtained by developing new solution algorithms based on each of the above kinetic models. The methodology presented in this thesis will be useful in feature research when building an experimental apparatus and estimating the optimal values of reactor parameters.

Keywords: Cupric chloride, steam, fluidized bed, transport phenomena, hydrodynamics, mass transport, chemical reaction

Acknowledgments

The author wishes to gratefully acknowledge with appreciation the guidance of his co-supervisors, *Prof. Ibrahim Dincer* and *Prof. Greg F. Naterer* who were always advising the author warmly in the present thesis work. In particular, the author would like to express his best appreciation to his co-supervisors for providing him this precious opportunity to contribute in such a significant research project.

Also, the support of the library staff at the University of Ontario Institute of Technology (UOIT) is greatly appreciated for providing the required materials including research papers and textbooks from interlibrary loans.

Financial support of this research from Atomic Energy of Canada Ltd. (AECL) and the Ontario Research Excellence Fund is gratefully acknowledged.

March 2008 **Yousef Haseli**

Contents

List of Tables

List of Figures

Nomenclature

$A_{c,bed}$	Bed cross-sectional area, m^2
Ar	Archimedes number
b	Stoichiometric factor of the reaction
$\bar{c}_p$	Molar specific heat, kJ/kmole.K
C_A	Gaseous reactant concentration, mole/m^3
C_{Ab}	Gaseous reactant concentration in bubble phase, mole/m^3
C_{Ac}	Gaseous reactant concentration in cloud region, mole/m^3
C_{Ae}	Gaseous reactant concentration in emulsion phase, mole/m^3
C_{Ai}	Inlet gaseous reactant concentration, mole/m^3
C_{Ao}	Outlet gaseous reactant concentration, mole/m^3
d_b	Bubble diameter, m
d_{b0}	Initial bubble diameter, m
$d_{b,ave}$	Average bubble diameter, m
d_{bm}	Maximum bubble diameter, m
d_p	Particle mean diameter, m
d_p^*	Dimensionless particle diameter, Eq. (2-3)
Da_s	Damkohler number at reactor scale, Eq. (3-39)
D_g	Gas diffusivity, m^2/s
D_t	Bed diameter, m
f	Function
$f_1(x_{c0},\lambda)$	Function defined in Eq. (3-47)
$f_2(x_{c0},\lambda)$	Function defined in Eq. (4-14)
$F_i(x_c)$	Kinetic function, Table 3.1
F_0	Inlet flow rate of solids, kg/s
F_1	Outlet flow rate of solids, kg/s
g	Acceleration of gravity, 9.81m/s

$\Delta\overline{G}$	Molar Gibbs free energy of reaction, kJ/kmole
$\overline{H}_T$	Molar enthalpy of formation, kJ/kmole
K_{bc}	Coefficient of gas interchange between bubble and emulsion, 1/s
K_{be}	Overall coefficient of gas interchange between bubble and emulsion, 1/s
K_{ce}	Coefficient of gas interchange between cloud-wake and emulsion, 1/s
K_f	Overall rate constant for a first order chemical reaction, 1/s
K_r	Rate constant for a first order catalytic reaction, 1/s
$K_{r,e}$	Kinetic coefficient defined in Eq. (3-42), 1/s
l_{or}	Spacing between adjacent holes on the distributor, m
L_f	Bed height, m
L_m	Packed bed height, m
L_{mf}	Bed height at minimum fluidization conditions, m
M_p	Molecular mass of solid reactant (kg/kgmol)
n	Order of reaction, Number of moles
N_a	Concentration efficiency, Eq. (3-32)
NTU	Number of Transfer Unit, Eq. (3-33)
N_{or}	Hole density of the distributor, m^{-2}
$p_b(x_c)$	Distribution of conversion in the bed
ΔP_b	Pressure drop across the bed, Pa
$r_{c,bed}$	Overall rate of reaction in the bed defined in Eq. (3-43), kg/s
$R(x_c)$	Reactivity of solid reactant defined in Eq. (3-44), 1/s
Re_{mf}	Reynolds number at minimum fluidization condition
Re_p	Particle Reynolds number
S	Slack variable
$\overline{S}_T$	Molar entropy of formation, kJ/kmole, K
T	Temperature, K
U^*	Dimensionless velocity, Eq. (2-4)
U_o	Superficial gas velocity, m/s
U_b	Velocity of bubble, m/s
U_b^*	Velocity of bubble defined in Eq. (3-20), m/s

U_{br}	Relative velocity of bubble, m/s
U_c, U_k	A transition velocity between bubbling and turbulent fluidization regimes, m/s
U_{mb}	Minimum bubbling velocity, m/s
U_{mf}	Minimum fluidized velocity, m/s
U_{ms}	Minimum slugging velocity, m/s
U_{tr}	A transition velocity between turbulent and fast fluidization regimes, m/s
W_b	Bed inventory, kg
x_c	Conversion of solid reactant in a particle
x_{c0}	Conversion of solid reactant in a particle at inlet condition
$x_{c,b}$	Average conversion of solids in the bed
X	Slack variable
X_A	Gaseous reactant conversion
X_B	Solids reactant conversion
X_g	Gas conversion
Y_{c0}	Mass fraction of solid reactant in the feed
$Y_{c,b}$	Mass fraction of solid reactant in the bed
z	Axial coordinate

Greek letters

α	Ratio of diameter of the wake to the diameter of the bubble introduced in Eq. (3-8), or dimensionless parameter at reactor level, Eq. (3-49)
β	Dimensionless excess of flow, Eq. (3-35)
γ_b	Volume of solids dispersed in bubble phase
γ_c	Volume of solids dispersed in cloud-wake region, Eq. (3-8)
γ_e	Volume of solids dispersed in emulsion phase, Eq. (3-9)
δ	Bubble fraction in a fluidized bed, Eq. (3-9)
ε_b	Bed void fraction
ε_{mf}	Bed void fraction at minimum fluidization conditions
η_{bed}	Bed effectiveness
η_p	Particle effectiveness factor

η_{ph}	Inter-phase effectiveness factor, Eq. (3-30)
$\Theta(x_c)$	Function defined in Eq. (3-38)
λ	Dimensionless factor defined in Eq. (3-40)
μ_g	Gas viscosity, Pa/s
ζ	Convergence criteria in Figs. 4.5-4.7
ρ_g	Gas density, kgm^{-3}
ρ_p	Particle density, kgm^{-3}
τ	Time needed for complete conversion of solid particle, s
φ	Particle sphericity

Chapter 1

Introduction

Currently the world consumes about 85 million barrels of oil and 104 trillion cubic feet of natural gas per day, releasing greenhouse gases that lead to global warming. Unlike fossil fuels, hydrogen is a sustainable and clean energy carrier, which is widely believed to be the world's next-generation fuel. Hydrogen demand is expected to rise dramatically over the next few decades. The worldwide hydrogen market is currently valued at over $282 billion/year, growing at 10%/year, rising to between 20-40%/year by 2020 and anticipated to reach several $trillions by 2020. Dincer [1] has outlined many of the key technical and environmental concerns of current methods of hydrogen production. There is a wide range of hydrogen production technology that can be classified as: hydrocarbon-based methods, e. g. coal gasification or steam-methane reforming (SMR), non-hydrocarbon-based methods, e. g. water electrolysis and thermochemical water decomposition, and integrated methods such as SMR linked to non-hydrocarbon-based processes [2].

1.1 LITERATURE SURVEY

The predominant existing process for large-scale hydrogen production is SMR. SMR is a carbon-based technology that emits a primary greenhouse gas (carbon dioxide). In contrast, nuclear-based hydrogen production does not emit greenhouse gases. Nuclear energy can be supplied abundantly for large-scale capacities of hydrogen production [3]. It can be used for hydrogen production in three main ways [4]:

- Using electricity from the nuclear plant for conventional liquid electrolysis;
- Using both high-temperature heat and electricity from the nuclear plant for high-temperature steam electrolysis or hybrid processes;
- Using heat from the nuclear plant for thermochemical processes.

Thermochemical "water splitting" requires an intermediate heat exchanger between the nuclear reactor and hydrogen plant, which transfers heat from the reactor coolant to the thermochemical cycle [5]. Operating temperatures are key factors for thermochemical methods of hydrogen production. Thus, optimization of heat flows is important for high energy conversion efficiency [6]. Energy efficiency is important for providing hydrogen economically in an environmentally friendly manner. High operating temperatures are needed for more efficient thermochemical and electrochemical hydrogen production using nuclear energy. Therefore, high-temperature reactors, such as gas-cooled, molten-salt-cooled and liquid-metal-cooled reactor technologies, are candidates for use in hydrogen production [4]. Several candidate technologies that span the range from well developed to conceptual were compared by Yildiz and Kazimi [4]. They concluded that high-temperature steam electrolysis (HTSE) coupled to an advanced gas reactor cooled by supercritical CO_2 (S-CO_2) and equipped with a supercritical CO_2 power conversion cycle has promising potential to provide higher energy efficiency at a lower temperature range than other alternatives.

Many types of thermochemical processes exist for hydrogen production. The Sulfur-Iodine (SI) cycle (hydrogen sulfide, iodine–sulfur, sulfuric acid–methanol) and the Br–Ca–Fe cycle are leading candidates [7]. A Literature review indicates that Japan and the USA have been leading the thermochemical hydrogen production developments through SI cycle proposed by General Atomics in the mid-1970s. This consists of the following three chemical reactions which yield the dissociation of water [4]:

$$I_2 + SO_2 + 2H_2O \rightarrow 2HI + H_2SO_4 \ (120\ ^{\circ}C) \quad (1\text{-}1)$$

$$H_2SO_4 \rightarrow SO_2 + H_2O + 1/2O_2 \ (830\text{-}900\ ^{\circ}C) \quad (1\text{-}2)$$

$$2HI \rightarrow I_2 + H_2 \ (300\text{-}450\ ^{\circ}C) \quad (1\text{-}3)$$

For the advanced methods of hydrogen generation using nuclear power, thermochemical cycles have received the most attention because current estimates indicate that thermochemical H_2 production costs could be as low as 60% of those from room-temperature electrolysis [7].

1.1.1 Past Developments in Japan

The Japan Atomic Energy Research Institute (JAERI) has been conducting R&D on thermochemical hydrogen production with the water-splitting SI process, as part of the research to utilize heat from a high temperature gas-cooled reactor (HTGR). Kasahara et al. [8] investigated the thermal efficiency of the S-I thermochemical cycle. The heat and mass balances of the process were calculated with various operating conditions and the effects of these conditions on the thermal efficiency were evaluated. They developed an electro-electrodialysis (EED) cell for the concentration of HI and a hydrogen permselective membrane reactor for decomposition of HI. Sensitivities of four operating conditions (the HI conversion ratio in the HI decomposition reactor, the reflux ratio in the HI distillation column, the pressure in the HI distillation column, and the concentration of HI after the EED cell) were investigated. The concentration of HI had the most significant effect on thermal efficiency. The difference of the efficiency was 13.3%. Other conditions had little effects, within 2% of the efficiency. Effects of non-ideal conditions in the process were evaluated. The difference of efficiencies due to the loss in the EED cell was 11.4%. The efficiency decreased by 5.7%, due to losses in heat exchangers. The loss during waste heat recovery lowered the efficiency by 6.3%. They reported a maximum thermal efficiency of 56.8% for the S-I process to produce hydrogen after optimization of various parts of the cycle.

Kasahara et al. [9] investigated effects of operation parameters of HI synthesis and concentration procedures on the thermal efficiency in S-I process, based on heat/mass balances. The concentration of HI was carried out by an electro-electrodialysis (EED) cell. The transport number of protons, electroosmosis coefficient and ratio of the flow rates at the inlets of the EED cell were considered as parameters of the EED cell, in different over-potential and temperature differences in the heat exchangers. The parameters of the EED cell had little effect on the thermal efficiency at optimized over-potential and temperature differences. The relation between these parameters and thermal efficiency was dependent on the over-potential and temperature difference. The composition of the solution produced in the HI synthesis procedure influenced the thermal efficiency significantly. Higher thermal efficiency was obtained at low I_2 concentrations and high HI concentrations.

Nomura and co-workers [10] successfully employed the Bunsen reaction ($SO_2 + I_2 + 2H_2O = H_2SO_4 + 2HI$) in the thermochemical S-I process to produce hydrogen using an electrochemical membrane reactor. H_2SO_4 and HI were concentrated in the anode side and cathode side of the reactor, respectively. I_2 was the dominant fluid in the recycling chemicals in this process. The I_2 concentration at the outlet of the reactor was reduced 93% by using this technique. The electric energy consumption for the reaction was about 50% smaller when reducing the concentration of I_2, indicating that the S-I process can be operated more efficiently at low I_2 concentrations. The reaction was carried out for 4 hours and the HI concentration was increased by 26%. This amount was within 10% of the values calculated from the total loaded electricity. In order to decrease the over-potential at the anode side, a small amount of HI was added to the anode side solution. The total voltage was reduced by 0.03V by the addition of HI.

Kubo et al. [11] performed a demonstration study by operating an experimental facility made of glass and fluorine resin for a closed-loop process of continuous hydrogen production. In the experiment, hydrogen production at the rate of 32 l/h for 20 hours was successfully accomplished. Feasibility of the operating stability was almost demonstrated.

Nomura et al. [12] evaluated the effects of three typical membrane techniques (electro-electrodialysis (EED), an electrochemical cell (EC) and a hydrogen

permselective membrane reactor (HPMR)) on the total thermal efficiency by heat/mass balance calculations based on the experimental data. The EED to concentrate an HI solution was found to be the most important membrane technique to obtain a high thermal efficiency, among the three techniques. The maximum thermal efficiency was 40.8% at 12.5 mol/kg_{H2O} of HI molality after the EED. The second important technique was the EC for the reaction of H_2O, SO_2 and I_2. The maximum thermal efficiency was 38.9% at 15.3 mol/kgH_{2O} of H_2SO_4 molality after the EC. The HPMR of the decomposition reaction of HI was sufficiently effective to improve one-pass conversion of HI to 76.4%. The amount of recycled HI was reduced by 91.5% using this membrane technique. The required heat for the reactor was small compared with that of the EED or at the EC. The total thermal efficiency was improved only 0.7% by the application of the HPMR.

The Bunsen reaction was examined by an electrochemical cell, with a cation exchange membrane as the separator, by Nomura et al. [13]. The optimal molalities of the anolyte and catholyte were evaluated by the total thermal efficiency, using the heat/mass balance of the SI process. The I_2/HI ratio could be reduced to 0.5 without decreasing the total thermal efficiency. On the other hand, the HI and H_2SO_4 molality greatly affected the total thermal efficiency. The total thermal efficiency increased when increasing the HI molality up to 16.7 mol/kg_{H2O} and the maximum thermal efficiency was found at 15.3 mol/kg_{H2O} of H_2SO_4. The total thermal efficiency increased by 3.0% at a current density of the electrochemical cell of 10.0Adm^{-2} by increasing the operating temperature from 313 to 363 K.

In a study by Kasahara et al. [14], a sensitivity analysis of the operation parameters and the chemical properties in the iodine-sulfur process was carried out for a static flow sheet. These parameters were evaluated by the hydrogen production thermal efficiency, mass flow rate or heat exchange, based on the heat/mass balance. The most important parameters were the concentration of HI after electro-electrodialysis (EED) and the apparent transport number of protons of the cation exchange membrane in the EED cell. For the chemical properties, fluid composition at the inlet of the HI decomposition procedure and HI pseudoazeotropic composition had significant effects.

The conceptual design of the S-I system using heat from Japan's first high-temperature gas-cooled reactor HTTR, and the thermal efficiency for the hydrogen production were evaluated in a recent study of Sakaba et al. [15]. A thermal efficiency of over 40 % and hydrogen production rate of 1,100 Nm^3/h were shown by the flowsheet evaluation of the HTTR-IS system. They showed the HTTR-IS system as the world first water-splitting hydrogen production demonstration by using heat directly from a high-temperature gas-cooled reactor.

Kasahara et al. [16] have recently reported the status of R&D at the Japan Atomic Energy Agency (JAEA) on the thermochemical water-splitting iodine–sulfur process for hydrogen production with the use of heat (temperatures close to 1000°C) from a nuclear plant, with particular attention to flowsheet studies of the process. They carried out successfully a continuous and stable operation of the bench-scale apparatus. Membrane techniques aimed for application to an HI decomposition procedure were investigated. A preliminary screening of corrosion resistant materials has been performed, and a ceramic heat exchanger for an H_2SO_4 vaporizer has been test-fabricated. A flowsheet study has been carried out for the membrane application for HI processing. An upper bound thermal efficiency was estimated to be 57%. A thermal efficiency based on more realistic parameters from experimental results was 34%. A sensitivity analysis of parameters indicated the performance of the EED cell was very important. Over 40% of thermal efficiency is related improvement of the cell. They demonstrated the importance of getting HI-rich HI_x solutions at the Bunsen reaction stage.

1.1.2 Recent Advances in the USA

Forsberg [7] from the Oak Ridge National Laboratory indicated that the infrastructure of H_2 consumption is compatible with the production of H_2 by nuclear reactors. Alternative H_2 production processes were examined to define the requirements such processes would impose on the nuclear reactor. These requirements include supplying heat at a near-constant high temperature, providing a low-pressure interface with the H_2 production processes, isolating the nuclear plant from the chemical plant, and avoiding tritium contamination of the H_2 product. A reactor concept—the advanced high-temperature reactor—was developed to match these requirements for H_2 production.

Forsberg et al. [17] utilized a molten-salt–cooled Advanced High-Temperature Reactor (AHTR) as a reactor concept designed to provide very high-temperature heat (750 to 1000^0C) to enable efficient low-cost thermochemical production of hydrogen or production of electricity. They provided an initial description and technical analysis of its key features. The proposed AHTR used coated-particle graphite-matrix fuel similar to that used in high temperature gas-cooled reactors (HTGRs), such as the General Atomics gas turbine–modular helium reactor. However, unlike the HTGRs, the AHTR used a molten salt coolant and a pool configuration, similar to that of the General Electric Super Power Reactor Inherently Safe Module (S-PRISM) liquid-metal reactor. Since the boiling points for molten fluoride salts are 1400^0C, the reactor could operate at very high temperatures and atmospheric pressure. For thermochemical H_2 production, the heat was delivered at the required near-constant high temperature and low pressure.

Yildiz et al. [18] proposed hydrogen production using high-temperature steam electrolysis (HTSE) supported by a supercritical CO_2 (SCO_2) recompression Brayton cycle that was directly coupled to an advanced gas-cooled reactor (AGR). The system features and efficiency were analyzed in a parametric fashion. The analysis included the influence of the major component's performance and the component integration in a proposed plant layout. The configuration, HTSE-SCO_2-AGR, with thermal recuperation from the product gas streams, and an intermediate heat exchanger between the turbine exit and the feed water stream, was found to offer excellent thermal efficiency, operational flexibility, and expected costs. The HTSE average process temperature was 900^0C, and the hydrogen pipeline delivery pressure was assumed to be 7 MPa for the evaluation of the plant performance. The reactor exit temperature and the SCO_2 cycle turbine inlet temperature were the same as those for the SCO_2 recompression cycle design: 550 to 700^0C. The 900^0C temperature at the HTSE unit, which was higher than the reactor exit temperature, was achieved with recuperative and electrical heating. HTSE was assumed to operate within 80 to 90% voltage efficiency at 1 atm to 7 MPa of pressure. A parametric analysis of these operating conditions showed that the system can achieve 38.6 to 48.2% low heating value for the net hydrogen production energy efficiency. Extensive experience from commercial AGRs, the compactness of the SCO_2 power conversion system, and the progress in the electrolysis cell materials can improve

the economical development of a future recuperative HTSE-SCO_2-AGR. The authors addressed materials processing for the durability and efficiency of the HTSE system, the design update of the AGR with advanced materials to resist high-pressure CO_2 coolant, thermal hydraulics of CO_2 at supercritical pressures, and detailed component design for system integration as the major research and development needs for this plant concept.

In past work by Summers and Gorensek [19], two sulfur cycles – the Sulfur-Iodine (S-I) and the Hybrid Sulfur (HyS) – emerged as leading thermochemical processes for making hydrogen using heat from advanced nuclear reactors. The Savannah River National Laboratory (SRNL) has been tasked by the U.S. Department of Energy Office of Nuclear Energy, Science & Technology with development of the HyS cycle since 2004. They discussed the background, current status, recent development results, and the future potential of the HyS process. Process design studies suggested that a net thermal efficiency of over 50% (higher heating value basis) is possible with HyS. Economic studies indicated that a nuclear hydrogen plant based on this process can be economically competitive, assuming that the sulfur dioxide-depolarized electrolyzer can be successfully developed. SRNL has demonstrated the use of a proton exchange membrane cell to perform this function, thus holding promise for economic and efficient hydrogen production.

McLaughlin et al. [20] estimated the capital and operating costs for producing hydrogen from the Pebble Bed Modular Reactor (PBMR) and the Hybrid Sulfur Process (HyS), also called the Westinghouse Sulfur Process (WSP). These calculations used a 400MWt version of the PBMR designed for the production of process heat at a temperature up to 950°C. Process heat between about 776°C and 950°C was used by the HyS to perform the decomposition of SO_3 to O_2 and SO_2 using a sulfuric acid separation system as the high temperature heat exchanger. Electricity for the HyS electrolysis step and export heat was obtained from the PBMR energy between about 550°C and 776°C, using a Rankine steam cycle as the Power Conversion Unit (PCU). The estimated capital cost for a plant producing 0.83 kg/sec of H_2 at 1300 psia was estimated at $285 million. Based on an 18% per year write-off and an availability of 95%, the cost of H_2 was estimated at $3.85/kg.

Smith et al. [21] presented an overview of the engineering methods, models, and results used in an evaluation for locating a hydrogen production facility near a proposed next-generation nuclear power plant. The quantitative analysis performed and described by Smith and co-workers [21] offers a mechanism to determine key parameters relating to the development of a nuclear-based hydrogen production facility. Their calculations indicated that when the facilities are less than 100 m apart, the core damage frequency is large enough to become problematic in a risk-informed environment. They reported that a variety of design modifications (blast-deflection barriers, for example) could significantly reduce risk and should be further explored as the design of a hydrogen production facility evolves.

The Argonne National Laboratory [22] is developing low temperature thermochemical cycles designed to split water and produce hydrogen at 550°C or less. The hybrid copper-chloride (Cu-Cl) cycle is one of the most promising cycles for this temperature region. This cycle consists of three thermal reactions and one electrochemical reaction. Lewis et al. [22] presented the results of the first Aspen simulation, based on experimental results and process design goals. A preliminary estimate of the open cycle efficiency of the Cu-Cl cycle has been calculated from the simulation. They reported that the closed cycle efficiency may be increased significantly when the Cu-Cl cycle is linked with the HTGR.

1.1.3 Recent Advances in Korea

Park and Lee [23] from the Korea Atomic Energy Research Institute addressed requirements of Nuclear Hydrogen Design Development (NHDD), with a large number of calculations involving operating parameter variations and many different system configurations. For this task, the *Hydrogen Production Plant Efficiency Calculator*, which was specifically designed to be an easy-to-use and fast running tool for the hydrogen and electricity production evaluation with a flexible system layout, has been developed. It includes the cost models to enable the program to carry out the system optimization calculations.

1.1.4 Past Developments in Canada

Rosen [2] and Rosen and Scott [24] reported comparisons based on energy and exergy analyses of a wide range of hydrogen production processes, including processes which are hydrocarbon-based (steam-methane reforming and coal gasification), non-hydrocarbon-based (water electrolysis and thermochemical water decomposition) and integrated (steam-methane reforming linked to the non-hydrocarbon-based processes). A version of the Aspen Plus process simulation computer code for exergy analysis, was used in the analyses. Overall efficiencies were determined to range widely, from 21 to 86% for energy efficiencies, and from 19 to 83% for exergy efficiencies. The losses in all processes were found to exhibit many common factors. Energy losses associated with emissions accounted for 100% of the total energy losses, while exergy losses associated with emissions accounted for 4-10% of the total exergy losses. The remaining exergy losses were associated with internal irreversibilities.

Granovskii et al. [25] have extended life cycle assessment to exergetic life cycle assessment and used it to evaluate the exergy efficiency, economic effectiveness and environmental impact of producing hydrogen using wind and solar energy in place of fossil fuels. The product hydrogen is a fuel for fuel cell vehicles and a potential substitute for gasoline. Exergy efficiencies, greenhouse gases and air pollution emissions were evaluated for all process steps, including crude oil and natural gas pipeline transportation, crude oil distillation and natural gas reforming, wind and solar electricity generation, hydrogen production through water electrolysis, and gasoline and hydrogen distribution and utilization. As addressed by the authors, the use of wind power to produce hydrogen via electrolysis, and its application in a fuel cell vehicle, exhibits the lowest fossil and mineral resource consumption rate. However, the economic attractiveness, as measured by a "capital investment effectiveness factor", of renewable technologies depends significantly on the ratio of costs for hydrogen and natural gas. At the cost ratio of about 2 (per unit of lower heating value or exergy), capital investments were found to be about five times lower to produce hydrogen via natural gas, rather than wind energy. As a consequence, the cost of wind- and solar-based electricity and hydrogen was reported to be substantially higher than that of natural gas.

Atomic Energy of Canada Ltd. (AECL) [26] has identified the copper-chlorine (Cu-Cl) cycle as a promising cycle for thermochemical hydrogen production. Water is decomposed into hydrogen and oxygen through intermediate Cu-Cl compounds. The Cu-Cl thermochemical cycle uses a series of reactions to achieve the overall splitting of water into hydrogen and oxygen. This cycle is expected to operate at 500°C to produce hydrogen and oxygen at a temperature compatible with current power plant technologies, such as the sodium-cooled fast reactor. It has the advantages that corrosion issues are more tractable at 500°C than at higher temperatures, compared to the S-I cycle. The energy efficiency of the process is projected to be 40–45% [4]. Recently, it has been reported at 44.4% by Lewis [27] from the US Argonne National Laboratory (ANL).

The Cu-Cl cycle is a match for Canada's Super-Critical Water Reactor (SCWR), Canada's Generation IV nuclear reactor. Other advantages of this proposed process are reduced demands on materials of construction, inexpensive chemical agents, insignificant solids handling and reactions going to completion without side reactions [3]. The primary components of the cycle are four interconnected reaction vessels, with intermediate heat exchangers, and a drying step. The sequence of steps in the Cu-Cl cycle is shown in Table 1.1. A preliminary conceptual schematic of the Cu-Cl cycle is depicted in Fig. 1.1. Further description of the cycle may be found in the work of Rosen et al. [3], as well as past studies at the Argon National Laboratory (ANL), as reported by Lewis et al. [22] and Serban et al. [28].

1.2 OBJECTIVES AND MOTIVATION OF THESIS

Currently a research team led by the University of Ontario Institute of Technology (UOIT) is developing a lab-scale demonstration of sustainable hydrogen production by thermochemical water splitting with a copper-chlorine cycle, in collaboration with Atomic Energy of Canada Ltd. (AECL), ANL and other partners. The overall project has been divided into 5 sub-project groups:

I. Research on thermal efficiency of the cycle and its modifications;
II. Research on thermochemistry/electrochemistry;
III. Research on thermal/fluids equipment;
IV. Research on mechanical/materials design;

V. Research on controls, safety and reliability.

Sub-group 1 consists of 4 sections:

- System Simulation and Modeling Studies;
- Energy/ Exergy / Exergoceonomic Analysis of System and Components;
- Life Cycle Assessment;
- Studies of Combined or Hybrid Systems on Nuclear and Wind/Solar Power.

Modeling studies on transport phenomena aspects of the system and its components are required to be carried out within section 1 of the first sub-group. The purpose of this thesis work is to investigate transport phenomena of the reaction of cupric chloride particles with superheated steam (reaction 4 in Table 1.1), which takes place in a fluidized bed reactor by performing a parametric study. Preliminary steps in studying the transport phenomena of a fluidized bed reactor consist of a hydrodynamics analysis, e.g. see Ref. [29]. A mass balance of both gas and solid reactants requires essentially the bed properties, such as bed height, bed voidage and bubble diameter, which are obtained through a hydrodynamics analysis. Since little or no experimental data of hydrodynamics and chemistry of the above reaction are available, the hydrodynamics of the bed will be analyzed by utilizing correlations that may be found in the literature. Thus, as a first step, the effective bed properties will be introduced by analysing the hydrodynamic behaviour of the bed.

Table 1.1: Steps in the Cu-Cl thermochemical cycle for hydrogen production

Step	Reaction	Temperature Range, ^{0}C
1	$2Cu(s) + 2HCl(g) \rightarrow 2CuCl(l) + H_2(g)$	430-475
2	$2CuCl(s) \rightarrow 2CuCl(aq) \rightarrow CuCl_2(aq) + Cu(s)$	30-70 (electrolysis)
3	$CuCl_2(aq) \rightarrow CuCl_2(s)$	> 100
4	$2CuCl_2(s) + H_2O(g) \rightarrow CuO*CuCl_2(s) + 2HCl(g)$	400
5	$CuO*CuCl_2(s) \rightarrow 2CuCl(l) + 1/2O_2(g)$	500

Source: Ref [3]

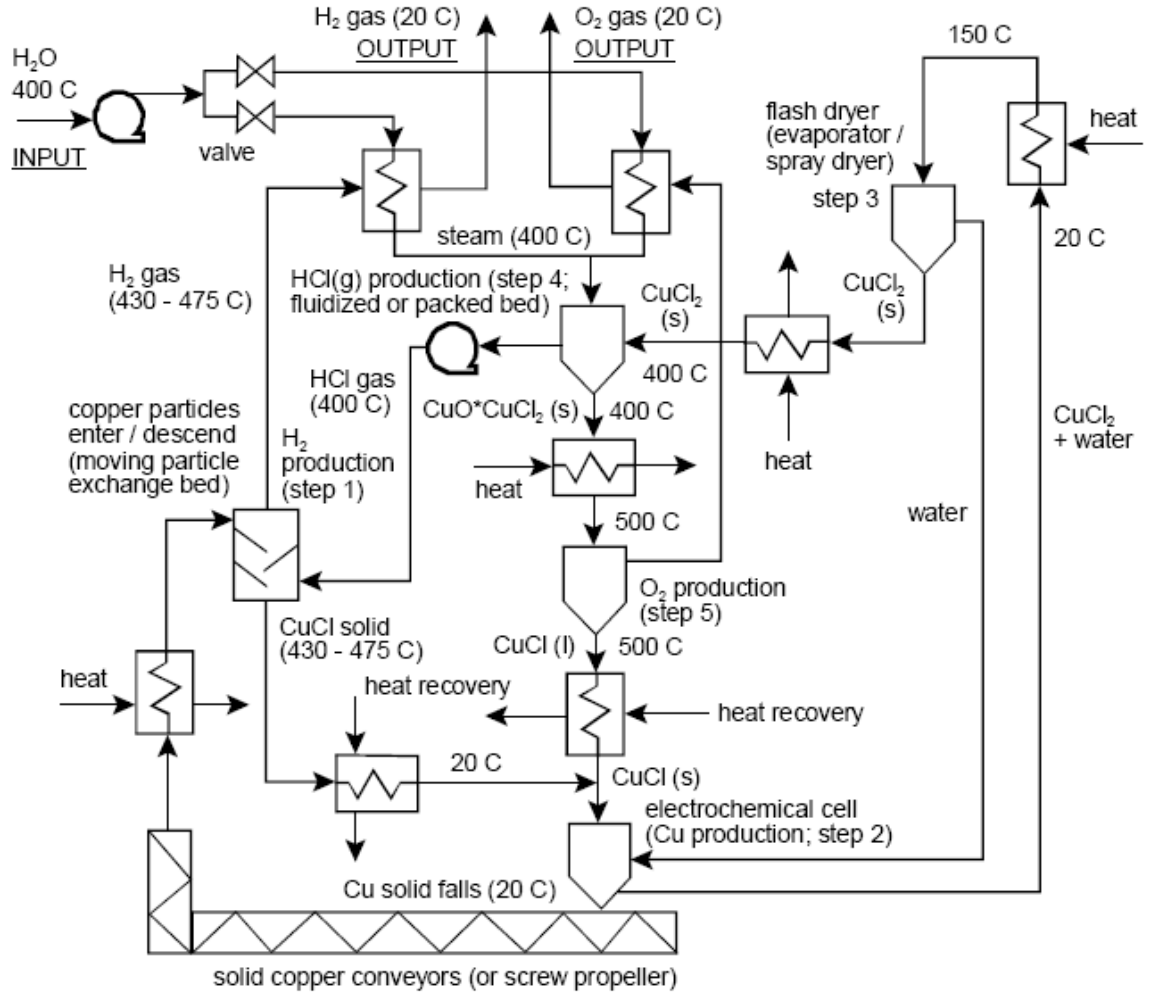

Fig. 1.1: Schematic of copper-chlorine cycle for hydrogen production, Ref. [3].

Since both cupric chloride and steam participate in the chemical reaction, as the next step, it is necessary to apply a Non-Catalytic Gas-Solid Reaction (NCGSR) model which describes conversions of cupric chloride particles, as well as steam. A literature survey indicates little work has been done in this field, although there are several works that have focused on modelling the conversion of gaseous species, such as those represented for Catalytic Gas-Solid Reactions (CGSRs). Examples are methods used in gasification in a fluidized bed [30]. Moreover, whether the particle reaction follows a *uniform reaction model (Volumetric Model-VM)* or a *Shrinking Core Model (SCM)* is usually defined according to lab-scale measurements. Due to absence of such measured data, the above two models will be considered as limiting cases in the current thesis.

Physical models of *Kunii and Levenspiel* [31] are well-known, wherein three reactor models depending upon flow regimes can predict the conversion of reacting gas. Furthermore, they developed two limiting models to describe the conversion of solid particles in a NCGSR. These two models are based on two extremes of behaviour, i. e. VM and SCM. However, the calculation procedure of *Kunii and Levenspiel* [31] is tedious, since one should consider a combination of various different models depending on process conditions. It would be beneficial to employ one single model that best describes the conversion of both gaseous and solid reactants. This goal is addressed in this thesis. Hence, based on two limiting models, i. e. VM and SCM, a separate numerical solution procedure is developed for each model, to monitor the effects of various parameters on conversions of $CuCl_2$ particles and steam.

1.3 OVERALL PLAN OF RESEARCH

Chapter 2 is devoted to a hydrodynamics analysis of fluidization. Key bed properties such as the bed height (for a vertical reactor), bubble diameter, bed voidage, etc., are introduced in Chapter 2. Studying the hydrodynamics behavior of a fluidized bed is a necessary step for mass transport analysis of the process.

Various reactor models, as well as kinetic models describing conversion of solid particles which participate in the reactions, are reviewed in Chapter 3. A recent non-catalytic gas-solid reaction (NCGSR) model is also introduced in this chapter, for usage in the present study.

The detailed analysis is presented in Chapter 4, from both hydrodynamics and species balance standpoints. The numerical solutions to study the fluid-dynamics and conversion of reactants are individually developed.

Chapter 5 illustrates the results of transport phenomena of reactions of cupric chloride particles with superheated steam, using the analysis in Chapter 4. In the hydrodynamics part, the effect of various parameters, such as superficial gas velocity, bed inventory of solid particles and particle diameter on the bed properties, e. g., bed height, average bubble diameter, are investigated and the results are discussed. Furthermore, applying the mass transport analysis to the conversions of reactants, as well as the bed

performance in terms of a newly introduced parameter called “Bed Effectiveness”, are studied at various process conditions.

Concluding remarks are summarized in Chapter 6. The findings of this thesis may be utilized in designing the experimental apparatus and evaluating the optimal parameters of the reactor, when building the lab-scale hydrogen production plant.

Chapter 2

Hydrodynamic Aspects of Fluidization

2.1 INTRODUCTION

Fluidization occurs when a gas or liquid is forced to flow vertically through a bed of particles, at such a rate that the buoyant weight of particles is completely supported by the drag force imposed by the fluid [29]. A fluidized bed displays the following characteristics similar to those of a liquid [30].

1) The static pressure at any height is approximately equal to the weight of the bed of solids, per unit of cross-sectional area above that level.
2) An object denser than the bulk density of the bed will sink, while one lighter will float. Thus, a steel ball sinks in the bed, while a light badminton cork floats on the surface.
3) The solids from the bed may be drained like a liquid through an orifice at the bottom or side of the container. The solid flow-stream is similar to a water jet from a vessel.

4) The bed surface maintains a horizontal level, independent of how the bed is tilted. Also, the bed assumes the shape of the vessel.
5) Particles are well mixed, and the bed maintains a nearly uniform temperature throughout its body when heated.

To understand how a fluidized bed is formed, imagine a gas moving up through a bed of granular solids resting on the porous bottom of a column. As the gas velocity through the solid particles increases, a series of changes in the motion of the particles could occur. For example, at a low flow rate, the fluid percolates through the void of spaces between stationary particles. This is called a *fixed or packed bed*. With changes in gas velocity, the solid particles move from one state/regime to another.

At a higher velocity, a point is reached where all particles are suspended by the upward flowing gas or liquid. At this point the frictional force between particles and the fluid counterbalances the weight of the particles. The vertical component of the compressive force between adjacent particles disappears and the pressure drop through any section of the bed nearly equals the weight of fluid and particles in that section. The bed is considered to be fluidized and it is called an incipiently fluidized bed, or a bed at the minimum fluidization [31].

Most applications of fluidized beds are cases where the fluidizing fluid is a gas, rather than a liquid. Gas-fluidized beds show a number of distinct flow regimes. The principal ones appear schematically in Fig. 2.1 for increasing superficial gas velocities (from left to right), in a column of high height-diameter ratio.

2.2 THE GELDART CLASSIFICATION OF PARTICLES

By carefully observing the fluidization of all types and sizes of solids, Geldart developed four clearly recognizable kinds of particle behavior. For smaller to larger particles, they are grouped as follows [31]:

- *Group C*: cohesive, or very fine powders. Normal fluidization is extremely difficult for these solids, because inter-particle forces are greater than those resulting from the action of the gas.

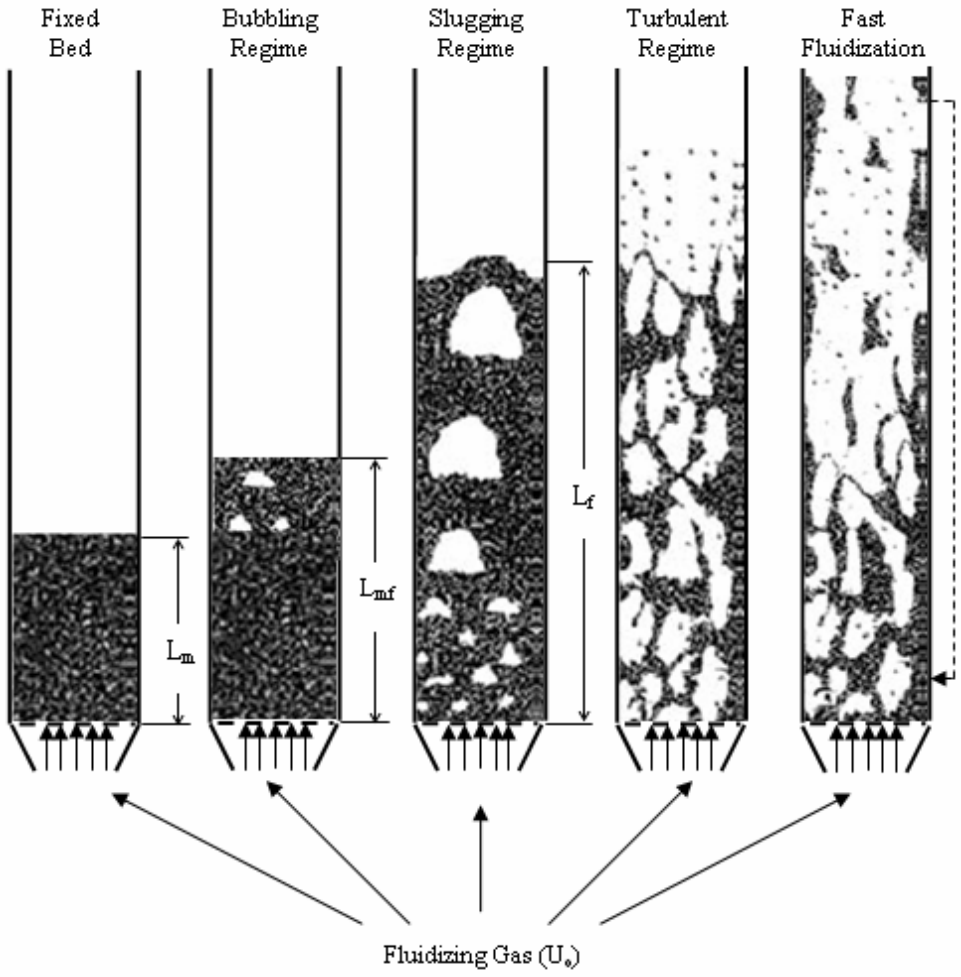

Fig. 2.1: Various fluidization regimes depending on the gas velocity (modified from Ref. [29]).

Group A: aeratable, with materials having a small mean particle size and/or low particle density (< ~ 1.4g/cm^3). These solids fluidize easily with small bubbles at higher gas velocities. An FCC catalyst is representative of these solids.

- *Group B:* sand-like, with most particles of size 40μm < d_p < 500μm and a density of 1.4<ρ_p<4 g/cm^3. These solids fluidize well with vigorous bubbling action and bubbles that grow large.

Group D: spoutable, with large and/or dense particles. Deep beds of these solids are difficult to fluidize. They behave erratically, giving large exploding bubbles or severe channeling, or spouting behavior if the gas distribution is uneven. Drying grains, peas or roasting coffee beans are such solids and they are usually processed in shallow beds.

Boundaries between adjacent groups for fluidization by air at room temperature and atmospheric pressure are shown in Fig. 2.2. This classification was extended by Grace [29, 32] to cover gases other than air, as well as operating temperatures and pressures other than atmospheric.

CA Boundary. This boundary will divide the system where inter-particle forces are so strong, that normal fluidization is impossible, from those where unaided fluidization is possible despite significant inter-particle forces. It is the most difficult boundary to predict, since it depends on a number of non-hydrodynamic factors, such as electrostatic charges and relative humidity, which can affect inter-particle forces, primarily caused by van der Waals forces.

AB Boundary. The AB boundary distinguishes systems where inter-particle forces are significant (but not dominant, group A) from those (group B) where inter-particle forces do not have a significant role. Data for this boundary for various gases, including air, at different temperatures and pressures have been correlated in Ref. [32] as follows,

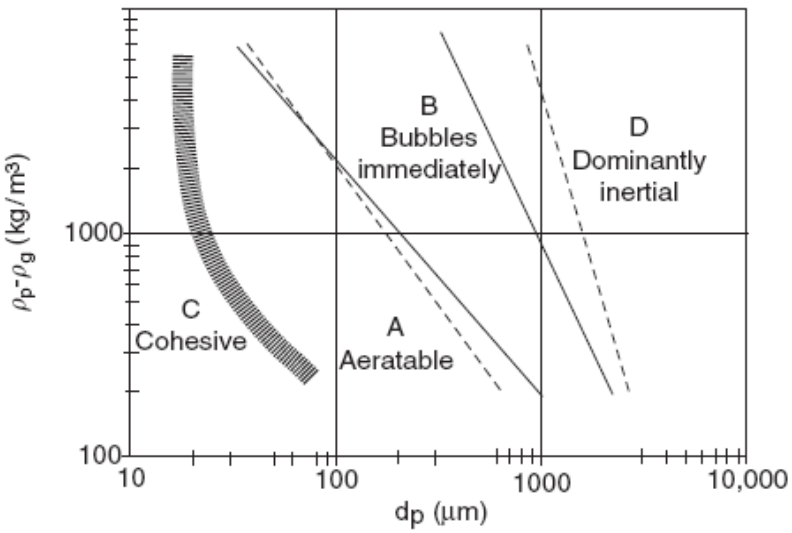

Fig. 2.2: Geldart powder groups for fluidization by air at room temperature and atmospheric pressure. The CA boundary is typical, but varies with properties such as moisture content of the particles. The solid lines give AB and BD boundaries, as suggested originally by Geldart. The dashed lines are AB and BD boundaries from Eqs. (2-1) and (2-2), respectively [29].

$$Ar_{AB} = \left| \frac{g\rho_g \left(\rho_p - \rho_g\right) d_p^3}{\mu_g^2} \right|_{AB\,boundary} = 1.0 \times 10^6 \left[\left(\rho_p - \rho_g\right) / \rho_g \right]^{-1.275} \quad (2\text{-}1)$$

where *Ar* represents the *Archimedes Number*

$$Ar = \frac{g\rho_g \left(\rho_p - \rho_g\right) d_p^3}{\mu_g^2} \quad (2\text{-}2)$$

an individual variables are defined in the nomenclature.

BD Boundary. This boundary separates systems where flow through the particles is dominated by viscous forces, from those where inertial effects are dominant. The boundary between groups B and D depends on whether the flow through the particulate phase is laminar or turbulent, leading to

$$Ar_{BD} = \left| \frac{g\rho_g \left(\rho_p - \rho_g\right) d_p^3}{\mu_g^2} \right|_{BD\,boundary} = 1.45 \times 10^5 \quad (2\text{-}3)$$

2.3 FLUIDIZATION REGIMES

Before we can predict the behavior of a specific gas-solid operation, we must know what contacting regime will be encountered. We can then use the appropriate expressions for that regime. We can also determine whether solid recirculation, cyclones, and so forth, are needed. This issue is especially important for the design engineer concerned with industrial applications [31]. As the gas velocity through the solid particles increases, a series of changes in the motion of particles could occur. With changes in gas velocity, the solids move from one regime to another. These regimes, arranged in order of increasing velocities, are [30]:

- Packed bed (fixed);
- Bubbling bed;
- Turbulent bed;

- Fast bed (used in circulating fluidized beds);
- Transport bed (pneumatic or entrained bed).

Table 2.1 compares the features of the above gas–solids contacting processes [30]. Also, the various regimes of gas-solid fluidization are summarized in Table 2.2, where the boundaries of different regimes are defined based on the range of superficial gas velocity. A flow regime diagram is shown in Fig. 2.3 for cases where the column is large enough that the slug flow regime is never reached. This form of regime diagram is convenient because the abscissa is a dimensionless particle diameter, whereas the ordinate is a dimensionless superficial gas velocity. Approximate boundaries between the powder groups introduced in the previous section are also shown in the figure [29]. The axes of Fig. 2.3 are labeled with the dimensionless variables d_p^* and U^*, defined in Eqs. (2-4) and (2-5), respectively,

$$d_p^* = d_p\left[\frac{g\rho_g\left(\rho_p-\rho_g\right)}{\mu_g^2}\right]^{1/3} = Ar^{1/3} \tag{2-4}$$

$$U^* = U_o\left[\frac{\rho_g^2}{g\mu_g\left(\rho_p-\rho_g\right)}\right]^{1/3} = \frac{Re_p}{Ar^{1/3}} \tag{2-5}$$

where and Re_p denotes the particle *Reynolds number*, defined as

$$Re_p = \frac{\rho_g d_p U_o}{\mu_g} \tag{2-6}$$

2.4 CONDITIONS OF MINIMUM FLUIDIZATION

Consider a bed of solid particles in a cylindrical vessel, whose bottom is permeable, with gas forced upward through it. As noted previously, fluidization requires that the pressure drop across the beds matches the buoyant weight of the particles. The force balance requires that the drag force by the upward moving gas equals the weight of particles. Hence,

$$\frac{dP}{dz} = -\left(\rho_p - \rho_g\right)\left(1-\varepsilon_{mf}\right)g \tag{2-7a}$$

or

$$\Delta P_b = L_{mf}\left(1-\varepsilon_{mf}\right)\left(\rho_p - \rho_g\right)g \tag{2-7b}$$

The pressure drop per unit height of a packed (fixed) bed of height L_m, of uniformly sized particles, d_p, is correlated by Ergun [34]:

$$\frac{\Delta P_b}{L_m} = 150\frac{\left(1-\varepsilon_m\right)^2}{\varepsilon_m^3}\frac{\mu_g U_o}{\left(\varphi d_p\right)^2} + 1.75\frac{1-\varepsilon_m}{\varepsilon_m^3}\frac{\rho_g U_o^2}{\varphi d_p} \tag{2-8}$$

Table 2.1: Comparison of gas-solid contacting processes

Property	Packed bed	Fluidized bed	Fast Bed	Pneumatic Transport
Mean particle diameter	<0.3mm	0.03-3mm	0.05-0.5mm	0.02-0.08mm
Gas velocity (m/s)	1-3	0.5-2.5	4.0-6.0	15-30
Gas motion	Up	Up	Up	Up
Gas mixing	Near plug flow	Complex two phases	Dispersed plug flow	Near plug flow
Solids motion	Static	Up and down	Mostly up, some down	Up
Solid-solid mixing	Negligible	Usually near perfect	Near perfect	Small
Overall voidage	0.4-0.5	0.5-0.85	0.85-0.99	0.99-0.998
Temperature gradient	Large	Very small	Small	Maybe significant

Source: *Ref. [30]*

Table 2.2: Description of various fluidization regimes

Velocity range	Fluidization regime	Fluidization features and appearance
$0 \leq U_o < U_{mf}$	Fixed bed	Particles are quiescent; gas flows through interstices
$U_{mb} \leq U_o < U_{ms}$	Bubbling regime	Gas bubbles form above distributor, coalesce and grow; gas bubbles promote solids mixing during rise to surface and breakthrough
$U_{ms} \leq U_o < U_c$	Slug flow regime	Bubble size approaches bed cross section; bed surface rises and falls with regular frequency with corresponding pressure fluctuation
$U_k \leq U_o < U_{tr}$	Turbulent regime	Small gas voids and particle clusters and streamers dart to and fro; bed surface is diffused and difficult to distinguish
$U_o > U_{tr}$	Fast fluidization	Particles are transported out of the bed and need to be replaced and recycled; normally has a dense phase region at bottom coexisting with a dilute phase region on top; no bed surface

Source: Ref. [33]

where U_o is the superficial gas velocity (total gas volumetric flow rate divided by the total column cross-sectional area) and φ is a particle shape factor called the sphericity, defined as the surface area of a volume equivalent sphere, divided by the true external surface area of the particle. Transition from a fixed bed to a fluidized bed occurs when the pressure drop across a loosely packed fixed bed reaches the value given by Eq. (2-7b). Hence, one can estimate the superficial velocity, U_{mf} , at the transition between a fixed and fluidized bed, called the "minimum fluidization velocity," by solving the quadratic equation obtained when the right sides of (2-7b) and (2-8) are equated. The result leads to [29]:

$$Re_{mf} = \frac{\rho_g d_p U_{mf}}{\mu_g} = \sqrt{C_1^{\,2} + C_2 Ar} - C_1 \tag{2-9}$$

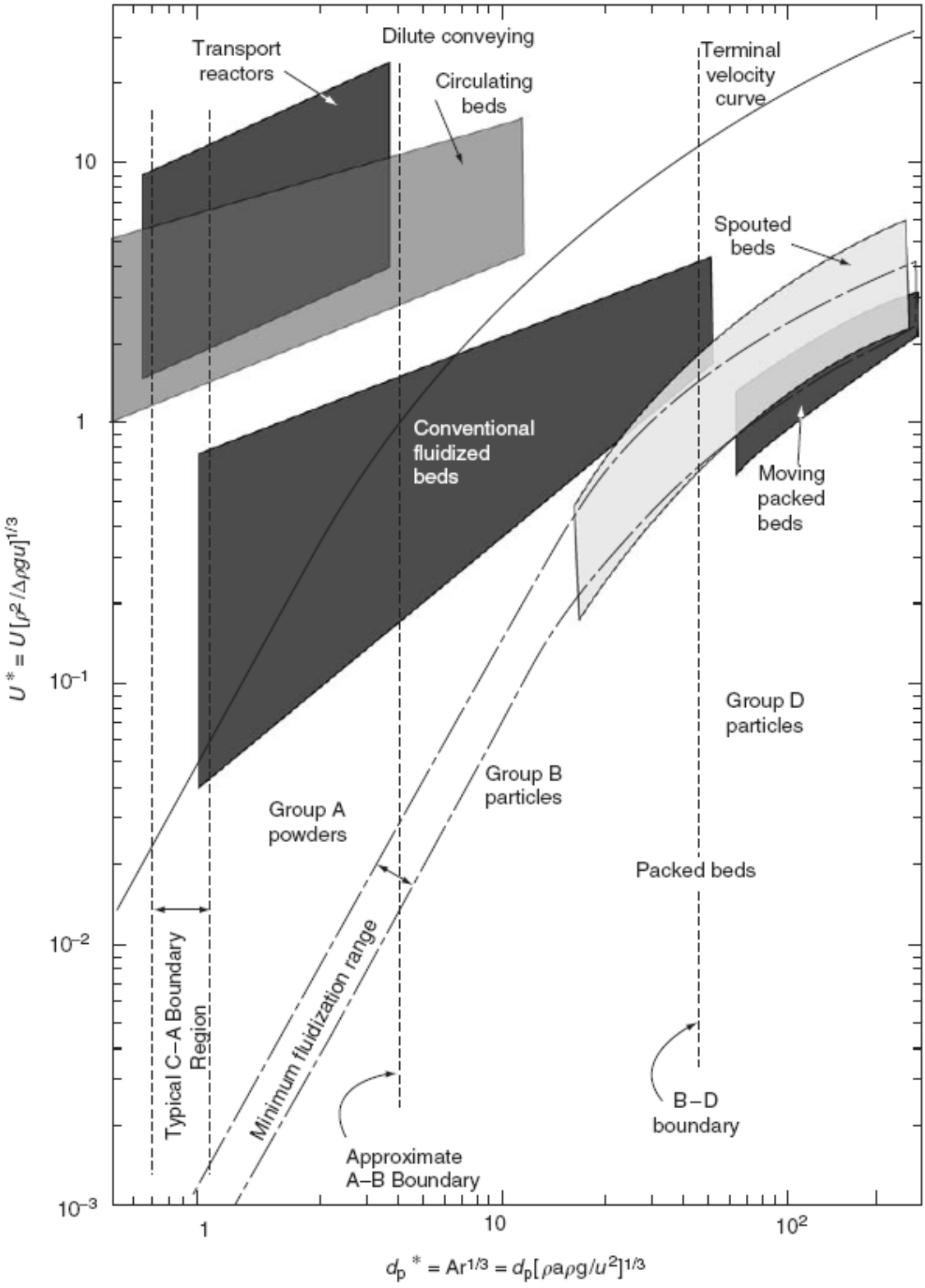

Fig. 2.3: Dimensionless flow regime map for upward gas flow through solid particles. Letters *C, A, B* and *D* refer to the Geldart classification of solids [29].

Different values of the constants, C_1 and C_2, are available in the literature, with the most common being C_1=33.7 and C_2=0.0408, as recommended by Wen and Yu [35]. Typically this equation predicts the minimum fluidization velocity within approximately $\pm 25\%$, so it is best to measure it experimentally whenever possible. The most common method of measurement requires that the pressure drop across the bed is recorded as the superficial velocity is increased stepwise through U_{mf} and beyond; U_{mf} is then taken at the intersection of the straight lines corresponding to the fixed bed and fluidized-bed portions of the graph obtained when ΔP_b is plotted against U on log–log coordinates. At the same time as U_{mf} is measured, it is important to also determine the bed voidage at the minimum fluidization, ε_{mf}, requiring that one finds the mass (bed inventory), W_b, of the particles, the bed height, L_{mf}, at the minimum fluidization, and the particle density, ρ_p, according to

$$\varepsilon_{mf} = 1 - \frac{W_b}{\rho_p A_{c,bed} L_{mf}} \tag{2-10}$$

Equation (2-9) can be simplified when the particles are either small (low Ar) or large (high Ar). With the C_1 and C_2 values specified above [29], then

$$Re_{mf} = \begin{cases} 6.1\times10^{-4} Ar & Ar < 10^3 \\ 0.202 Ar^{0.5} & Ar > 10^7 \end{cases} \tag{2-11}$$

or

$$U_{mf} = \begin{cases} 0.00061 \dfrac{g(\rho_p - \rho_g) d_p^{\,2}}{\mu_g} & Ar < 10^3 \\ 0.20 \sqrt{\dfrac{g(\rho_p - \rho_g) d_p}{\rho_g}} & Ar > 10^7 \end{cases} \tag{2-12}$$

where d_p denotes the mean diameter of particles.

2.5 BUBBLE PROPERTIES

2.5.1 Bubble Size and Bubble Growth

Experiments show that the bubble size in fluidized beds increases with gas velocity and height above the distributor, and varies widely from system to system. Bubbles in a bubbling bed can be irregular in shape and may vary greatly in size. This makes it difficult to characterize a mean bubble size, although such a measure is needed. For application purposes, we define the mean spherical bubble of diameter d_b that represents the bubbles in the bed, usually a mean volumetric size. However, for certain extremely fast kinetic processes, one should more strongly weight the smaller bubbles since most of the transfer or reaction occurs near the bottom of the bed, where the bubbles are small [31].

Several correlations to estimate bubble growth in fluidized beds have been developed from experiments, mainly in small diameter beds of Geldart *B* solids [31]. Mori and Wen [36] proposed the following correlation for Group *B* and *D* particles, which gives the bubble diameter at any height z in a bed of diameter D_t:

$$\frac{d_{bm} - d_b}{d_{bm} - d_{b0}} = exp\left(-0.3 \frac{z}{D_t} \right) \tag{2-13}$$

where d_{bm} is the bubble limiting (maximum) size evaluated as [37]

$$d_{bm} = Min\left\{ 163.77\left[0.7854.\left(U_o - U_{mf} \right) D_t^2 \right]^{0.4},\ D_t \right\} \tag{2-14}$$

Also, d_{b0} is the initial bubble size formed near the bottom of the bed given by [37]

$$d_{b0} = \begin{cases} \dfrac{0.082}{g^{0.2}} \left[\dfrac{U_o - U_{mf}}{N_{or}} \right]^{0.4} & for\ \ d_{b0} \le l_{or} \\ \dfrac{0.0278}{g} \left(U_o - U_{mf} \right)^2 & for\ \ d_{b0} > l_{or} \end{cases} \tag{2-15}$$

Here N_{or} represents the hole density of the distributor, and l_{or} denotes the spacing between adjacent holes on the distributor.

$$N_{or} = \begin{cases} \dfrac{1}{l_{or}^2} & \textit{for square array of holes} \\ \dfrac{2}{\sqrt{3} l_{or}^2} & \textit{for triangle array of holes} \end{cases} \tag{2-16}$$

2.5.2 Bubble Rise Velocity

The single bubble rise velocity can be determined using the proposed correlation of Davidson and Harrison [31], as follows.

$$U_{br} = 0.711 (g.d_b)^{0.5} \tag{2-17}$$

This is not an absolute velocity, as used with respect to the emulsion phase. The bubble velocity, however, may be evaluated as

$$U_b = U_o - U_{mf} + U_{br} \tag{2-18}$$

Based on experimental data, Kunii and Levenspiel [31] suggested the following correlations for the bubble velocity for a column with $D_t \leq 1m$.

$$U_b = 1.55\{(U_o - U_{mf}) + 14.1(d_b + 0.005)\} D_t^{0.32} + U_{br} \quad \text{for Geldart } A \text{ particles} \tag{2-19}$$

$$U_b = 1.6\{(U_o - U_{mf}) + 1.13 d_b^{0.5}\} D_t^{1.35} + U_{br} \quad \text{for Geldart } B \text{ particles} \tag{2-20}$$

2.6 BED PROPERTIES

When the superficial gas velocity is equal to $U_{mf,}$ a bed exists at the minimum fluidized condition. In this state, there is no bubble, and only the emulsion phase remains. For Group *B* and *D* particles, further excess in the gas that exceeds above the limit would

lead to the formation of bubbles, which push their way into the emulsion phase of solids, resulting in bed expansion. A mass balance for the bed solids gives [31]

$$L_{mf}\left(1-\varepsilon_{mf}\right)=L_{f}\left(1-\varepsilon_{b}\right) \tag{2-21}$$

The bed voidage at the minimum fluidization, ε_{mf}, is usually defined based on experimental measurements. However, if there is a lack of data, it may be estimated based on the particle sphericity, φ as follows,

$$\varepsilon_{mf}=\left(\frac{1}{14\varphi}\right)^{1/3} \tag{2-22}$$

Moreover, the bed void fraction represented by ε_b, is determined by [38]

$$\varepsilon_{b}=1-\frac{1-\varepsilon_{mf}}{1+\dfrac{U_{o}-U_{mf}}{U_{br}}} \tag{2-23}$$

In the next chapter, modeling of transport phenomena within a fluidized bed will be presented.

Chapter 3

Modelling of Two-Phase Transport Processes

3.1 INTRODUCTION

Historically, two classes of models have been proposed to describe the performance of fluidized bed reactors; one is based on a pseudo-homogeneous approach and the other is a two-phase approach. In the pseudo-homogeneous approach, the existence of more than one phase is not taken into account. It proposes the use of conventional multiphase flow models for the fluidized bed reactors. These conventional models may include ideal flow models, dispersion models, residence time distribution models, and contact time distribution models. The two-phase approach, however, considers the fluidized bed reactor to consist of at least two phases, a bubble and an emulsion, and proposes a separate governing equation for each phase, with a term in each equation describing mass interchange between the two phases. Among the two-phase models, the bubbling bed model proposed by *Kunii and Levenspiel* [31] and the bubble assemblage model proposed by *Kato and Wen* have received the most attention [33].

3.2 TWO-PHASE MODELS

Toomey and Johnstone [39] were the first researchers who introduced a two-phase theory of fluidization, which assumes that all the gas in excess of the minimum fluidization velocity flows through the bed as bubbles, while the emulsion stays stagnant at minimum fluidization conditions. The term two-phase model, however, represents a broad range of models with various basic assumptions that may or may not directly follow the original two-phase theory. For example, some models consider wakes and clouds, while others do not; some models propose the use of single-size bubbles, while others allow for bubble growth. Some models use the two-phase flow distribution following a two-phase theory, while others neglect the percolation of gas through the emulsion. In addition, different models may propose different inter-phase mass transfer mechanisms [33]. In the following sections, past literature models that predict the conversion of the gaseous reactant, along with assumptions of each model will be described.

3.2.1 Model of Davidson and Harrison

One of the representative two-phase models was proposed by Davidson and Harrison [40]. This model follows the two-phase theory of Toomey and Johnstone [39] and uses the following assumptions.

1) All gas flow in excess of that required for incipient fluidization passes through the bed as bubbles.
2) Bubbles have a uniform size throughout the bed.
3) The reaction takes place only in the emulsion phase with first-order kinetics.
4) Inter-phase mass transfer occurs by a combined process of molecular diffusion and gas flow.
5) The emulsion phase (dense phase) is either perfectly mixed (DPPM) or a plug flow (DPPF).

Note that the key parameter in their model is the equivalent bubble diameter, which was assumed to be constant.

3.2.2 Model of Partridge and Rowe

Another representative two-phase model was proposed by Partridge and Rowe [41]. In this model, the two-phase theory of Toomey and Johnstone [39] is still used to estimate the visible gas flow, as with the model of Davidson and Harrison [40]. However, this model considers the gas interchange to occur at the cloud-emulsion interface, i.e., the bubble and cloud phase are considered to be well-mixed, with the result being called a bubble-cloud phase. The model thus interprets the flow distribution in terms of the bubble-cloud phase and the emulsion phase. With the inclusion of the clouds, the model also allows reactions to occur in the bubble-cloud phase [33].

3.2.3 Model of Kunii and Levenspiel

The bubbling bed model proposed by Kunii and Levenspiel [31] is a modified version of the two-phase model. In addition to the bubble and emulsion phases, a cloud-wake phase is also considered. The model represents a group of models often called back-mixing or dense phase flow reversal models.

A key difference between this model and the other two-phase models is the inter-phase mass transfer considers two distinct resistances, one from the bubble phase to the cloud-wake phase, and the other from the cloud-wake phase to the emulsion phase. The derivation of the model involves the following background theory and observations reported by Davidson and Harrison [40], and Rowe and Partridge [41].

1) Bubble gas stays with the bubble, re-circulating very much like smoke rising and only penetrating a small distance into the emulsion. This zone of penetration is called the cloud, since it envelopes the rising bubble.
2) All related quantities, such as the velocity of the rise, cloud thickness, and the recirculation rate, are simple functions of the size of a rising bubble.
3) Each bubble of gas drags a substantial wake of solids up the bed.

Based on the above observations, the bubbling bed model makes the following assumptions.

1) Bubbles have one size and they are evenly distributed in the bed.
2) The flow of gas in the vicinity of rising bubbles follows the Davidson model.

3) Each bubble drags along with it a wake of solids, creating a circulation of solids in the bed, with up-flow behind bubbles and down-flow in the rest of the emulsion.
4) The emulsion stays at minimum fluidizing conditions; thus the relative velocity of gas and solid remains unchanged.

3.2.4 Model of Kato and Wen

Kato and Wen [33] proposed a bubble assemblage model that considers changing bubble size with height in the bed. The model uses the following assumptions.

1) A fluidized bed may be represented by n compartments in a series. The height of each compartment is equal to the size of each bubble at the corresponding bed height.
2) Each compartment is considered to consist of a bubble phase and an emulsion phase. The gas flows through the bubble phase, and the emulsion phase is completely mixed within the phase.
3) The void space within the emulsion phase is considered to be equal to the space of the bed at the incipient fluidizing conditions. The upward velocity of the gas in the emulsion phase is U_e.
4) The bubble phase is assumed to consist of spherical bubbles surrounded by spherical clouds. The voidage within the cloud is assumed to be the same as that in the emulsion phase
5) Gas interchange takes place between the two phases.
6) The bubbles grow continuously while passing through the bed, until they reach the maximum stable size, or reach the diameter of the bed column.
7) The bed is assumed to be operating under isothermal conditions, since the effective thermal diffusivity and the heat transfer coefficient are large.

3.2.5 Comparison of the Literature Models

Chavarie and Grace [42] performed an experimental study to monitor the catalytic decomposition of ozone in a two-dimensional fluidized bed reactor. Experimental concentration profiles were measured for both the dense phase and the bubble phase. They also measured the overall conversions. The experimental data were compared to

predictions from various physical models, which take account of the two-phase nature of gas fluidized beds, including the models reviewed previously. As reported by the authors, the bubbling bed model of Kunii and Levenspiel [31] provides the best overall representation of the experimental data obtained in the study. Predicted bubble phase profiles tend to traverse the measured profiles, while dense phase profiles show reasonable agreement over most of the bed depth. Overall conversions are well predicted. The success of the model can be mainly attributed to the moderate global inter-phase mass transfer, negligible percolation in the dense phase, reactions within the clouds and wakes assumed by the model, and the use of average bubble properties to simulate the entire bed.

The model of Davidson and Harrison [40], which assumes perfect mixing in the dense phase (DPPM), underestimates seriously the overall conversion for the reaction studied. While the counterpart model that assumes a piston type flow in the dense phase gives much better predictions of the overall conversion, the predicted concentration profiles in the individual phases exhibit poor agreement with the observed profiles.

The model of Partridge and Rowe [41] makes allowance for variable bubble sizes, velocities and the presence of clouds. Unfortunately, for the conditions of their work, over-estimation of visible bubble flow by Toomey and Johnstone's "two-phase theory" led to incompatibility between predicted cloud areas and the total bed cross section. This mechanical incompatibility prevented a direct application of these models to the reaction data obtained in their work.

The Kato and Wen bubble assemblage model [33], though better suited to represent complex hydrodynamics due to allowance for variable bubble properties, fails to account for observed end effects in the reactor. While this model was found to give the best fit for the bubble phase profile, dense phase profiles and outlet reactant concentrations were seriously over-predicted.

3.3 REACTOR MODEL OF KUNII AND LEVENSPIEL

Industrial processes are usually operated at many multiples of U_{mf}, or with $U_o / U_{mf} >> 1$ and $U_b / U_{mf} >> 1$. For this situation, Kunii and Levenspiel [31] proposed a bubbling bed model called *fine particle model*. Since $U_o >> U_{mf}$, all the feed gas passes

through the bed as bubbles, and flow through the emulsion is negligible. As shown in Fig. 4.1, fresh feed gas containing reactant A with $C_{A,i}$ and a superficial velocity enters the bed. The disappearance of A in the rising bubble phase can be expressed as

$$\begin{pmatrix} overall\ disappearance \\ in\ bubble \end{pmatrix} = \begin{pmatrix} reaction \\ in\ bubble \end{pmatrix} + \begin{pmatrix} transfer\ to \\ cloud\ -\ wake \end{pmatrix} \tag{3-1}$$

$$\begin{pmatrix} transfer\ to \\ cloud\ -\ wake \end{pmatrix} \cong \begin{pmatrix} reaction \\ in\ cloud\ -\ wake \end{pmatrix} + \begin{pmatrix} transfer\ to \\ emulsion \end{pmatrix} \tag{3-2}$$

$$\begin{pmatrix} transfer\ to \\ emulsion \end{pmatrix} \cong \begin{pmatrix} reaction \\ in\ emulsion \end{pmatrix} \tag{3-3}$$

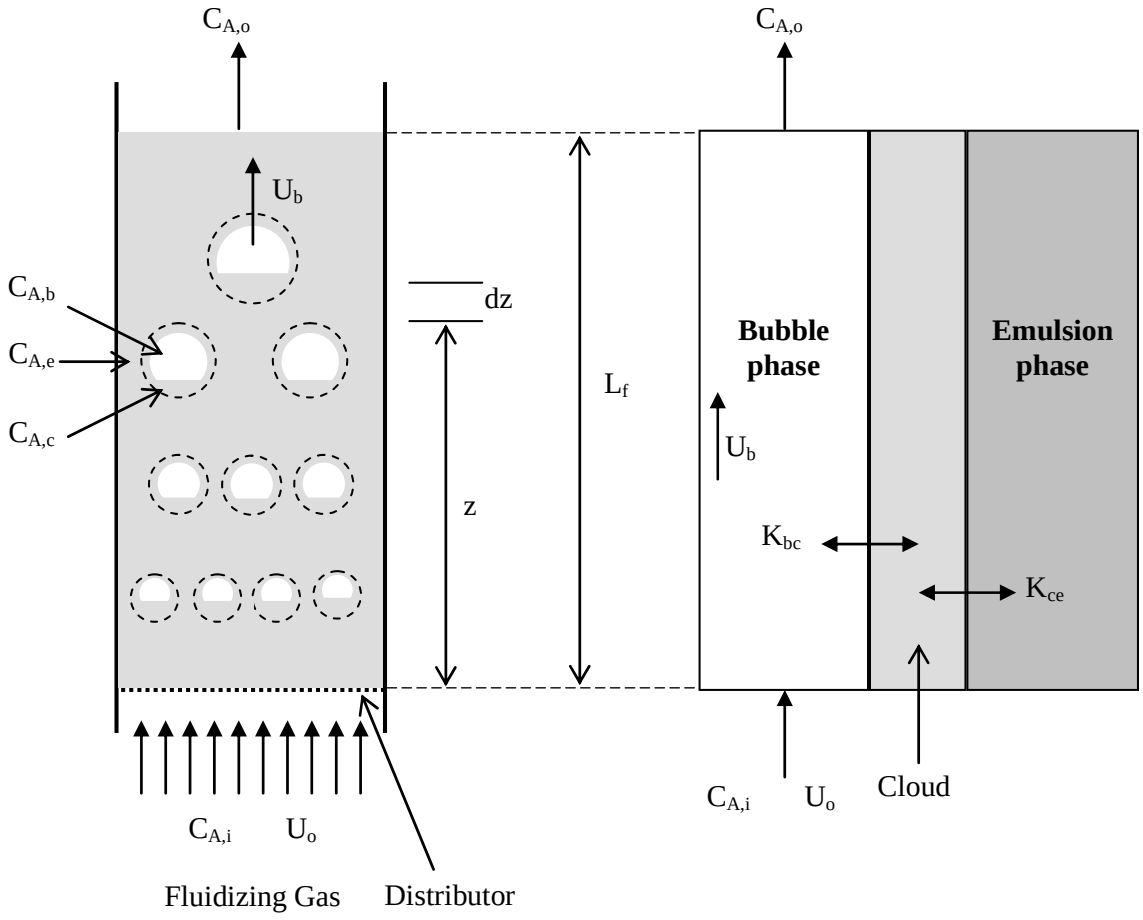

Fig. 3.1: Schematic of the Bubble Bed Model of Kunii and Levenspiel [31] for a vigorously bubbling fast bubble, thin cloud bed, U_o *and* $U_b >> U_{mf}$

These expressions may be expressed mathematically as follows,

$$-\frac{dC_{Ab}}{dt} = -U_b \frac{dC_{Ab}}{dz} = \gamma_b K_r C_{Ab} + K_{bc}\left(C_{Ab} - C_{Ac}\right) \tag{3-4}$$

$$K_{bc}\left(C_{Ab} - C_{Ac}\right) \cong \gamma_c K_r C_{Ac} + K_{ce}\left(C_{Ac} - C_{Ae}\right) \tag{3-5}$$

$$K_{ce}\left(C_{Ac} - C_{Ae}\right) \cong \gamma_e K_r C_{Ae} \tag{3-6}$$

where the fraction of solid particles dispersed in a bubble, cloud and emulsion are represented by γ_b, γ_c and γ_e, respectively.

$$\gamma_e = \frac{\left(1-\varepsilon_{mf}\right)\left(1-\delta\right)}{\delta} - \gamma_b - \gamma_c \tag{3-7}$$

$$\gamma_c = \left(1-\varepsilon_{mf}\right)\left[3\frac{\left(\frac{U_{mf}}{\varepsilon_{mf}}\right)}{\left(U_{br} - \frac{U_{mf}}{\varepsilon_{mf}}\right)} + \alpha\right] \tag{3-8}$$

Based on experimental data [33]

$\gamma_b = 0.001 - 0.010$

and

$\alpha = 0.25 - 1.00$

On the other hand [31],

$$\delta = \frac{U_o - U_{mf}}{U_b - U_{mf}} \qquad \text{For fast bubbles } (U_b > 5U_{mf}/\varepsilon_{mf}) \tag{3-9a}$$

$$\delta = \frac{U_o}{U_b} \qquad \text{For vigorously bubbling beds } (U_o >> U_{mf}) \tag{3-9b}$$

Denoting D_g as the *diffusion coefficient of gas*, the interchange coefficients between the bubble and cloud, K_{bc}, and between the cloud and emulsion, K_{ce}, are calculated as [31]

$$K_{bc} = 4.5\left(\frac{U_{mf}}{d_b}\right) + 5.85\left(\frac{D_g^{0.5} g^{0.25}}{d_b^{1.25}}\right) \tag{3-10}$$

$$K_{ce} = 6.77\left(\frac{D_g \varepsilon_{mf} U_{br}}{d_b^3}\right)^{0.5} \tag{3-11}$$

Eliminating $C_{A,c}$ and $C_{A,e}$ by combining Eqs. (3-4)-(3-6) yields

$$-U_b \frac{dC_{Ab}}{dz} = K_f C_{Ab} \tag{3-12}$$

where K_f is the overall rate constant of the bed, which accounts for all mass transfer resistance. It may be determined by [31]

$$K_f = \gamma_b K_r + \frac{1}{\frac{1}{K_{bc}} + \frac{1}{\gamma_c K_r + \frac{1}{\frac{1}{K_{ce}} + \frac{1}{\gamma_e K_r}}}} \tag{3-13}$$

Integration of Eq. (3-12) gives the concentration of the bubble at any height, z, as

$$\frac{C_{Ab}}{C_{Ai}} = exp\left(-K_f \frac{z}{U_b}\right) \tag{3-14}$$

For the entire fluidized bed as a whole, by inserting $z=L_f$, one may find the mean conversion of reactant A throughout the bed as

$$X_A = 1 - exp\left(- K_f \frac{L_f}{U_b} \right) \tag{3-15}$$

3.4 EXTENSION OF REACTOR MODEL OF KUNII AND LEVENSPIEL

Kunii and Levenspiel [31] extended their reactor model described in the preceding section and proposed two more reactor models for intermediate sized particles and large particle bubbling beds that are briefly described below.

3.4.1 Reactor Model for Intermediate Sized Particles

With fairly large particles, the bubbling bed may have behavior between the extremes of very fast and slow bubbles. A model was developed by Kunii and Levenspiel [31] to view the bed as consisting of two regions, bubble and emulsion, with just one interchange coefficient, K_{be}, to represent the transfer of gas between regions. In contrast to the fine particle model, the up-flow of gas through the emulsion is not neglected.

For a first order reaction, the disappearance of reactant gas A from two regions can be written as

$$(disappearance\ in\ bubble) = (reaction\ in\ bubble) + (transfer\ to\ emulsion) \tag{3-16}$$

$$(disappearance\ in\ emulsion) = (reaction\ in\ emulsion) + (transfer\ to\ bubble) \tag{3-17}$$

Mathematically, the above expressions become

$$-\delta U_b^* \frac{dC_{Ab}}{dz} = \delta \gamma_b K_r C_{Ab} + \delta K_{be} \left(C_{Ab} - C_{Ae} \right) \tag{3-18}$$

and

$$-(1-\delta) U_{mf} \frac{dC_{Ae}}{dz} = (1-\delta)(1-\varepsilon_{mf}) K_r C_{Ae} - \delta K_{be} \left(C_{Ab} - C_{Ae} \right) \tag{3-19}$$

In these equations the rise velocity of bubble gas is

$$U_b^* = U_b + 3U_{mf} \tag{3-20}$$

Equations (3-18) and (3-19) can be simultaneously solved to determine the overall conversion of reactant gas *A*. For the details of the solution of the above equations, the reader can refer to the textbook of Kunii and Levenspiel [31].

3.4.2 Reactor Model for Large Particles

In contrast to a fine particle bubbling bed, the up-flow of emulsion gas is faster than the rise velocity of bubbles. This is called a *slow bubble bed*. In this flow regime, a typical element of entering reactant gas rises through an emulsion, then a bubble and so on. A plug flow of gas through the bed is also assumed. Ignoring the conversion in the bubble phase, since little solid is present there, the performance of the fluidized bed in terms of the conversion of reactant *A* is expressed as

$$1 - X_A = \frac{C_{A,o}}{C_{A,i}} = exp\left[- K_r \frac{L_f (1-\varepsilon_b)}{U_o} \frac{U_{mf}}{U_o} (1-\delta) \right] \tag{3-21}$$

3.5 KINETIC MODELS FOR THE CONVERSION OF SOLIDS

Consider the following gas-solid reaction,

$$A(g) + bB(s) \xrightarrow{k} Products \tag{3-22}$$

where *A* refers to reactant gas and *B* represents the solid particle. Both reactants participate in the reaction. The solid particles may grow, shrink and remain unchanged in size during the reaction. The conversion of solids can follow one of two extremes of behavior. At one extreme, the diffusion of gaseous reactant into a particle is rapid, compared to the chemical reaction, so that solid reactant is consumed nearly uniformly

throughout the particle. This is the *uniform reaction model* [31] or *Volumetric Model (VM)*.

At the other extreme, diffusion into the reactant particle is slow, so the reaction zone advances from the outer surface into the particle, leaving behind a layer of completely converted and inert material called a product layer. This model is called the *shrinking core model (SCM)* [31].

Real situations lie between these two extremes; however, because these extremes are easy to analyze, they are used whenever possible to represent a real situation. Naturally, the first and most important consideration is to select the model that most closely represents reality, and only then should we proceed to the detailed mechanism and evaluation of the rate constants [31].

3.5.1 Uniform Reaction/Volumetric Model (VM)

The reacting gas A reacts with solid reactant everywhere in the fluidized bed reactor. As a first approximation, we may write

$$\left(rate\ of\ consumption\ of\ B\right) \propto \begin{pmatrix} concentration\ of\ A \\ covering\ the\ particle \end{pmatrix} \begin{pmatrix} amount\ of\ B \\ left\ unreacted \end{pmatrix} \tag{3-23}$$

In symbols, the rate expression becomes

$$\frac{dX_B}{dt} = K_r C_A \left(1 - X_B\right) \tag{3-24}$$

where X_B is conversion of reactant solid, and C_A is a uniform concentration of gaseous reactant. Also, K_r is the volumetric rate coefficient. Integrating Eq. (3-24) yields

$$X_B = 1 - exp\left(-K_r C_A t\right) \tag{3-25}$$

3.5.2 Shrinking Core Model (SCM)

The distinguishing feature of the conversion equations of this model is they are expressed in terms of a characteristic time, τ, the time required to completely convert an unreacted particle into product. According to *SCM*, for solids of unchanging size, the particle reaction may be controlled by either one or both of the following resistances: (1) chemical reaction, or (2) diffusion of reactant *A* through the product layer.

The conversion of X_B of an individual particle of solid depends on its length of time in the bed. However, the individual particles have different lengths of time in the bed. Thus, the mean conversion of the exit stream of solids $\overline{X}_B$ is

$$\begin{pmatrix} fraction\ of\ B \\ unconverted\ in \\ the\ exiting\ solids \end{pmatrix} = \sum_{all\ particles} \begin{pmatrix} fraction\ of\ B \\ unconverted\ in \\ particles,\ staying \\ in\ the\ reactor\ for\ time \\ between\ t\ and\ t+dt \end{pmatrix} \begin{pmatrix} fraction\ of\ exit \\ stream\ that\ stays \\ this\ length\ of\ time \\ in\ the\ reactor \end{pmatrix} \tag{3-26}$$

For *SCM-reaction controlling kinetics*,

$$1-\overline{X}_B = 1-3\left(\frac{\bar{t}}{\tau}\right)+6\left(\frac{\bar{t}}{\tau}\right)^2-6\left(\frac{\bar{t}}{\tau}\right)^3\left(1-e^{-\frac{\tau}{\bar{t}}}\right) \tag{3-27}$$

For *SCM-diffusion in product layer controlling kinetics*,

$$1-\overline{X}_B = \frac{1}{5}\left(\frac{\bar{t}}{\tau}\right)-\frac{19}{420}\left(\frac{\bar{t}}{\tau}\right)^2+\frac{41}{4620}\left(\frac{\bar{t}}{\tau}\right)^3-0.00149\left(\frac{\bar{t}}{\tau}\right)^4+\ldots \tag{3-28}$$

where $\bar{t}$ represents the mean residence time of particle solids.

3.6 CONVERSION OF BOTH SOLIDS AND GAS

The key assumption of the models for solid conversion, presented in the previous section, is that the reacting solids are covered by gas of the same mean composition.

When a reaction is slow and the concentration of gaseous reactant does not change much when passing through the bed, this approximation may be reasonable. In the general case, however, the mean gas-phase driving force in the bed is a variable that changes with operating conditions. Thus, the conversion of solid and the concentration of gaseous reactant leaving and staying within the bed are inter-dependent. A proper analysis of the bed behavior requires accounting for both changes.

Kunii and Levenspiel [31] dealt with this interaction by a three-step calculation that is applicable to solids of constant size or changing size. As the first step, a proper model should be selected, which best describes the conversion of gas. Then, another kinetic model is required for representing the conversion of solids. Finally, these two physical models must be related, with respect to the conversion of gaseous reactant *A* and that of solid reactant *B*. Therefore, a variety of combinations of the previously described models may be encountered. As a result, the designer of non-catalytic gas-solid reactors would need to carry out tedious calculations, based on the Kunii and Levenspile method [31].

3.7 A NEW GAS-SOLID REACTOR MODEL

Catalytic gas-solid reactions (CGSRs) have been widely studied and there are various models describing conversion of a gaseous reactant in a fluidized bed reactor, while the solid particles do not participate in the reactions. These models are generally based on two-phase theory, as the most well-known models reviewed previously. Nevertheless, expansion of these models to non-catalytic gas-solid reactions (NCGSRs) is difficult, since solid particles take part in the reaction as well. In such a situation, one may employ the method of Kunii and Levenspile [31], explained in the preceding sections. As mentioned, however, it would require a combination of physical models for a catalytic gas-solid reaction and those for solid reaction kinetics.

Very recently, a generalized method to analyze NCGSR has been presented by Gomez-Barea et al. [43] for an isothermal fluidized bed reactor, where only one reaction takes place. They developed a model in two stages. First, a method for an evaluation of gas conversion was formulated by applying the two-phase theory of fluidization, in fluidized bed catalytic reactors, in which only gas conversion is considered. In a second stage, the model was extended to account for non-catalytic reactions by incorporating a

variation of particle properties and a reaction rate with conversion, as well as the distribution of the conversion of reacting particles in the bed. The method of Gomez-Barea et al. [43] is briefly explained below.

3.7.1 Reactor Model for CGSR

Consider that gaseous reactant A at concentration C_{Ai} is fed into the bed reactor, which consists of bubble and emulsion phases. It is transferred from the bubble phase (with C_{Ab}) to the emulsion phase (with C_{Ae}) to react with particles. It is assumed that a solid particle S is made up of an active reactant solid particle C, and non-reactive material D. The transport resistances are: bubble to emulsion resistance, external film resistance around the solid particle, and inter-particle resistance. The reactor contains particles that have spent different times inside the bed, and hence they have a wide distribution of conversion, represented by $p_b(x_c)$. As a first step, a fluid-dynamic model is applied to a catalytic system.

Defining the gas conversion, X_g, and inter-phase effectiveness factor, η_{ph} as

$$X_g = 1 - \frac{C_{Ao}}{C_{Ai}} \tag{3-29}$$

$$\eta_{ph} = \left(\frac{C_{Ae}}{C_{Ai}} \right)^n \tag{3-30}$$

one may calculate the gas conversion by

$$X_g = \left(1 - \eta_{ph}^{1/n}\right) N_a \tag{3-31}$$

where n denotes the order of reaction, and

$$N_a = \frac{C_{Ai} - C_{Ao}}{C_{Ai} - C_{Ae}} = 1 - \beta \, exp\left(- \frac{NTU}{\beta} \right) \tag{3-32}$$

$$NTU = \frac{K_{be}\varepsilon_b}{U_o / L_f} \tag{3-33}$$

$$K_{be} = \left(\frac{1}{K_{bc}} + \frac{1}{K_{ce}} \right)^{-1} \tag{3-34}$$

$$\beta = \frac{U_o - U_{mf}}{U_o} \tag{3-35}$$

The expression for β assumes that all gas in excess of the minimum fluidization velocity flows though the bed in the form of bubbles.

3.7.2 Extension of the Reactor Model for NCGSR

At the next step, allowance is made for the deviation from the catalytic case, considering the extent of conversion in the fluidized bed by a solid population balance. Here, it is assumed that all fine particles are returned to the reactor and there is no carryover. Furthermore, it is assumed that all particles enter the bed with the same conversion x_{c0}, and they are removed from the reactor with $x_{c,b}$ (average conversion of perfectly mixed particles in the bed). This approach expresses the equations in terms of the conversion, rather than time or particle size. The outlet conversion of solids, $x_{c,b}$ may be expressed in terms of the fraction of C in the bed, $Y_{c,b}$, as

$$x_{c,b} = \frac{Y_{c0} - Y_{c,b}}{Y_{c,0}\left(1 - Y_{c,b}\right)} \tag{3-36}$$

where Y_{c0} is inlet mass fraction of solid reactant.

A population balance over the reactor yields the distribution of the solids conversion.

$$p_b(x_c) = \frac{1}{Da_s}\frac{1}{F(x_c)}\frac{1-Y_{c0}x_c}{1-Y_{c0}x_{c0}}exp\left[-\frac{\Theta(x_c)}{\lambda}\right] \tag{3-37}$$

$$\Theta(x_c) = \int_{x_{c0}}^{x_c}\frac{ds}{F(s)} \tag{3-38}$$

Here Da_s and λ are dimensionless parameters that are defined as

$$Da_s = \frac{K_{r,e}W_b}{F_0} = K_{r,e}\bar{t} \tag{3-39}$$

$$\lambda = \frac{K_{r,e}W_b}{F_1} = \frac{K_{r,e}W_b}{F_0 - r_{c,bed}} \tag{3-40}$$

Also, $F(x_c)$ is a function expressing the dependence of the conversion rate of a single particle on x_c, at any particle effectiveness factor, η_p.

$$F(x_c) = \eta_p F_i(x_c) \tag{3-41}$$

Table 3.1 shows two well-known kinetic model extremes for $F_i(x_c)$ and $\Theta(x_c)$: Volumetric Model (VM), and Grain Model (GM) or Shrinking Core Model (SCM). In Eqs. (3-39) and (3-40), $K_{r,e}$ is the kinetic coefficient, which accounts for the concentration of the gaseous reactant and temperature in the emulsion. It can be calculated by

Table 3.1: Two extremes of kinetic models for NCGSR

MODEL NAME	$F_I(X_C)$	$\Theta(X_C)$
Volumetric Model (VM)	$1-x_c$	$-\ln(1-x_c)$
Grain Model (GM), or Shrinking Core Model (SCM)	$(1-x_c)^{2/3}$	$-3[1-(1-x_c)^{1/3}]$

Source: Refs. [43, 44]

$$K_{r,e} = b\frac{M_p}{\rho_p}k_0 C_{Ae}^n \tag{3-42}$$

where k_0 is the kinetic coefficient based, on the particle volume, determined at the inlet conditions.

The overall mass rate of reaction within the bed, represented by $r_{c,bed}$ may be calculated by

$$r_{c,bed} = \int_{x_{c0}}^{1} W_b R(s) p_b(s) ds \tag{3-43}$$

Where $R(x_c)$ is the reactivity defined as

$$R(x_c) = \frac{Y_{c0}K_{r,e}}{1 - Y_{c0}x_c} F(x_c) \tag{3-44}$$

A combination of Eqs. (3-39) and (3-40) yields

$$r_{c,bed} = \left(1 - \frac{Da_s}{\lambda}\right) F_0 \tag{3-45}$$

Based on a mass balance of non-reacted material of solid particle *S*, and combining it with the conversion distribution of solids, $p_b(x_c)$, i. e. Eq. (3-37), it can be shown that

$$\left(\frac{Da_s}{\lambda}\right) = \frac{f_1(x_{c0}, \lambda) + (1/Y_{c0} - 1)}{1/Y_{c0} - x_{c0}} \tag{3-46}$$

where

$$f_1(x_{c0}, \lambda) = \int_{x_{c0}}^{1} \frac{1-s}{F(s)} exp\left[-\frac{\Theta(s)}{\lambda}\right] ds \tag{3-47}$$

The conversions of solid particles and gaseous reactant may be related through an overall mass balance on the solid particles and gaseous reactant, and the stoichiometry of the reaction, *b*. Thus, one may find the following expression for gas conversion by equaling the rate of disappearance of solid particles, with the rate of consumption of gaseous reactant.

$$X_g = \frac{1}{\alpha}\left(1 - \frac{Da_s}{\lambda}\right) \tag{3-48}$$

$$\alpha = b\frac{U_o A_{c,bed} C_{Ai} M_p}{F_0} \tag{3-49}$$

An expression may be derived to evaluate the inter-phase effectiveness factor, η_{ph}, by combining Eqs. (3-31) and (3-48) as follows.

$$\eta_{ph} = \left[1 - \frac{1}{N_a \alpha}\left(1 - \frac{Da_s}{\lambda}\right)\right]^n \tag{3-50}$$

Taking into account the average conversion of solid particles within the bed, $x_{c,b}$, in Eq. (3-36) and solving the distribution function, $p_b(x_c)$, over the bed results in

$$x_{c,b} = 1 - \frac{f_1(x_{c0}, \lambda)}{\lambda} \tag{3-51}$$

Combining Eqs. (3-47) and (3-51) to eliminate $f_1(x_{c0}, \lambda)$ and combining the result with Eq. (3-48) yields the following expression, which relates the conversion of gaseous reactant to that of solid particles as follows,

$$X_g = \frac{x_{c,b} - x_{c0}}{\alpha(1/Y_{c0} - x_{c0})} \tag{3-52}$$

In the next chapter, a solution algorithm will be described to solve these coupled non-linear equations.

Chapter 4

Solution Methodology for Cupric Chloride System

4.1 INTRODUCTION

This chapter focuses on transport phenomena of reactions of cupric chloride particles ($CuCl_2$) with steam at elevated temperatures (~ 400 ^{0}C) within a fluidized bed reactor (Fig. 4.1). The analysis is presented in three sections. The first part investigates the Gibbs free energy of the reaction. The second part gives the method of hydrodynamic analysis, along with a calculation procedure. Lastly, the fluidized bed model, is presented for two limiting extremes, a Volumetric Model (VM) and Shrinkage Core Model (SCM), as well as an algorithm for each case that allows an evaluation of conversion of cupric chloride particles and steam in a given process condition.

4.2 GIBBS FREE ENERGY OF REACTION

As previously shown in Table 1.1, the stoichiometry of the reaction is

$$2CuCl_2 + H_2O \rightarrow CuO*CuCl_2 + 2HCl \tag{4-1}$$

which is the forth step in the thermochemical copper-chlorine cycle for hydrogen production (see Fig. 1.1). It is assumed that $CuCl_2$ particles and superheated steam are fed at the same temperature, e. g. 400 ^{0}C, and the fluidized bed reactor experiences an approximately isothermal reaction as both of the reactants participate in the reaction. As depicted in Fig. 4.1, gaseous HCl and melanothallite particles ($CuO*CuCl_2$) are the only products of the bed reactor, assuming the cupric chloride and steam are perfectly converted.

The reaction given by Eq. (4-1) is an endothermic reaction, so a certain amount of heat is required to supply the reaction. The change in Gibbs free energy associated with the reaction in Eq. (4-1) may be defined as

$$\Delta\overline{G} = \Delta\overline{H}_f - T\Delta\overline{S} \tag{4-2}$$

where the "over bar" refers to a molar value. Also, changes in the enthalpy of formation and the entropy of the reaction are described as

$$\begin{aligned}\Delta\overline{H}_f &= \overline{H}_{f|Products} - \overline{H}_{f|Reactants} \\ &= \left(\overline{H}_{f,CuO*CuCl_2} + 2\overline{H}_{f,HCl}\right) - \left(2\overline{H}_{f,CuCl_2} + \overline{H}_{f,H_2O}\right)\end{aligned} \tag{4-3}$$

$$\begin{aligned}\Delta\overline{S} &= \overline{S}_{|Products} - \overline{S}_{|Reactants} \\ &= \left(\overline{S}_{CuO*CuCl_2} + 2\overline{S}_{HCl}\right) - \left(2\overline{S}_{CuCl_2} + \overline{S}_{H_2O}\right)\end{aligned} \tag{4-4}$$

The molar enthalpy of formation at a temperature T is given by [45]

$$\overline{H}_T = \overline{H}_{298.15} + \int_{298.15}^{T} \overline{c}_P \, dT \tag{4-5}$$

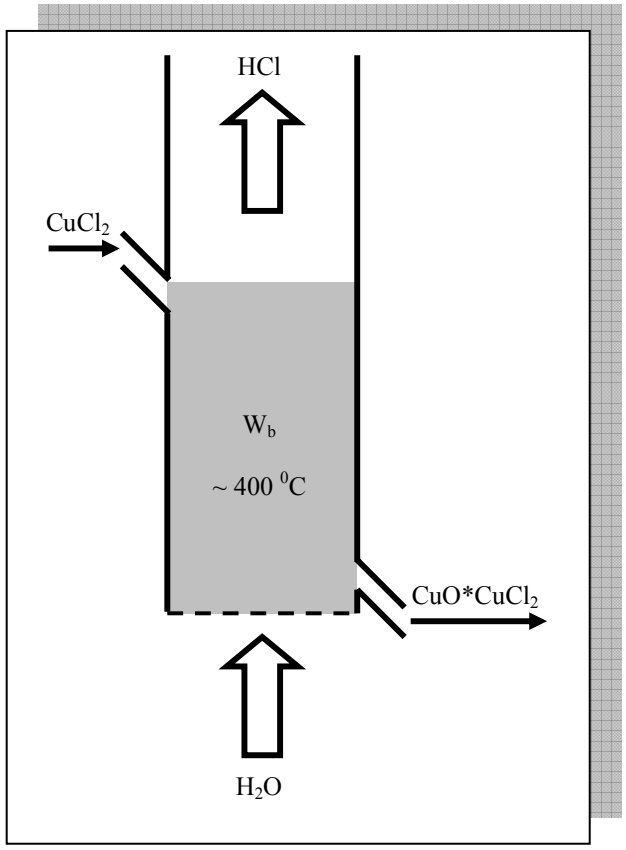

Fig. 4.1: Schematic of an inlet/outlet of a fluidized bed, where a reaction of cupric chloride with steam takes place at an elevated temperature.

The molar entropy is given by [45]

$$\overline{S}_T = \overline{S}_{298.15} + \int_{298.15}^{T} \frac{\overline{c}_P}{T} dT \tag{4-6}$$

The molar specific heat at constant pressure, $\overline{c}_p$, is given as a function of the temperature for various substances by NIST [46]. The NIST data for molar specific heats was used in this thesis.

Figure 4.2 shows the variation of enthalpy of formation and the entropy of reaction of cupric chloride with steam at varying temperatures. The change in Gibbs free energy is also illustrated in Fig. 4.3. At 375^0C, the value of ΔG (31.6 kJ/mole) given by Lewis [47]

is close to the computed value in this thesis. The reaction of $CuCl_2$ with steam is thermodynamically viable based on the valuehs of the Gibbs free energy.

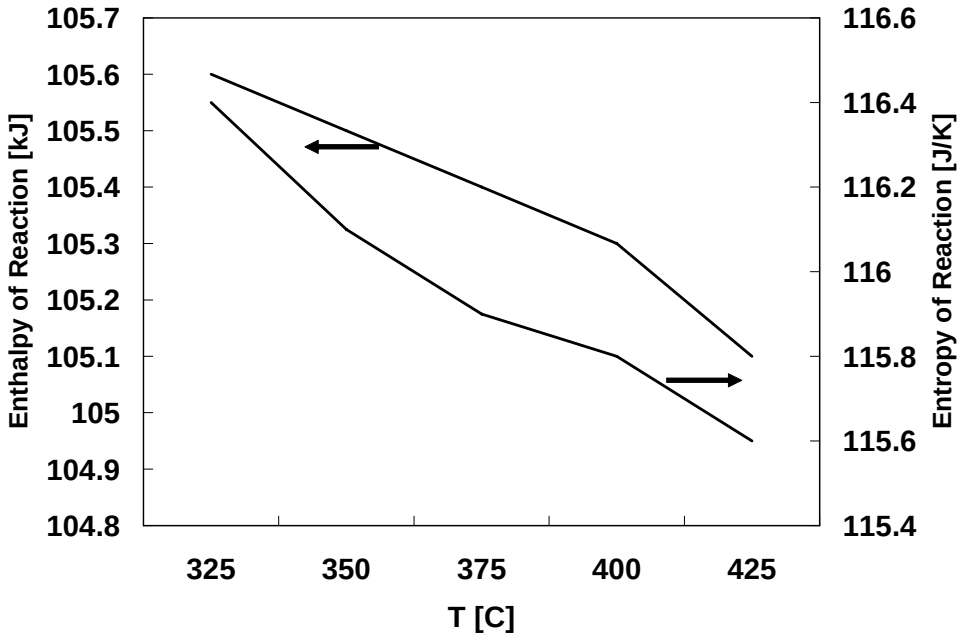

Fig. 4.2: Enthalpy of formation and entropy of reaction of cupric particles with superheated steam at various reaction temperatures.

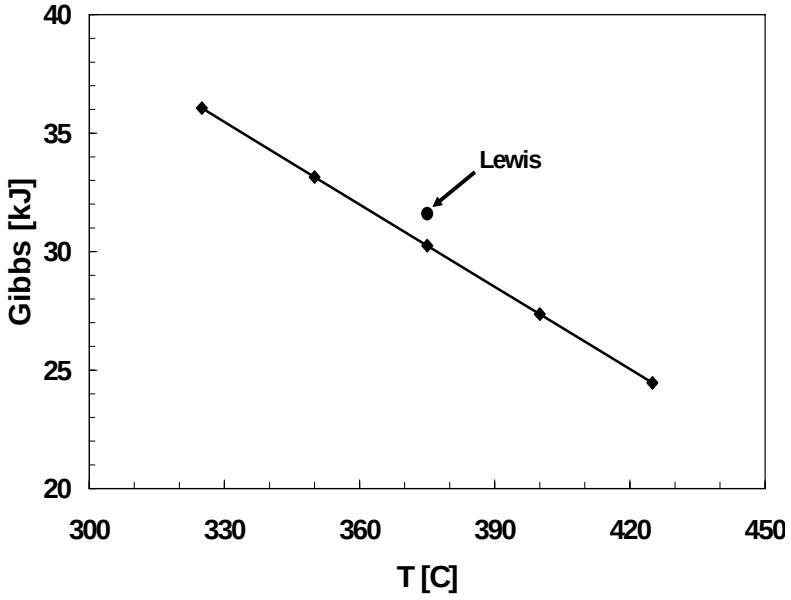

Fig. 4.3: Gibbs free energy for the reaction of cupric chloride particles with steam at various reaction temperatures. The marker in the figure is a value given by Lewis [47].

4.3 HYDRODYNAMIC ANALYSIS OF A FLUIDIZED BED

A key and essential step before studying the detailed transport phenomena of reactions of $CuCl_2$ particles with superheated steam in a fluidized bed reactor is to investigate hydrodynamic behavior in the bed. The hydrodynamics analysis examines the interaction of key parameters, such as the bubble diameter, bed void fraction, bed height, minimum fluidization velocity, etc. Furthermore, fluid-dynamics parameters are also needed when studying the bed performance, with respect to the conversion of reactants at a given process condition. This section employs the correlations introduced in Chapter 2, and develops a solution procedure to determine the hydrodynamic parameters that will be needed in the mass transport analysis.

4.3.1 Bed Height

Figure 4.4 shows schematically the fluidized bed reactor. Given a bed inventory, W_b, the bed height at the minimum fluidization condition can be determined from Eq. (2-10) as follows.

$$L_{mf} = \frac{W_b}{\rho_p \left(1 - \varepsilon_{mf}\right)\left(\pi D_t^2 / 4\right)} \tag{4-7}$$

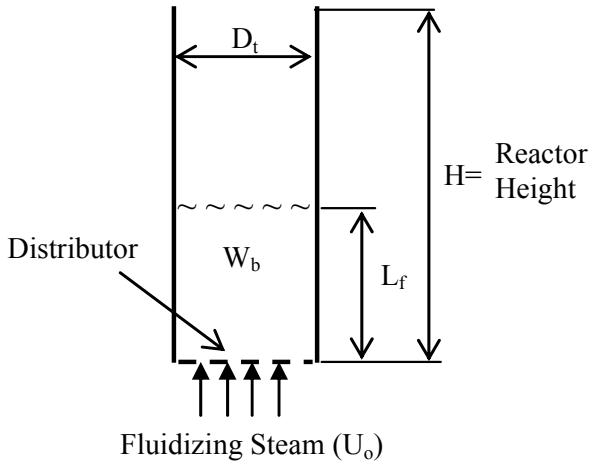

Fig. 4.4: Schematic diagram of a fluidized bed reactor.

Hence, the bed height, L_f, may be computed using Eq. (2-21) as follows,

$$L_f = L_{mf}\frac{1-\varepsilon_{mf}}{1-\varepsilon_b} \tag{4-8}$$

4.3.2 Bubble Average Diameter

The local bubble diameter, d_p, at a given height above the distributor (z) can be calculated using Eq. (2-13) as follows.

$$d_b = d_{bm} - (d_{bm} - d_{b0})exp\left(-0.3\frac{L_f}{D_t}z\right) \tag{4-9}$$

where d_{bm} and d_{b0} are the limiting bubble size defined in Eqs. (2-14) and (2-15), respectively. One may now obtain the average bubble diameter throughout the bed by integrating Eq. (4-9) along the bed height as follows.

$$d_{b,ave} = \frac{1}{L_f}\int_0^{L_f} d_b dz \tag{4-10}$$

In order to find the average bubble diameter, substitute Eq. (4-9) into Eq. (4-10), and solve the resulting integral,

$$\begin{aligned} d_{b,ave} &= \frac{1}{L_f}\int_0^{L_f}\left[d_{bm} - (d_{bm} - d_{b0})exp\left(-0.3\frac{L_f}{D_t}z\right)\right]dz \\ &= \frac{1}{L_f}\int_0^{L_f} d_{bm}dz - \int_0^{L_f}\left[(d_{bm} - d_{b0})exp\left(-0.3\frac{L_f}{D_t}z\right)\right]dz \\ &= d_{bm}z\Big|_0^{L_f} - \left(-\frac{D_t}{0.3L_f}\right)(d_{bm} - d_{b0})exp\left(-0.3\frac{L_f}{D_t}z\right)\Bigg|_0^{L_f} \Rightarrow \end{aligned}$$

$$d_{b,ave} = d_{bm} + \left(\frac{D_t}{0.3L_f^2} \right) \left(d_{bm} - d_{b0} \right) \left[exp\left(-0.3 \frac{L_f^2}{D_t} \right) - 1 \right] \tag{4-11}$$

4.3.3 Solution Procedure

The bed height, average bubble diameter and bed porosity will be required for transport phenomena analysis of the bed. A solution flowchart is thus developed for determining these parameters, as illustrated in Fig. 4.5. This flowchart will be used in this work to study the hydrodynamics of the fluidized bed, both individually and when analysing the transport phenomena of the reactor. As shown in Fig. 4.5, an evaluation of bed properties may be carried out by trial-and-error. In estimating the bubble rise velocity (U_{br}) and bubble velocity (U_b), the average bubble diameter is utilized. Since the difference between reactants densities is greater than 3,000kgm^{-3} (as $\rho_{H_2O} = 0.326$ kgm^{-3} at 400^{0}C and 1bar, and $\rho_{CuCl_2} = 3{,}400$ kgm^{-3}), and considering the particle mean diameter in the range of 100-700μm, the reactant solid particles belong to group **B** in Geldart's particle classification (see Fig. 2.2). Thus, Eq. (2-20) is used to evaluate the bubble velocity.

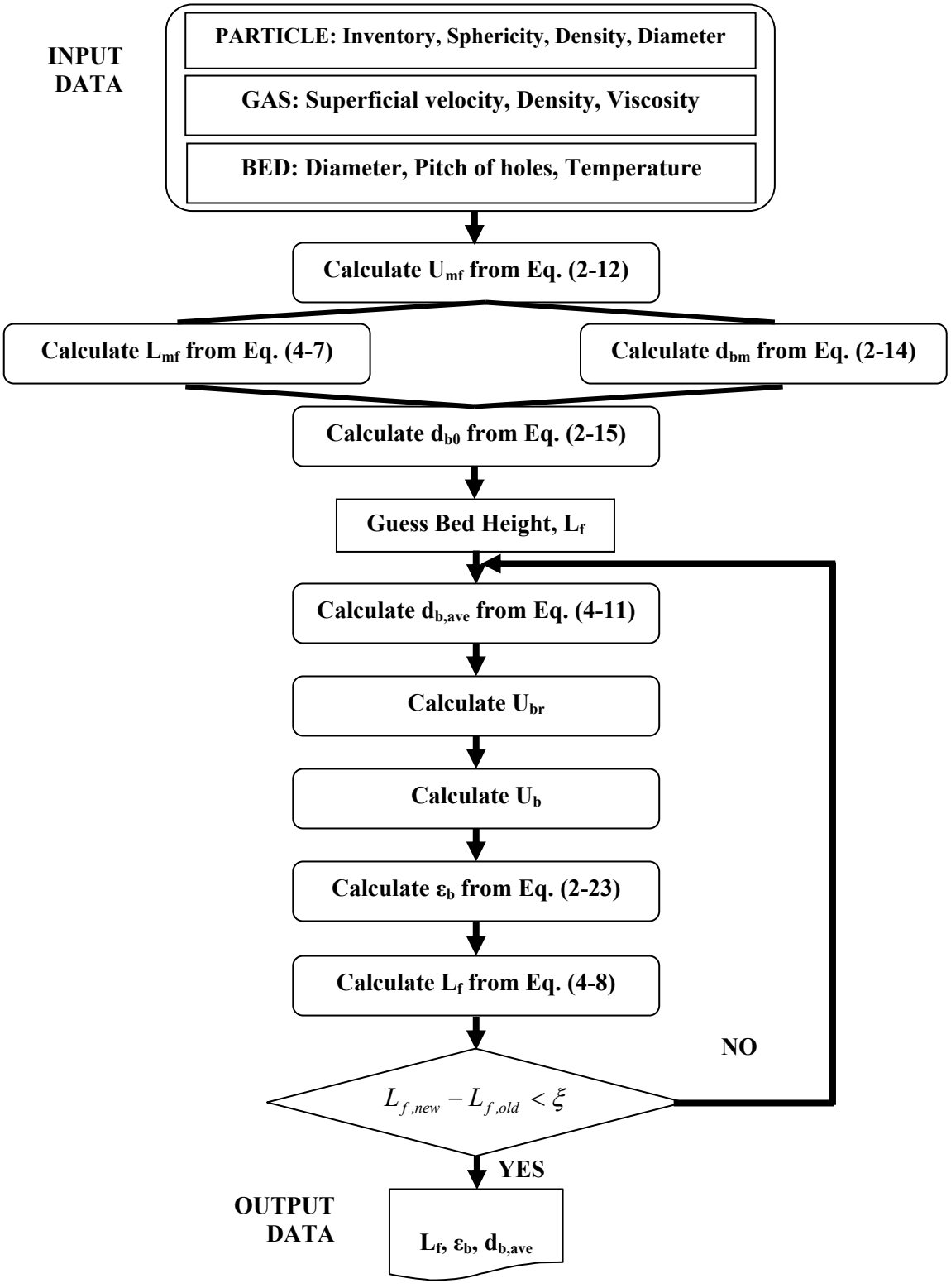

Fig. 4.5: Solution flowchart for evaluating the bed properties.

4.4 FLUIDIZED BED MODEL

Since both cupric chloride particles and steam take part in the reaction, it is necessary to apply a Non-Catalytic Gas-Solid Reaction (*NCGSR*) model to analyze the bed performance. The following assumptions are applied for analyzing the bed performance.

- The bed consists of two regions according to two-phase theory: a bubble phase, and emulsion phase.
- The temperature gradient within the bed reactor is negligible, so it experiences an isothermal process.
- There exists merely one reaction, namely the reaction of cupric particles with superheated steam.
- The reaction takes place in the emulsion phase.

Based on these assumptions, the general NCGSR model of Gomez-Barea et al. [43], introduced in section 3.6 is utilized to describe the behavior of the reactor. Their model is simpler and more straightforward compared to the model of Kunii and Levenspiel presented in the preceding chapter. Another advantage of this model is that the distribution of solid particle conversion is taken into account throughout the bed.

One crucial issue that must be identified in this stage is the nature and kinetics of the reaction of cupric chloride particles, which is not well-known. This important issue needs experimental data. For the purpose of the present study, however, two idealized extreme cases will be examined: (1) Volumetric Model (VM), and (2) Grain or Shrinking Core Model (SCM).

4.4.1 Rate of Cupric Chloride Reactions

In addition to the assumptions mentioned earlier, for the case of the present work, the followings approximations are also used.

- Unlike the assumption of Gomez-Barea et al. [43], there exists only one type of particle, that reacts with fluidizing gas, and there is no non-reacting material, so Y_c=1.
- The conversion of particles at the inlet of the reactor is zero; x_{c0}=0.
- The analysis assumes that the reaction is *first-order*.

The key point in determining the reactant conversions is that the ratio (Da_s / λ) should be computed by Eq. (2-46), which depends on $f_1(x_{c0}, \lambda)$ defined in Eq. (2-47). However, the integral appearing in Eq. (2-47) is cumbersome, particularly since it can not be solved analytically for complicated kinetic model functions, such as SCM (see Table 2.1). An alternative way to calculate (Da_s / λ) may be Eq. (2-45) so

$$\frac{Da_s}{\lambda} = 1 - \frac{r_{c,bed}}{F_0} \tag{4-12}$$

The overall rate of reaction, $r_{c,bed}$, must be determined from Eq. (3-43), taking into account Eqs. (3-37) and (3-44),

$$r_{c,bed} = \int_{x_{c0}}^{1} W_b R(s) p_b(s) ds \Rightarrow$$

$$r_{c,bed} = \int_{x_{c0}}^{1} W_b \left[\frac{Y_{c0} K_{r,e}}{1 - Y_{c0} s} F(s) \right] \left\{ \frac{1}{Da_s} \frac{1}{F(s)} \frac{1 - Y_{c0} s}{1 - Y_{c0} x_{c0}} exp\left[-\frac{\Theta(s)}{\lambda} \right] \right\} ds \Rightarrow$$

$$r_{c,bed} = \left(\frac{W_b K_{r,e}}{Da_s} \right) \left(\frac{Y_{c0}}{1 - Y_{c0} x_{c0}} \right) \int_{x_{c0}}^{1} exp\left[-\frac{\Theta(s)}{\lambda} \right] ds \tag{4-13}$$

In past work of Gomez-Barea et al. [43], the integral part of the above expression is written as

$$f_2(x_{c0}, \lambda) = \int_{x_{c0}}^{1} exp\left[-\frac{\Theta(s)}{\lambda} \right] ds \tag{4-14}$$

Hence, substituting Eq. (4-14) into Eq. (4-13) and taking into consideration Eq. (3-39), it can be shown that

$$r_{c,bed} = F_0\left(\frac{Y_{c0}}{1-Y_{c0}x_{c0}}\right)f_2\left(x_{c0},\lambda\right) \tag{4-15}$$

So, combining Eqs. (4-12) and (4-15) yields

$$\frac{Da_s}{\lambda} = 1-\left(\frac{Y_{c0}}{1-Y_{c0}x_{c0}}\right)f_2\left(x_{c0},\lambda\right) \tag{4-16}$$

There is a discrepancy between the resulted expression for $\left(Da_s/\lambda\right)$ in Eq. (4-16) and the result presented by Gomez-Barea et al. [43]; since the latter equation is

$$\frac{Da_s}{\lambda} = \frac{1}{\lambda}-\left(\frac{Y_{c0}}{1-Y_{c0}x_{c0}}\right)f_2\left(x_{c0},\lambda\right) \tag{4-17}$$

Equation (4-16) is derived differently here than Ref. [43]. Considering Y_{c0}=1, x_{c0}=0, the ratio $\left(Da_s/\lambda\right)$ may be expressed as

$$\frac{Da_s}{\lambda} = 1-f_2\left(\lambda\right) = 1-\int_0^1 exp\left[-\frac{\Theta(s)}{\lambda}\right]ds \tag{4-18}$$

4.4.2 Volumetric Model

In this model, the conversion rate of particles is proportional to the conversion of the particle. From Table 3.1, the kinetic functions are

$$F_i\left(x_c\right) = 1-x_c \tag{4-19}$$

$$\Theta\left(x_c\right) = -ln\left(1-x_c\right) \tag{4-20}$$

Hence,

$$f_2(\lambda)=\int_0^1 exp\left[-\frac{\Theta(s)}{\lambda}\right]ds=\int_0^1 exp\left[\frac{ln(1-s)}{\lambda}\right]ds=\int_0^1 exp\left[ln(1-s)^{\frac{1}{\lambda}}\right]ds$$

$$=\int_0^1\left[(1-s)^{\frac{1}{\lambda}}\right]ds \tag{4-21}$$

The solution for the above integral becomes

$$f_2(\lambda)=\frac{\lambda}{\lambda+1} \tag{4-22}$$

So, the ratio (Da_s/λ) is calculated for the Volumetric Model (VM) by substituting Eq. (4-22) into Eq. (4-18) as

$$\frac{Da_s}{\lambda}=\frac{1}{\lambda+1} \tag{4-23}$$

Solving Eq. (4-23) with respect to λ results in

$$\lambda=\frac{Da_s}{1-Da_s} \tag{4-24}$$

Moreover, the overall rate of the reaction can be determined in this model, by combining Eqs. (4-12) and (4-23), yielding

$$r_{c,bed}=F_0\left(\frac{\lambda}{\lambda+1}\right) \tag{4-25}$$

A solution procedure is needed herein to evaluate conversions of $CuCl_2$ particles and steam, assuming that the particle conversion takes place in accordance with VM, which is illustrated in Fig. 4.6. As shown in this figure, conversion of the reactants may be evaluated through trial-and-error.

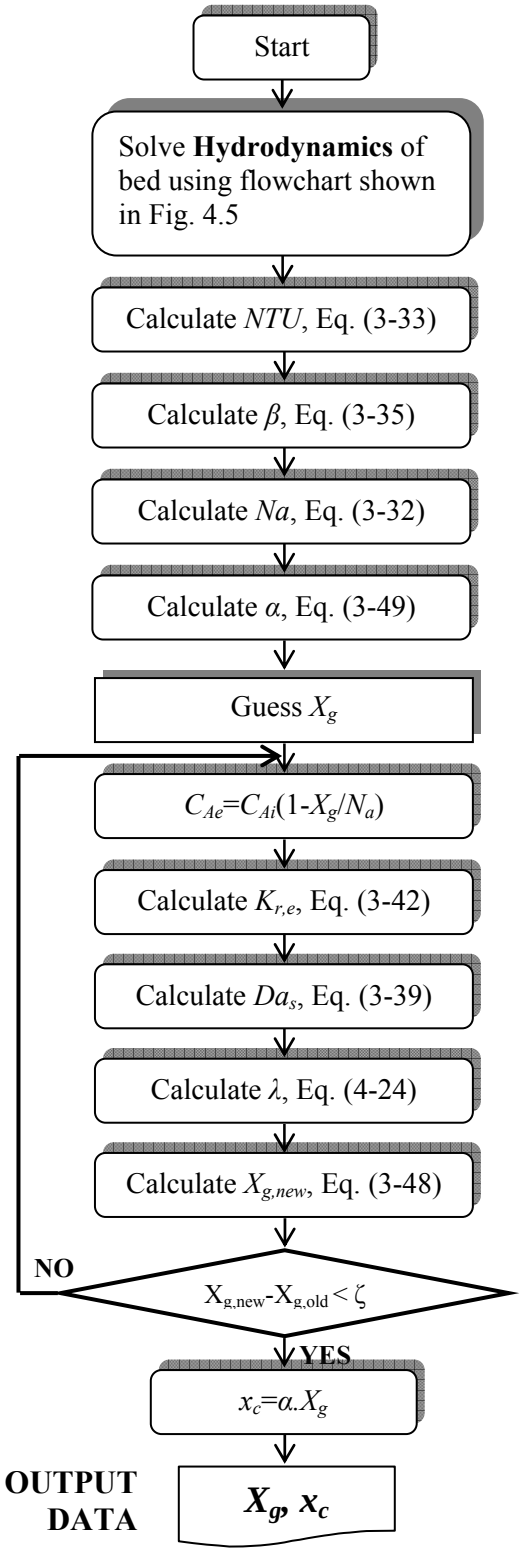

Fig. 4.6: Solution procedure for determining $CuCl_2$ and steam conversions, assuming a *Volumetric Model* (*VM*) for kinetics of the particle consumption.

4.4.3 Shrinking Core Model

The shrinking core model (SCM) is a limiting extreme that will also be considered in this study. Assuming that the particle consumption follows SCM, the kinetic functions are (see Table 3.1)

$$F_i(x_c) = (1 - x_c)^{2/3} \tag{4-26}$$

$$\Theta(x_c) = 3\left[1 - (1 - x_c)^{1/3}\right] \tag{4-27}$$

Hence, $f_2(\lambda)$ in Eq. (4-19) becomes

$$f_2(\lambda) = \int_0^1 exp\left\{-\frac{3}{\lambda}\left[1 - (1 - s)^{1/3}\right]\right\} ds \tag{4-28}$$

Defining a slack variable such that S=1-s, the above integral becomes

$$f_2(\lambda) = \int_0^1 exp\left[-\frac{3}{\lambda}\left(1 - S^{1/3}\right)\right] dS \tag{4-29}$$

Defining a second slack variable as

$$X = \frac{3}{\lambda}\left(1 - S^{1/3}\right) \tag{4-30}$$

Then Eq. (4-29) gives

$$f_2(\lambda) = \lambda \int_0^{3/\lambda} \left(1 - \frac{\lambda}{3} X\right)^2 exp(-X) dX$$

$$= \lambda \int_0^{3/\lambda} \left[1 - \frac{2\lambda}{3} X + \left(\frac{\lambda}{3} \right)^2 X^2 \right] exp(-X) dX \Rightarrow$$

$$f_2(\lambda) = \lambda \int_0^{3/\lambda} \left[exp(-X) - \left(\frac{2\lambda}{3} \right) X \, exp(-X) + \left(\frac{\lambda}{3} \right)^2 X^2 \, exp(-X) \right] dX \tag{4-31}$$

The resulting integral can be expressed with three parts as

$$I_1 = \int_0^{3/\lambda} exp(-X) dX = 1 - exp\left(-\frac{3}{\lambda} \right) \tag{4-32}$$

$$I_2 = \left(\frac{2\lambda}{3} \right) \int_0^{3/\lambda} X \, exp(-X) dX = \left(\frac{2\lambda}{3} \right) \left[1 - \left(\frac{3}{\lambda} \right) exp\left(-\frac{3}{\lambda} \right) - exp\left(-\frac{3}{\lambda} \right) \right] \tag{4-33}$$

$$\begin{aligned} I_3 &= \left(\frac{\lambda}{3} \right)^2 \int_0^{3/\lambda} X^2 \, exp(-X) dX \\ &= \left(\frac{\lambda}{3} \right)^2 \left[2 - \left(\frac{3}{\lambda} \right)^2 exp\left(-\frac{3}{\lambda} \right) - 2\left(\frac{3}{\lambda} \right) exp\left(-\frac{3}{\lambda} \right) - 2\, exp\left(-\frac{3}{\lambda} \right) \right] \end{aligned} \tag{4-34}$$

Hence, substituting Eqs. (4-32)-(4-34) into Eq. (4-31) gives

$$\begin{aligned} f_2(\lambda) = \lambda(I_1 - I_2 + I_3) = &\left[\lambda - \lambda \, exp\left(-\frac{3}{\lambda} \right) \right] - \left[\frac{2\lambda^2}{3} - 2\lambda \, exp\left(-\frac{3}{\lambda} \right) - \left(\frac{2\lambda^2}{3} \right) exp\left(-\frac{3}{\lambda} \right) \right] + \\ &\left[\frac{2\lambda^3}{9} - \lambda \, exp\left(-\frac{3}{\lambda} \right) - \left(\frac{2\lambda^2}{3} \right) exp\left(-\frac{3}{\lambda} \right) - \left(\frac{2\lambda^3}{9} \right) exp\left(-\frac{3}{\lambda} \right) \right] \Rightarrow \end{aligned}$$

$$f_2(\lambda) = \lambda \left[\left(1 - \frac{\lambda}{3} \right)^2 + \left(\frac{\lambda}{3} \right)^2 - 2\left(\frac{\lambda}{3} \right)^2 exp\left(-\frac{3}{\lambda} \right) \right] \tag{4-35}$$

Combining Eqs. (4-12), (4-19) and (4-35) yields

$$r_{c,b} = F_0 \lambda \left[\left(1 - \frac{\lambda}{3}\right)^2 + \left(\frac{\lambda}{3}\right)^2 - 2\left(\frac{\lambda}{3}\right)^2 exp\left(-\frac{3}{\lambda}\right) \right] \tag{4-36}$$

Likewise, a solution procedure is developed for evaluating the conversions of $CuCl_2$ particles and steam, assuming that the particle conversion takes place in accordance with SCM, which is depicted in Fig. 4.7. In comparison with the numerical algorithm presented for the case of VM (Fig. 4.6), the solution method for SCM requires two trial-and-error loops as illustrated in Fig. 4.7.

4.5 FLUIDIZED BED EFFECTIVENESS

Utilizing a fluidized bed in a hydrogen production plant (see Fig. 1.1) provides a condition under which $CuCl_2$ and steam are reacted. It is worth defining a factor representing the effectiveness of the fluidized bed reactor. According to the stoichiometry of the reaction (Eq. (4-1)), two moles of $CuCl_2$ are reacted with one mole of steam. The best performance of the bed occurs when all three moles of reactants (two moles of $CuCl_2$ + one mole of steam) convert to products, so there will be no $CuCl_2$ or steam at the exit. Thus, the *Bed Effectiveness* represented by η_{bed} may be described as

$$\eta_{bed} = \frac{Total\ moles\ of\ reactants\ converted\ to\ products}{Total\ reactant\ moles\ at\ the\ inlet\ streams} \tag{4-37a}$$

$$\eta_{bed} = 1 - \frac{Total\ non\text{-}reacted\ reactant\ moles}{Total\ reactant\ moles\ at\ the\ inlet\ streams} \tag{4-37b}$$

$$\eta_{bed} = 1 - \frac{Total\ reactant\ moles\ at\ the\ outlet\ streams}{Total\ reactant\ moles\ at\ the\ inlet\ streams} \tag{4-37c}$$

In symbols, Eq. (4-37c) can be expressed as

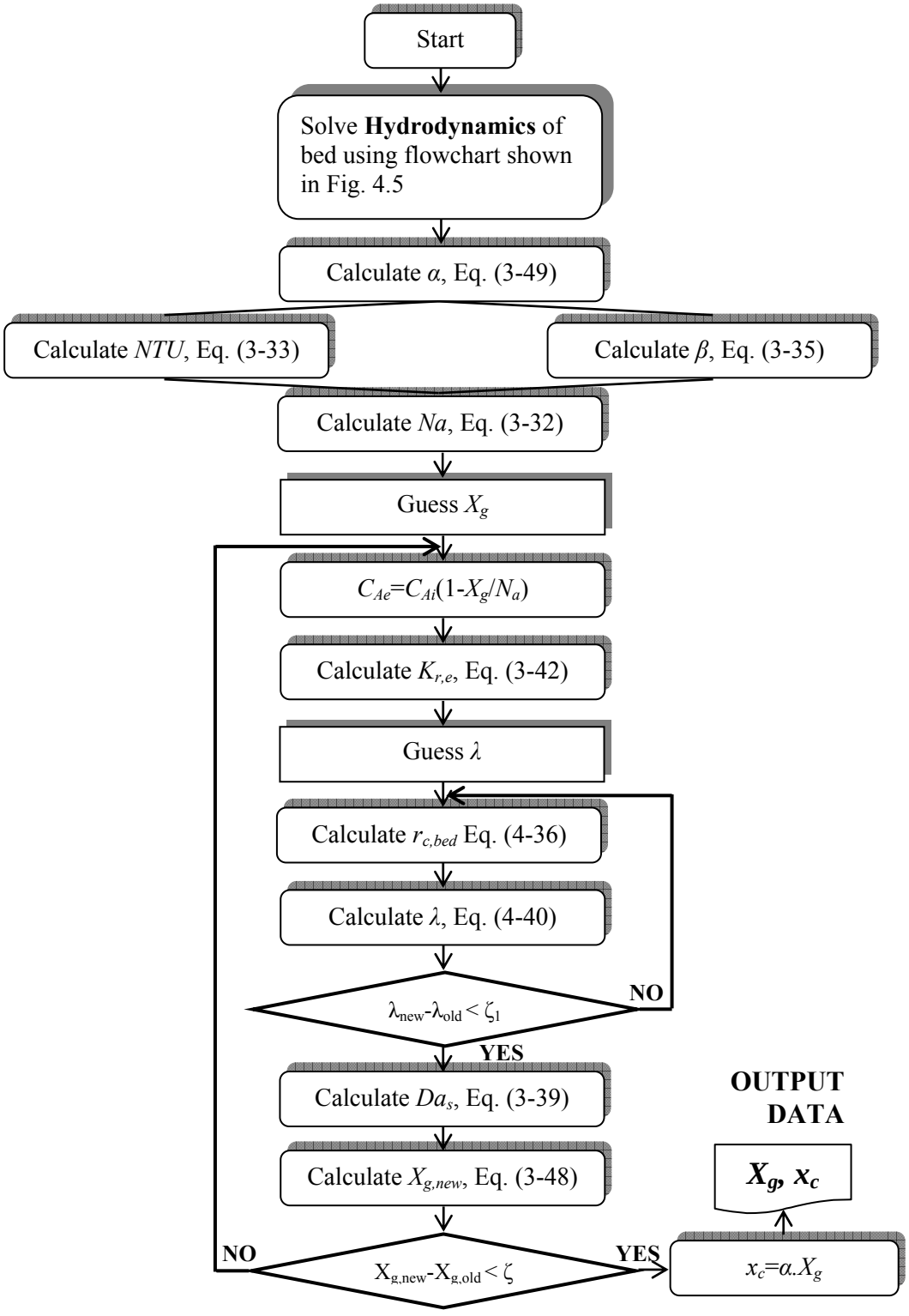

Fig. 4.7: Solution procedure for determining $CuCl_2$ and steam conversions, assuming a *Shrinking Core Model* (*SCM*) for kinetics of the particle consumption.

$$\eta_{bed} = 1 - \frac{\sum_{outlet} Reactant\ moles}{\sum_{inlet} Reactant\ moles} \tag{4-38}$$

For the case of the present work,

$$\sum_{outlet} Reactant\ moles = \left(n_{CuCl_2} + n_{H_2O}\right)_{outlet} \tag{4-39}$$

$$\sum_{inlet} Reactant\ moles = \left(n_{CuCl_2} + n_{H_2O}\right)_{inlet} = 2 + 1 = 3 \tag{4-40}$$

The reactant moles at the outlet may be computed based on their conversions as shown below.

$$\frac{n_{CuCl_2|outlet}}{n_{CuCl_2|inlet}} = \frac{C_{po}}{C_{pi}} = 1 - x_{c,b} \tag{4-41a}$$

$$n_{CuCl_2|outlet} = n_{CuCl_2|inlet}\left(1 - x_{c,b}\right) \tag{4-41b}$$

and

$$\frac{n_{H_2O|outlet}}{n_{H_2O|inlet}} = \frac{C_{Ao}}{C_{Ai}} = 1 - X_g \tag{4-42a}$$

$$n_{H_2O|outlet} = n_{H_2O|inlet}\left(1 - X_g\right) \tag{4-42b}$$

Substituting Eqs (4-41b) and (4-42b) into Eq. (4-39), and then substituting the resulting expression into Eq. (4-38), taking into account Eq. (4-40) and considering $n_{CuCl_2|inlet} = 2$ and $n_{H_2O|inlet} = 1$ yields

$$\eta_{bed} = 1 - \frac{2\left(1 - x_{c,b}\right) + 1 - X_g}{3} \tag{4-43}$$

Simplifying Eq. (4-43) gives

$$\eta_{bed} = \frac{2x_{c,b} + X_g}{3} \tag{4-44}$$

Hence, the bed effectiveness can be determined at a known process condition after calculating the cupric chloride particle and steam conversions within the bed reactor. The influences of various process parameters on the bed effectiveness have been studied and the results will be illustrated in the next chapter.

Chapter 5

Results and Discussion

5.1 INTRODUCTION

The numerical results from the models in previous chapter will be presented in this chapter.The computed outcomes of hydrodynamics of the reactor are given for a typical bench-scale and full-scale bed reactor. The effects of the bed's operating parameters, such as superficial gas velocity and bed inventory, on the bed height, average bubble diameter and bed void fraction are investigated. The hydrodynamic results are required for studying the overall performance of the bed, in terms of the conversions of reactants, i. e. cupric chloride particles and steam.

At the next stage, the reactor behavior is investigated numerically based on the Fluidized Bed Model explained in the previous chapter. The performance of the bed is examined under the assumption of limiting kinetic models, i. e. Volumetric Model and Shrinking Core Model. The prediction of the conversion of reactants is illustrated for

various process parameters, using the previously proposed solution algorithms. Finally, the predictions of both models are compared and discussed.

5.2 RESULTS OF BED HYDRODYNAMICS

The influence of the superficial gas velocity and bed inventory on the bed height, bed void fraction and average bubble diameter are studied for two bed scales: lab (bench) scale bed, and a full-scale bed.

5.2.1 Bench-Scale Reactor

Consider a column that is *16.5-cm* high and a diameter of *2.66-cm*. Figure 5.1 shows the variation of the bed height versus superficial velocity at three different values of bed inventory. Increasing the superficial velocity leads to a taller bed height, since the upward force of the gas stream acting on suspended particles increases. As expected, the bed height is higher at larger bed inventories.

The predicted average bubble diameter versus the superficial velocity is shown in Fig. 5.2. At a low flow rate of steam, the initial bubbles above the distributor are not big enough to contact each other. In contrast, when the gas flow rate is high, the initial bubbles are big enough, so they overlap when formed. As observed in Fig. 5.2, a higher velocity (steam flow rate) results in larger bubbles. On the other hand, Fig. 5.2 indicates that the bubble average diameter is larger at a heavier bed inventory. This may be due to a taller bed height at a larger bed inventory, so that neighboring bubbles have more opportunity to contact and form larger bubbles, which on average would lead to a larger bubble diameter at a heavier inventory.

Furthermore, Fig. 5.3 shows that a higher superficial velocity may cause a larger bed void fraction. This occurs since a high flow rate of gas for a specific bed geometry would occupy more volume of the bed, thereby leading to a higher void fraction of the bed. However, at a certain gas velocity, the bed void fraction can be reduced by increasing the bed inventory, but this would require more space.

The effects of particle diameter on bed properties are also investigated. The outcomes are depicted in Figs. 5.4-5.6, in terms of the bed height, average bubble diameter and bed voidage at varying particle diameters. Each of these parameters

decreases when the mean particle diameter is bigger. This reduction for larger particles is interestingly sharper. A higher bed height for smaller particles occurs, since with the same amount of bed inventory, smaller particles lead to a larger the gap-space between adjacent particles, which may cause a taller bed height. Furthermore, bubble forming with larger particles is not as easy, compared to when particles are smaller. Hence, on an average basis, the bubble diameter would be smaller at larger particle diameters. On the other hand, when particles are larger, the fluidizing gas does not have more gap-space to penetrate through the solid particles, thereby causing a decrease in bed voidage.

Figure 5.7 illustrates the influence of particle sphericity on the bed height at three different bed inventories. As the particle shape becomes more spherical, the height of the bed decreases. When the particles have an irregular shape, there will be more free space between adjacent particles, compared to the situation when the particles are closer to a spherical shape. Hence, when the particle sphericity is less, the bed height at a given bed inventory would be taller.

Lastly, the pressure drop in the stream of steam flowing through the cupric chloride particles in the bed is further calculated for a sphericity of 0.85 at gas velocities greater than the minimum fluidization velocity. The results are represented in Fig. 5.8. As shown in this figure, the pressure drop is represented as a function of bed inventory, since it is the only crucial parameter that yields resistance against the flow of fluidizing steam (see Eqs. (2-7) and (2-10)). It can be observed that a heavier inventory would cause more resistance against the path of gas flow and the gas stream would experience more pressure drop. But at a fix bed condition where the gas velocity is less than the minimum fluidization velocity (Table 2.2), the pressure drop would also vary with gas velocity, since particle weights are not yet balanced with upside gas drag forces.

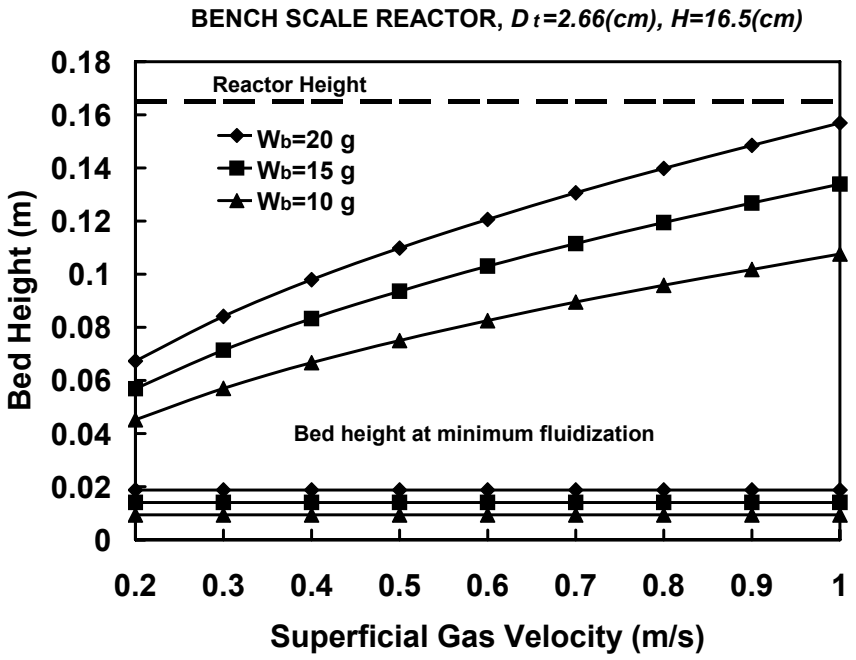

Fig. 5.1: Effects of superficial gas velocity on bed height, at three different inventories (bench-scale bed).

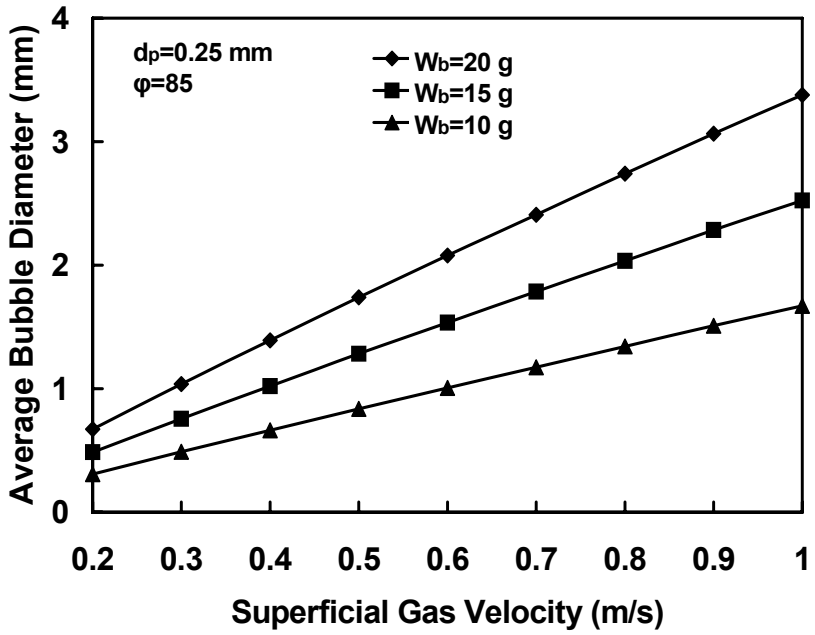

Fig. 5.2: Effects of superficial gas (steam) velocity on average bubble diameter at three different inventories (bench-scale bed).

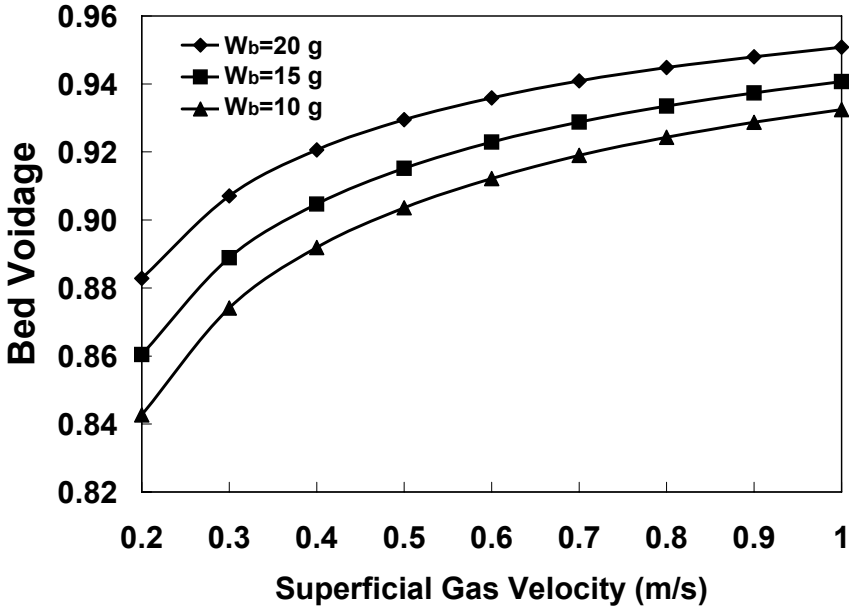

Fig. 5.3: Effects of superficial gas velocity on bed voidage, at three different inventories (bench-scale bed) with .φ=0.85.

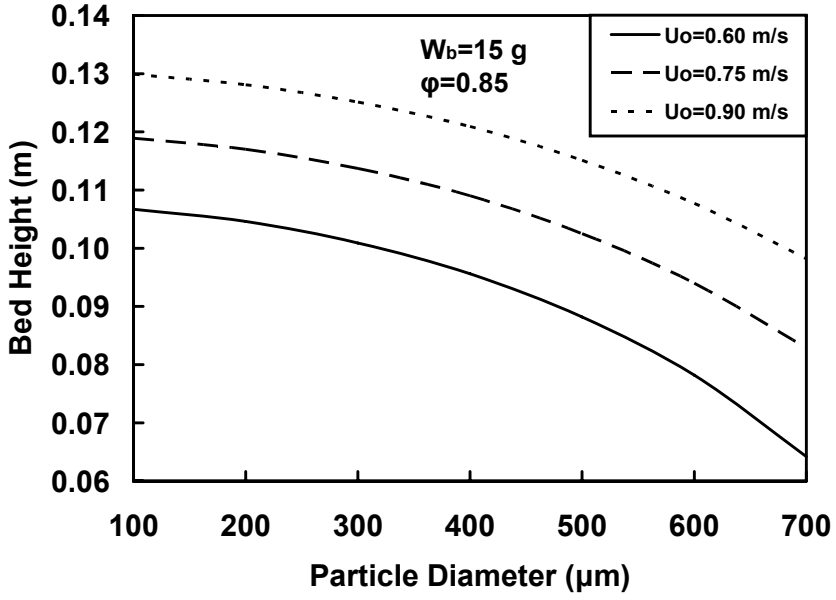

Fig 5.4: Dependence of bed height on particle diameter (bench-scale bed).

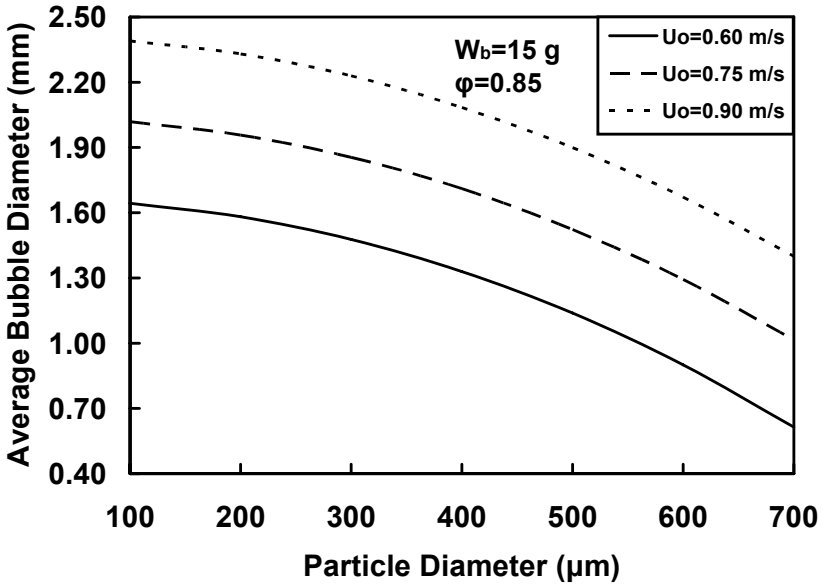

Fig 5.5: Effects of particle diameter on average bubble diameter (bench-scale bed).

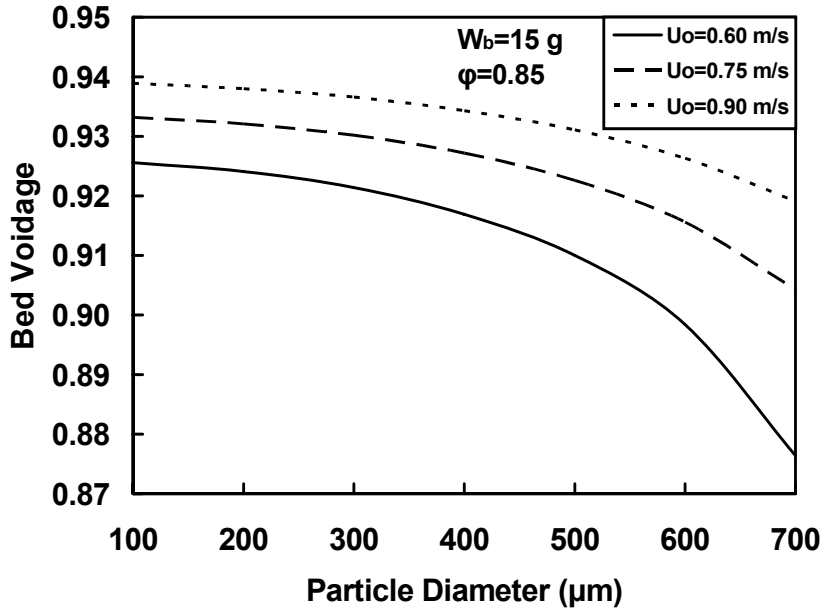

Fig 5.6: Effects of particle diameter on bed voidage (bench-scale bed).

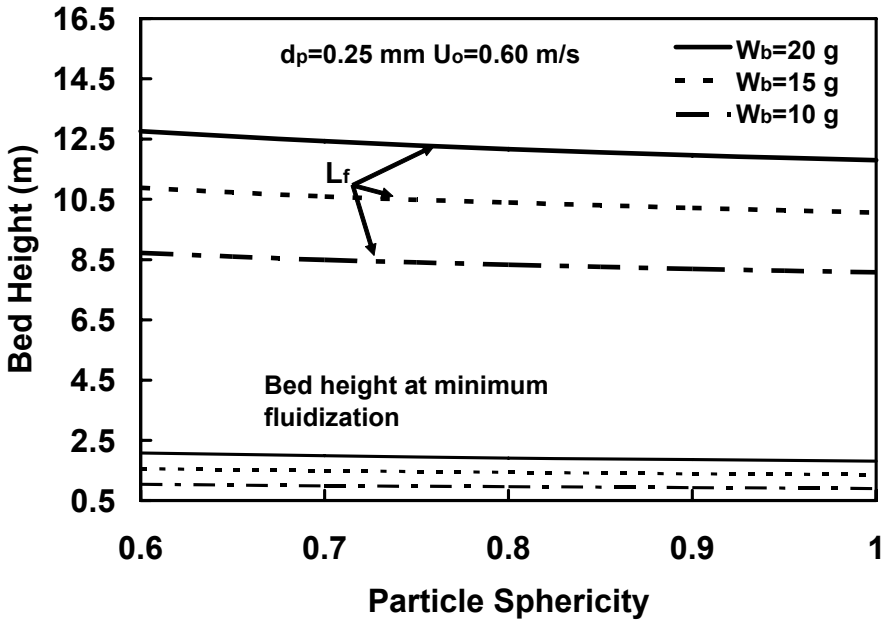

Fig. 5.7: Effects of particle sphericity on bed height (bench-scale bed).

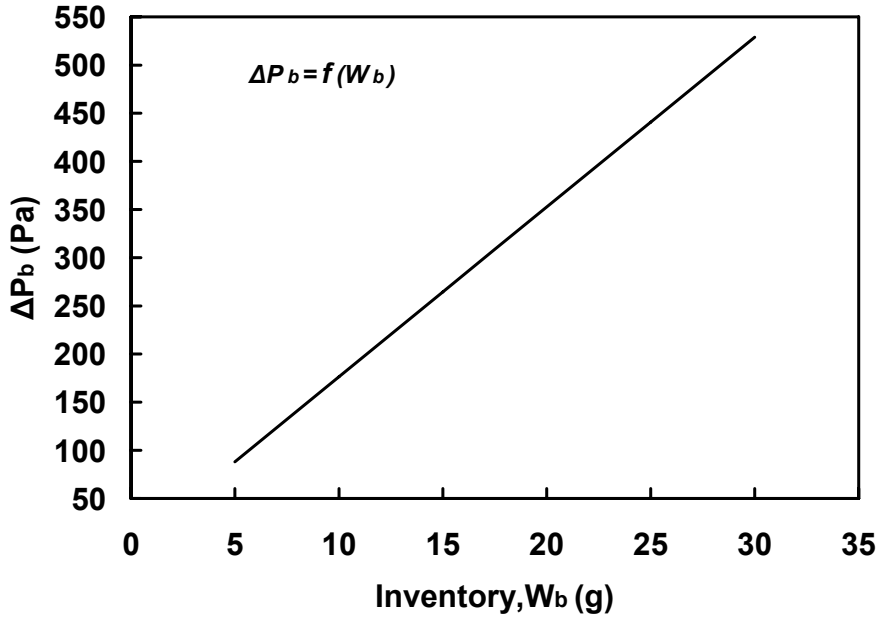

Fig. 5.8: Pressure drop along the bed, versus bed inventory at $U_o > U_{mf}$ (bench-scale bed), φ=0.85.

5.2.2 Full-Scale Reactor

In order to investigate the feasibility of the hydrodynamic analysis, it is important to consider the hydrodynamic behavior of a commercial unit. Considering a scaling factor, m=24 (as an example), compared to the lab-scale reactor of section 5.1.2, the height and diameter of the reactor are assigned, respectively, as *4m* and *0.6448m*. Likewise, the effects of gas velocity, bed inventory and particle sphericity on the bed height, average bubble diameter and bed porosity are studied. The results are depicted in Figs. 5.9-5.12. The predicted results for a full-scale reactor in Figs. 5.9-5.11 are qualitatively the same as the graphs of Figs. 5.1-5.3, respectively. Similarly, increasing the superficial gas velocity causes an increase in bed height, average bubble diameter and bed void fraction. Also, a heavier bed inventory may result in a taller bed height and larger bubble diameter, whereas it can lead to a smaller bed void fraction. From Fig. 5.10, it seems that the computed bubble diameters are too large for a full-scale bed. This issue needs to be investigated further in future research, when performing lab-scale experiments. Scaling is a key issue for bubble columns and fluidized beds. Scaling laws are beyond the scope of this thesis, but they are discussed in chapter 6 as part of recommended future research.

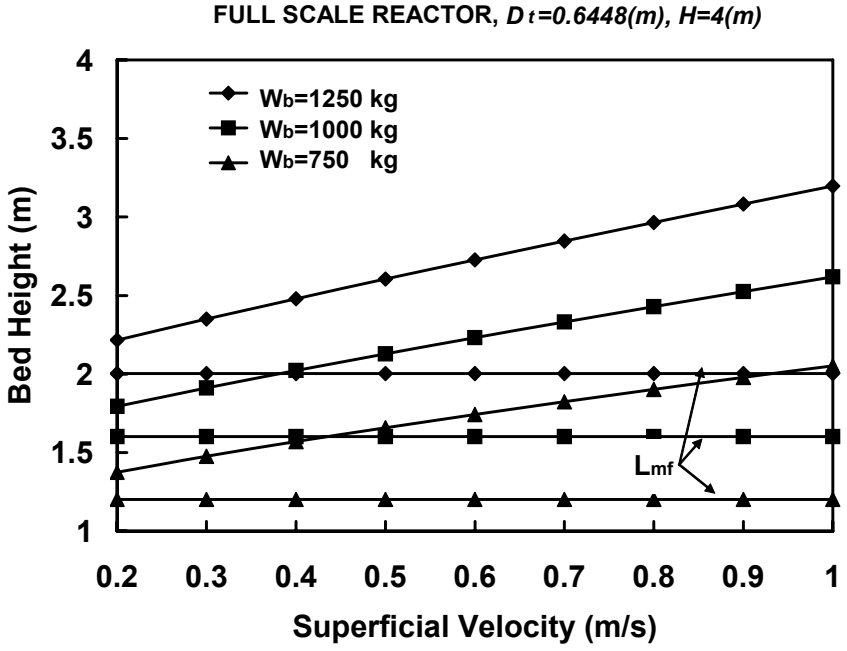

Fig. 5.9: Effects of superficial velocity on bed height, at three different inventories (full-scale bed).

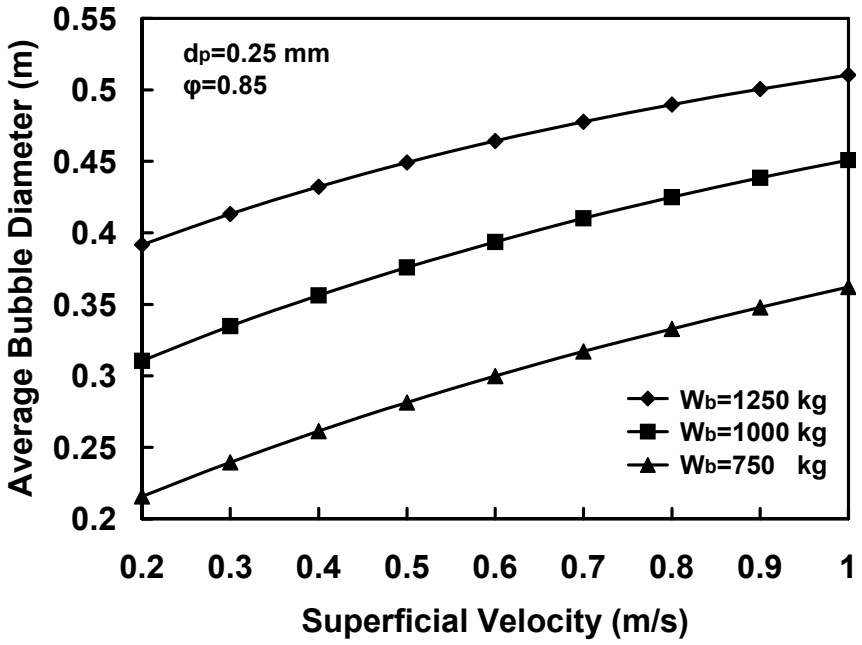

Fig. 5.10: Influence of superficial gas (steam) velocity on the average bubble diameter at three different inventories (full-scale bed).

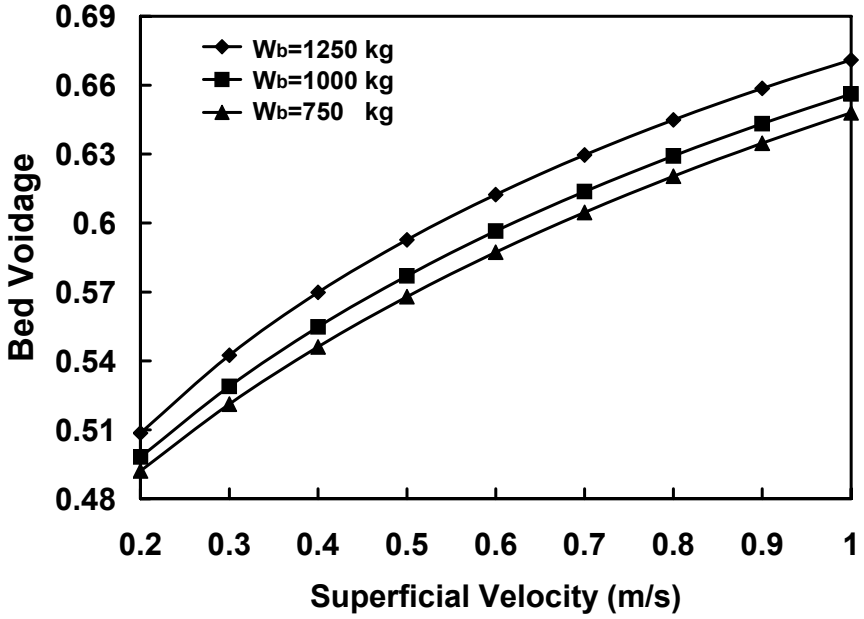

Fig. 5.11: Effects of superficial velocity on bed voidage, at three different inventories (full-scale bed).

Additionally, Fig. 5.12 illustrates the variation of bed height versus particle sphericity in a full-scale bed, at three different values of inventory. On an average basis, when the sphericity increases from 0.6 to 1.0, the bed height decreases by 12.05% and the bed height at a minimum fluidization reduces by 13.16%. These values for lab-scale results (Fig. 5.7) are 10.8% and 13.15%, respectively, for the bed height and minimum fluidization bed height.

Figure 5.13 shows the pressure drop across the bed, for the range of 500-1500 kg of inventory. In a commercial reactor, the pressure drop throughout the bed is an important issue compared to the lab scale-bed (Fig. 5.8).

Moreover, the influences of particle diameter on the bed height, average bubble diameter and bed voidage are numerically investigated for a full-scale bed. The results are illustrated in Figs. 5.14-5.16, respectively. Comparing them with graphs depicted earlier in Figs. 5.4-5.6 for a bench-scale bed, it can be seen that curves in Figs. 5.14-5.16 are qualitatively the same. Larger particles result in a shorter bed height, smaller average bubble diameter and smaller bed voidage.

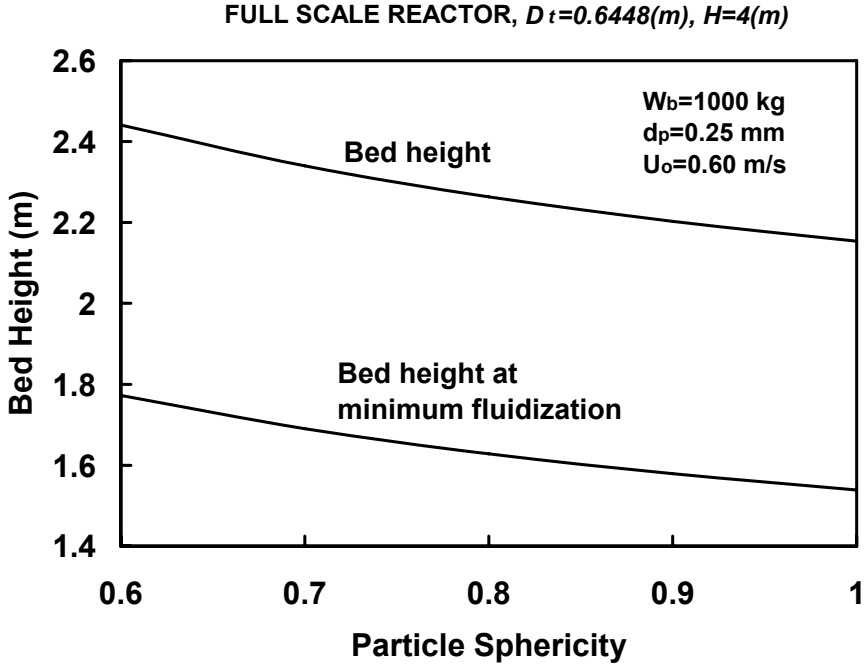

Fig. 5.12: Effects of particle sphericity on bed height (full-scale bed).

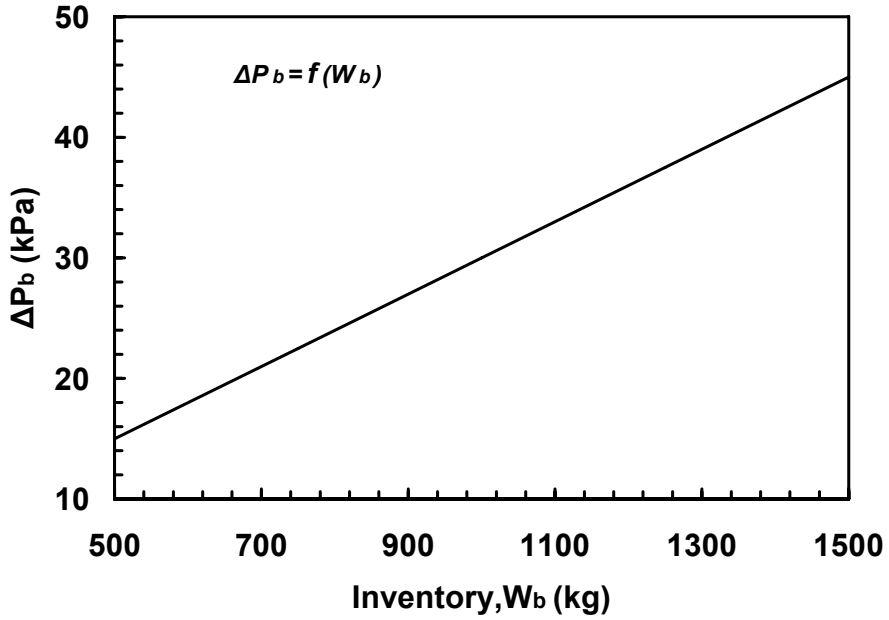

Fig. 5.13: Pressure drop along the bed versus bed inventory (bench-scale bed).

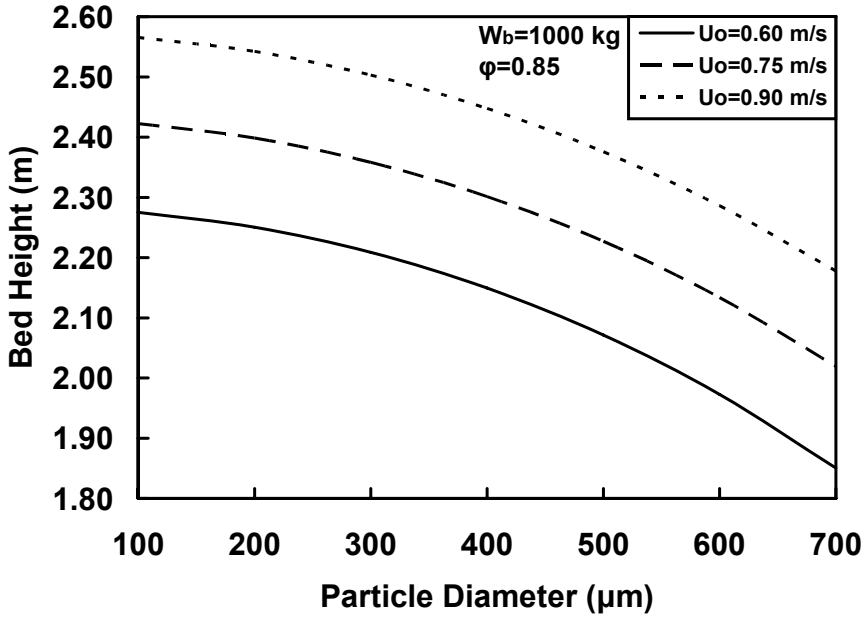

Fig 5.14: Effects of particle diameter on bed height (full-scale bed).

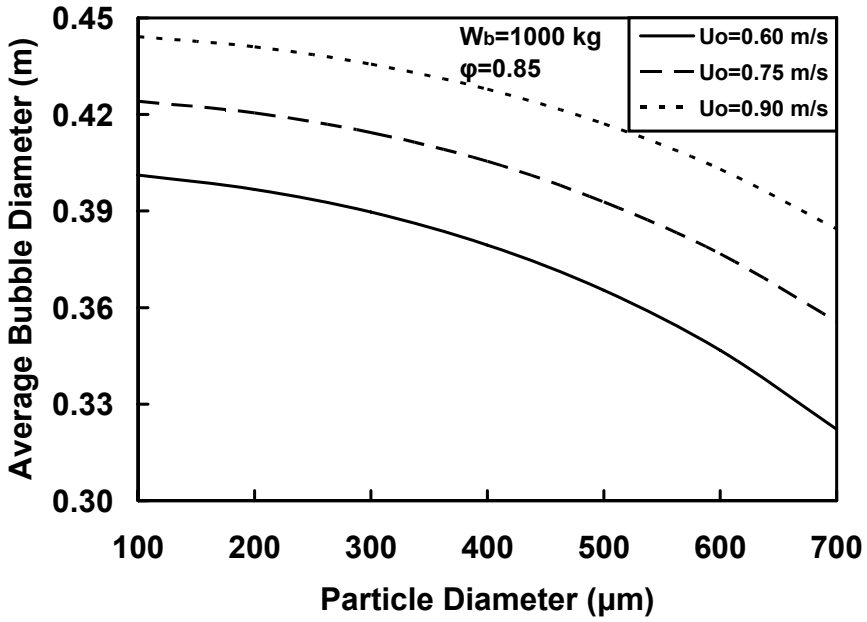

Fig 5.15: Effects of particle diameter on average bubble diameter (bench-scale bed).

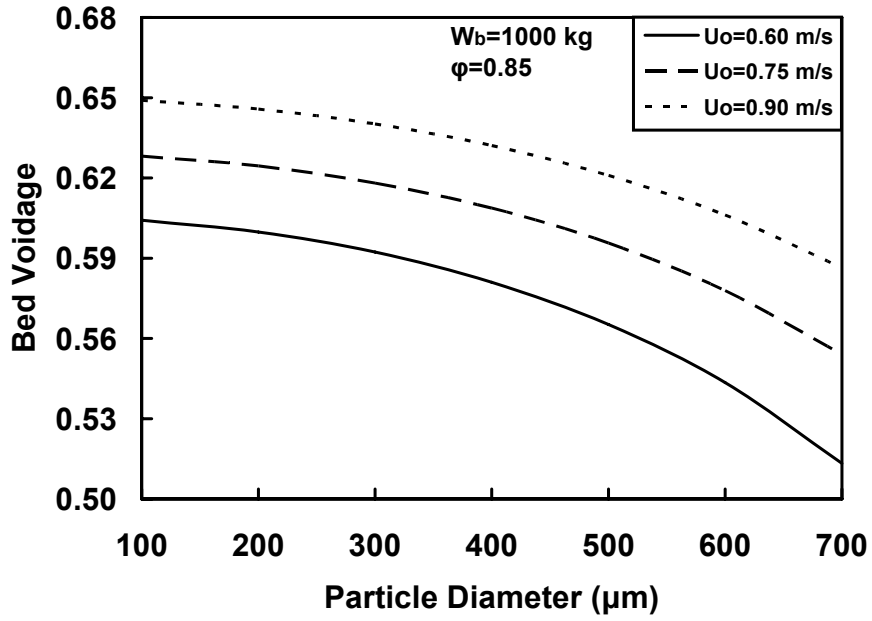

Fig 5.16: Effects of particle diameter on bed voidage (bench-scale bed).

5.3 RESULTS FOR BED PERFORMANCE

Since the reaction kinetics of $CuCl_2$ particles in the reaction with superheated steam is unknown, two limiting kinetics (VM and SCM) will be considered and the results in terms of conversions of reactants, overall rate of reaction, inter-phase effectiveness factor and bed effectiveness will be illustrated in this section at various process parameters. The outcomes are separately given for VM and SCM cases using solution algorithms presented in the previous chapter, and then the predictions of these two limiting kinetics models will be compared and discussed.

5.3.1 Bed Performance Based on Volumetric Model

The predicted steam and $CuCl_2$ particle conversions at various superficial velocities and three typical bed inventories are shown in Fig. 5.17. The solid conversion increases with the fluidizing gas velocity, since the solid particles have more contact with steam. On the other hand, however, the steam conversion decreases as its superficial velocity increases. For a certain amount of bed inventory, a higher superficial velocity (and consequently gas flow rate) means the less contact of gaseous spices with particles. Furthermore, from Fig. 5.17, a higher bed inventory would improve the conversion of both reactants. At given feed rates of reactants, the mean residence time, $\bar{t}$, increases as the bed inventory rises. Thus, the contact opportunity for both reactants will increase.

The overall rate of reaction in the bed is indicated versus superficial velocity and bed inventory in Fig. 5.18. As mentioned previously, as the gas velocity increases, and the inventory becomes heavier, the solid particle contact with fluidizing gas increases, so the reaction rate (consumption) of particles increases. The profiles in Fig. 5.18 show another presentation of solid conversion, shown in Fig. 5.17.

Figure 5.19 shows the variation of the inter-phase effectiveness factor with superficial velocity and bed inventory. Higher conversion of steam corresponds to the situation where the concentration of steam at the outlet stream, as well as its concentration in the emulsion, are accordingly lower. Thus, the inter-phase effectiveness factor is lower at the higher gas conversion, which may result from higher bed inventory and/or less superficial velocity, as discussed above for the illustrative example shown in Fig. 5.17.

Further results involve the influences of various process parameters on *Bed Effectiveness*, introduced in Chapter 3 and represented by η_{bed}. It may vary between 0 (no reactant conversions) and 1 (complete conversions of both reactants). Conversion of solid particles and steam is illustrated by this new parameter, indicating the net performance of the fluidized bed reactor.

Figure 5.20 shows the variation of η_{bed} versus superficial velocity at three bed inventories. From this figure, η_{bed} may increase or decrease with gas velocity depending upon the bed inventory. This phenomenon is further investigated and the results are depicted in Fig. 5.21 where the bed effectiveness changes with bed inventory at a varying gas velocity. The graphs in Fig. 5.21 may be divided into three regions. At a bed inventory between 12 g and 14 g, the bed effectiveness is independent of the superficial velocity. As the bed inventory exceeds 14 g, a higher velocity leads to larger bed effectiveness. Furthermore, for a bed inventory of less than 12 g, a higher superficial velocity may result in less bed effectiveness.

The influence of bed temperature as a key factor on η_{bed} is illustrated in Fig. 5.22 at varying superficial velocities. This figure suggests that a lower bed temperature improves that performance of the process.

5.3.2 Bed Performance Based on Shrinking Core Model

Similar results are obtained based on Shrinking Core Model. They are depicted in Figs. 5.23 to 5.28, in terms of the conversion of reactants and overall rate of reaction, respectively. The only difference is seen in Fig. 5.27, which shows the effect of bed inventory on η_{bed} at various gas velocities. Unlike Fig. 5.21, there exists only two regions in Fig. 6.27. At a bed inventory lighter than 12 g, superficial velocity does not have a significant effect on η_{bed}. On the other hand, as the inventory exceeds 12 g, a higher velocity results in a higher bed effectiveness.

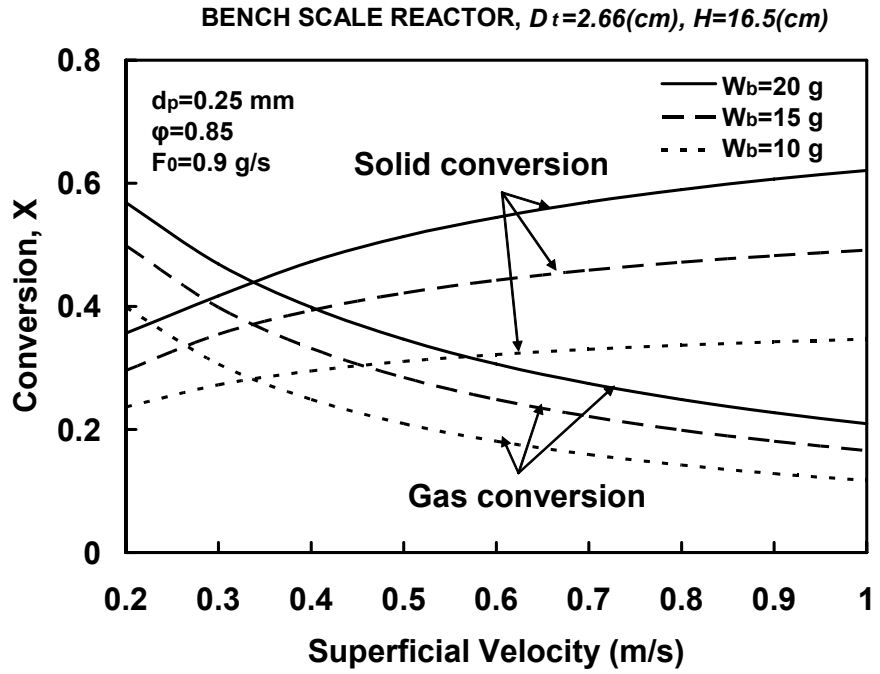

Fig. 5.17: Conversion of cupric particles and steam within a bench-scale reactor for a typical range of superficial gas velocities and three different values for bed inventory (*Volumetric Model*).

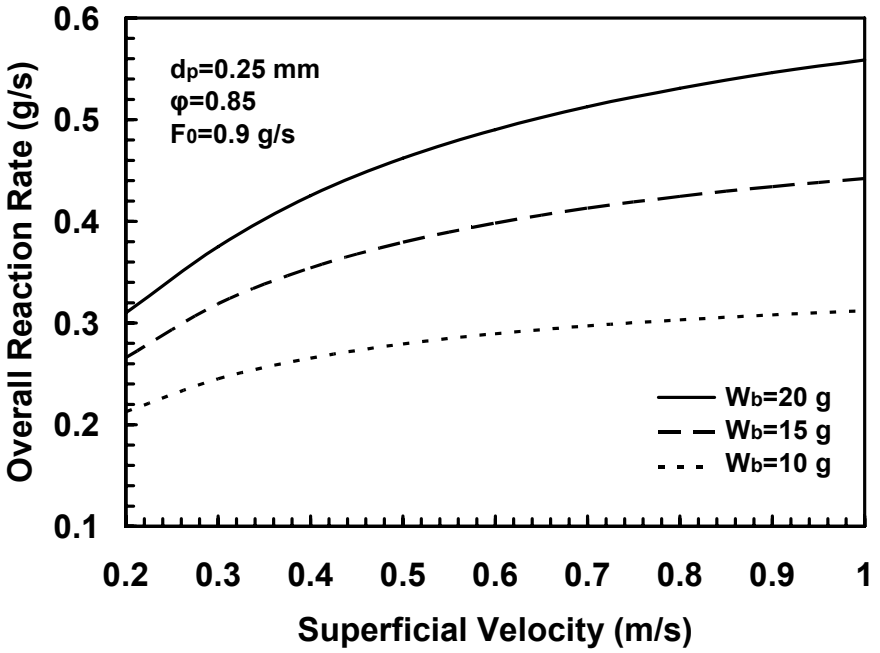

Fig. 5.18: Overall reaction rate at various superficial velocities and typical bed inventories within a bench-scale reactor (*Volumetric Model*).

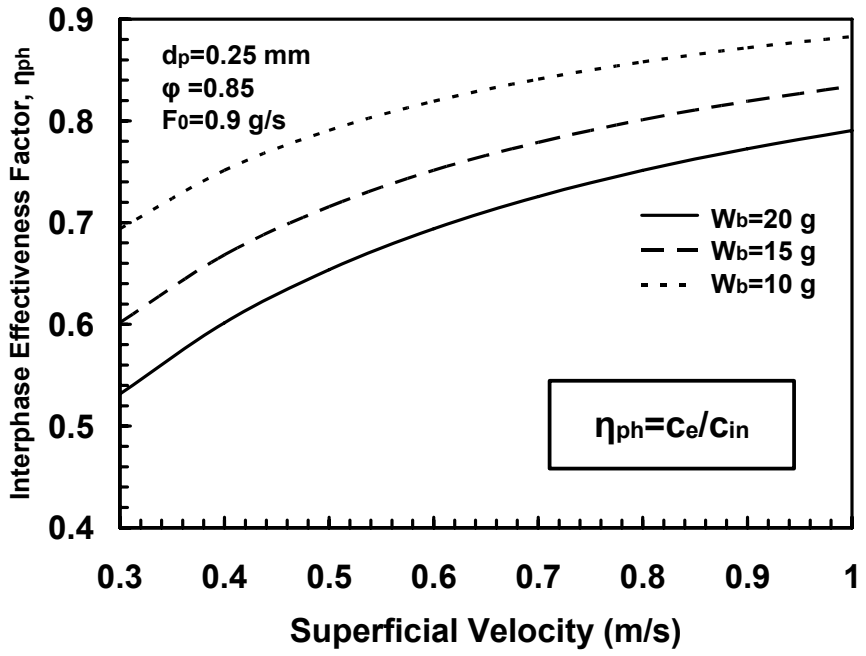

Fig. 5.19: Variation of inter-phase effectiveness factor, η_{ph} with superficial velocity at three bed inventories within a bench-scale reactor (*Volumetric Model*).

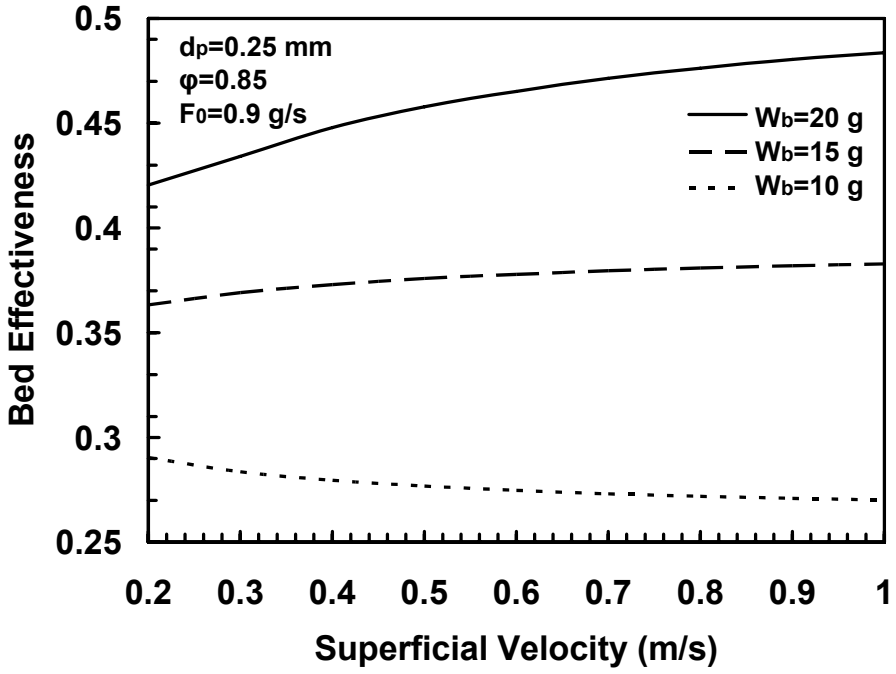

Fig. 5.20: Predicted bed effectiveness at various superficial velocities according to the *Volumetric Model.*

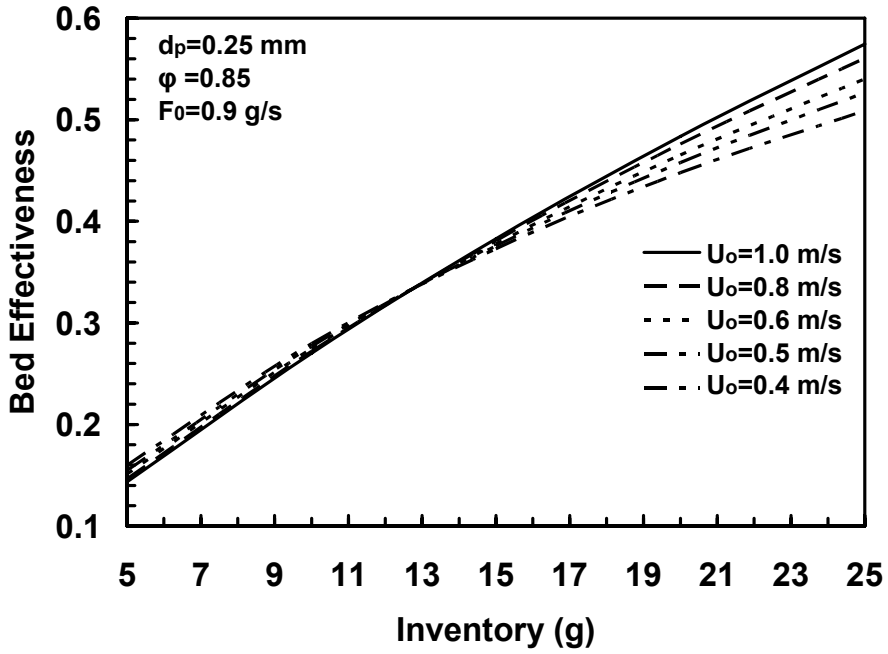

Fig. 5.21: Dependence of bed effectiveness on bed inventory according to the *Volumetric Model.*

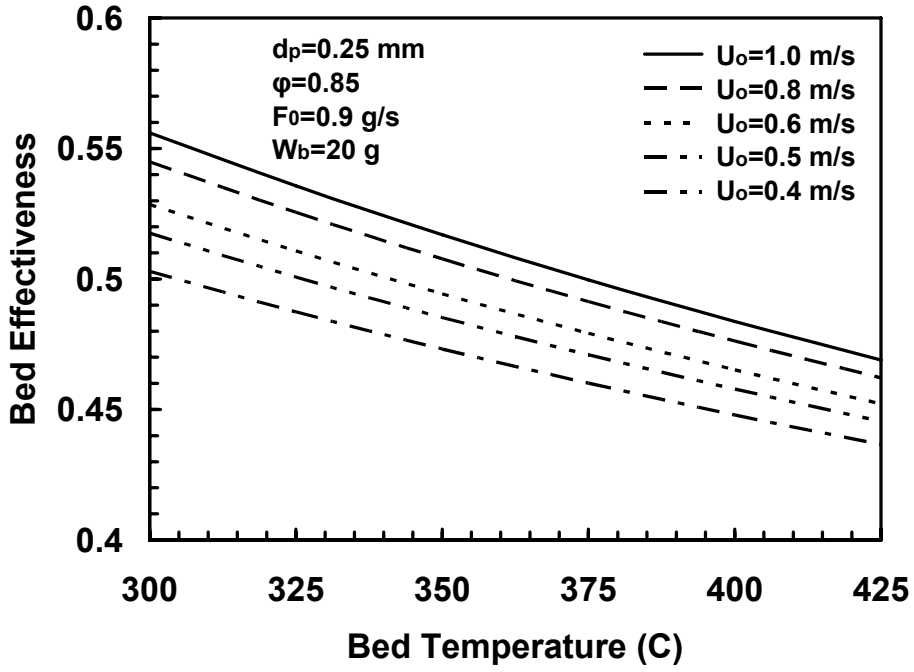

Fig. 5.22: Dependence of bed effectiveness on bed temperature at different superficial velocities based on the *Volumetric Model.*

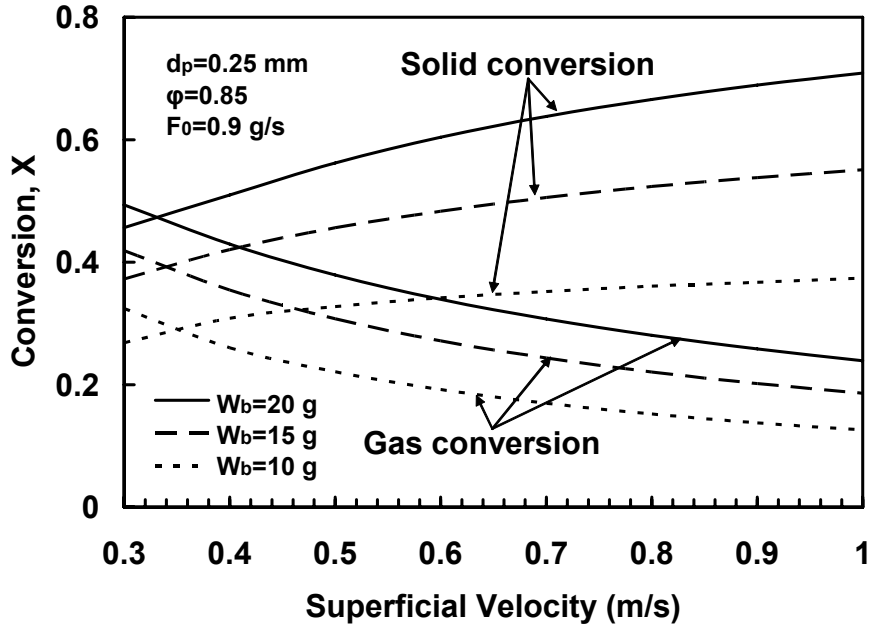

Fig. 5.23: Conversion of cupric particles and steam within a bench-scale reactor for a typical range of superficial gas velocities and three different values for bed inventory (*Shrinking Core Model*).

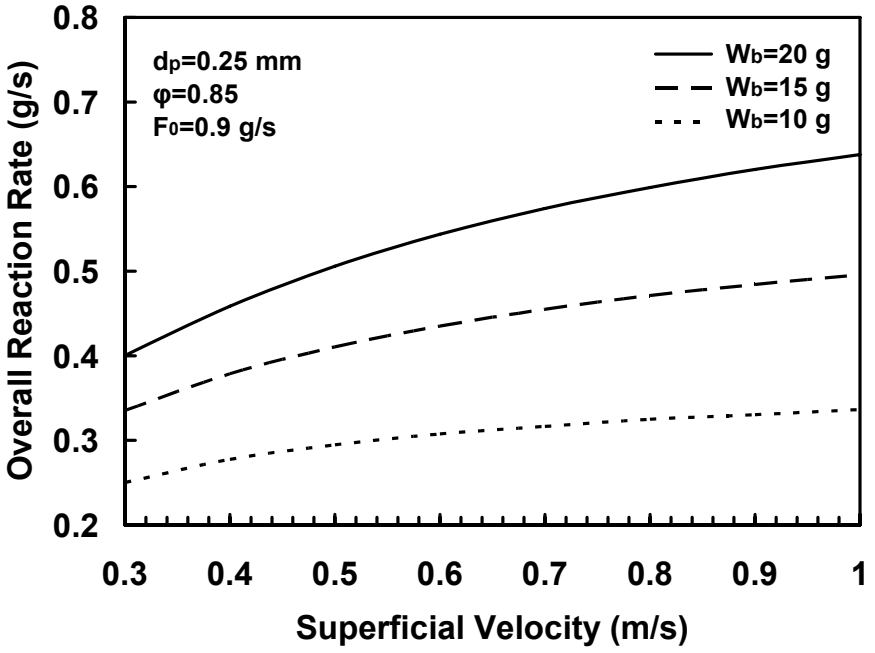

Fig. 5.24: Overall reaction rate at various superficial velocities and typical bed inventories within a bench-scale reactor (*Shrinking Core Model*).

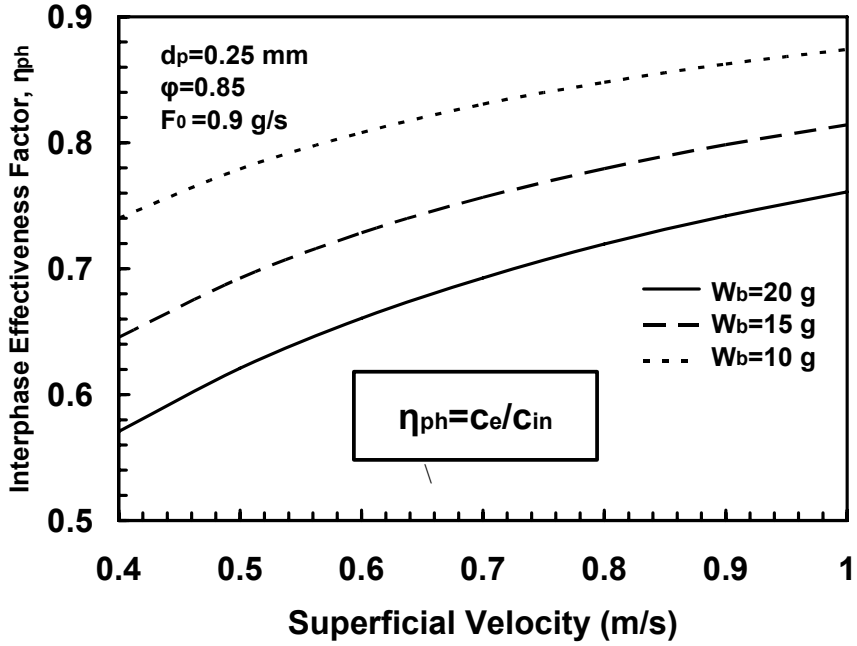

Fig. 5.25: Variation of inter-phase effectiveness factor, η_{ph}, with superficial velocity at three bed inventories within a bench-scale reactor (*Shrinking Core Model*).

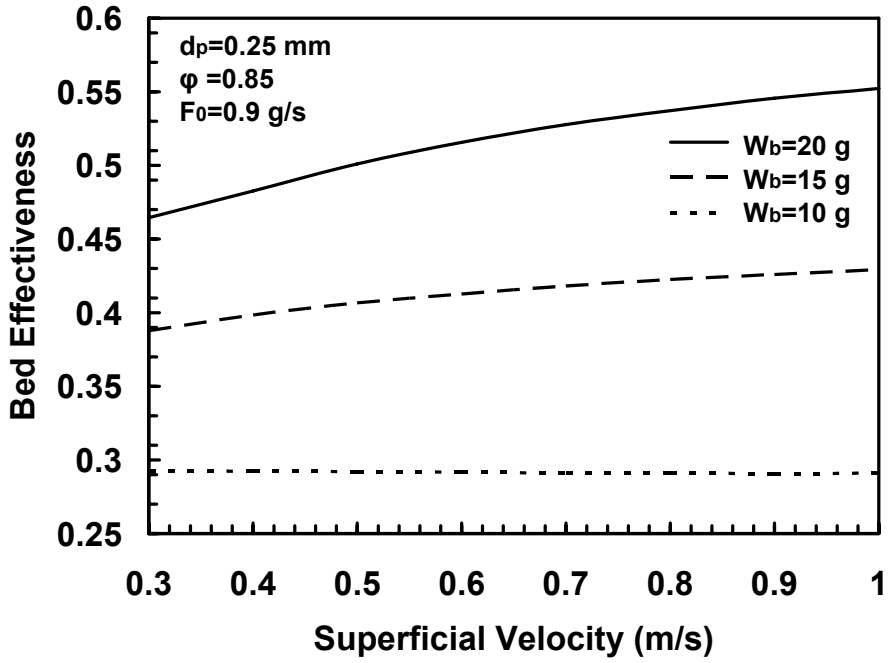

Fig. 5.26: Predicted bed effectiveness at various superficial velocities according to the *Shrinking Core Model.*

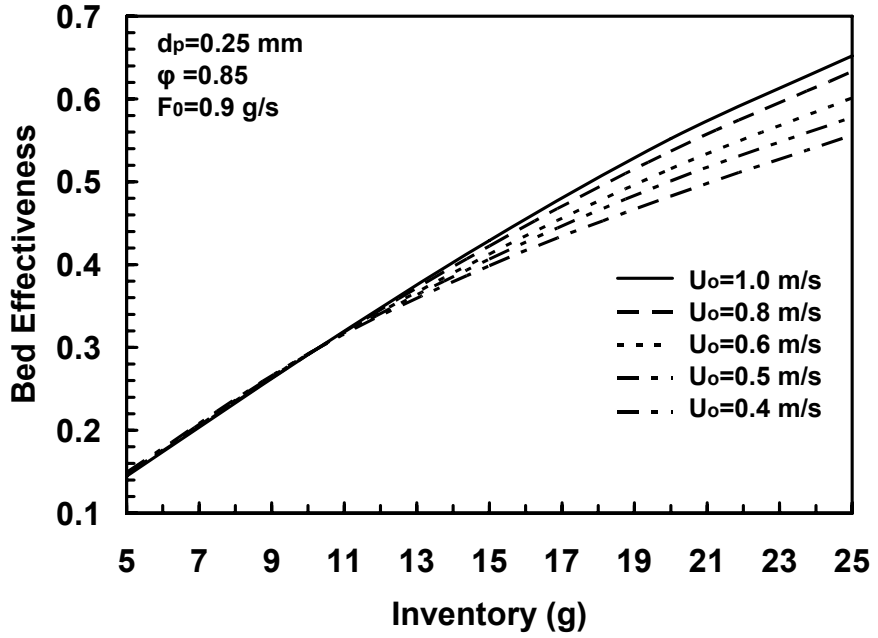

Fig. 5.27: Dependence of bed effectiveness on bed inventory according to the *Shrinking Core Model.*

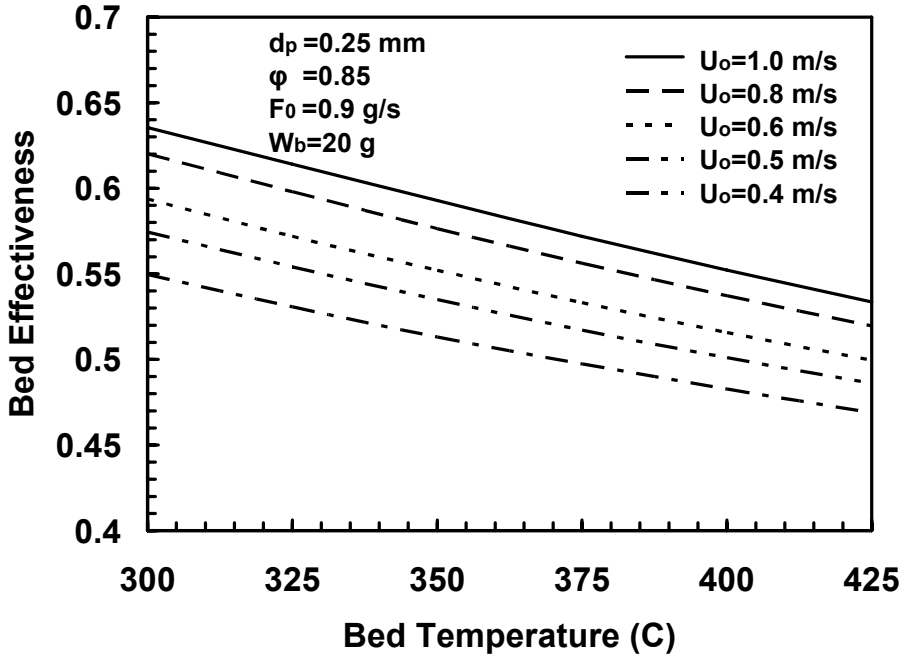

Fig. 5.28: Dependence of bed effectiveness on bed temperature at different superficial velocities based on the *Volumetric Model.*

5.3.3 Comparison of SCM and VM Results

The predictions of two kinetic models are compared herein. The computed reactant conversions, overall rate of reaction and inter-phase effectiveness factor based on VM and SCM are shown in Figs. 5.29 to 5.31, respectively, under identical process conditions. Figure 5.29 indicates that if the kinetics of solids follows the SCM, the conversion of both $CuCl_2$ particles and fluidizing steam would be higher than the prediction by VM. Also, SCM predicts a higher overall rate of conversion than VM (Fig. 5.30). Further comparisons of kinetic models are made in Fig. 5.31 in terms of the inter-phase effectiveness factor, η_{ph}, defined in Eq. (3.30). From Fig. 6.31, the SCM prediction of η_{ph} is less than VM. The reason is shown in Fig. 5.29, where conversion of gaseous reactant is higher based on the SCM compared to VM. Thus, the mean concentration of steam in the emulsion would be less for the case of SCM. Therefore, η_{ph} based on the SCM is lower than that of VM.

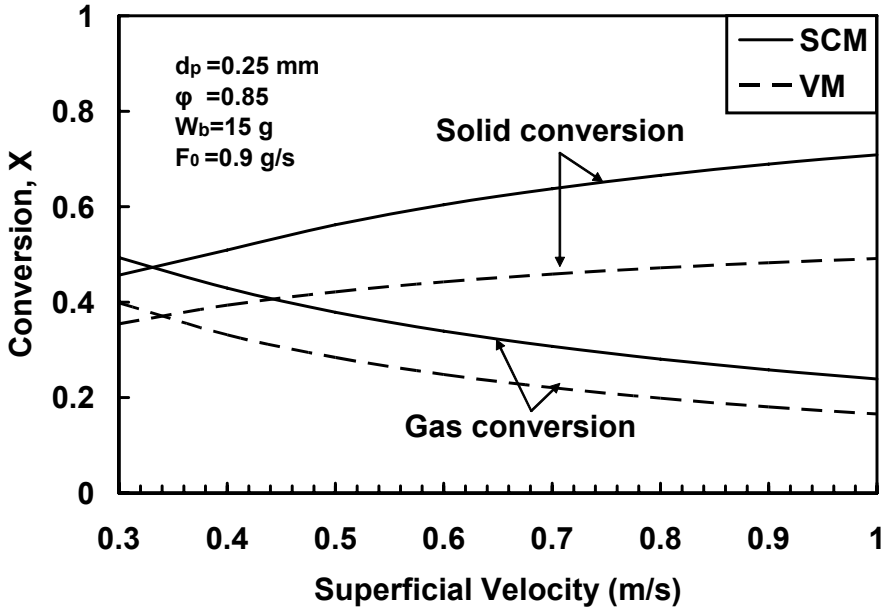

Fig. 5.29: Comparison of prediction of SCM and VM in terms of reactants conversions (bench-scale bed).

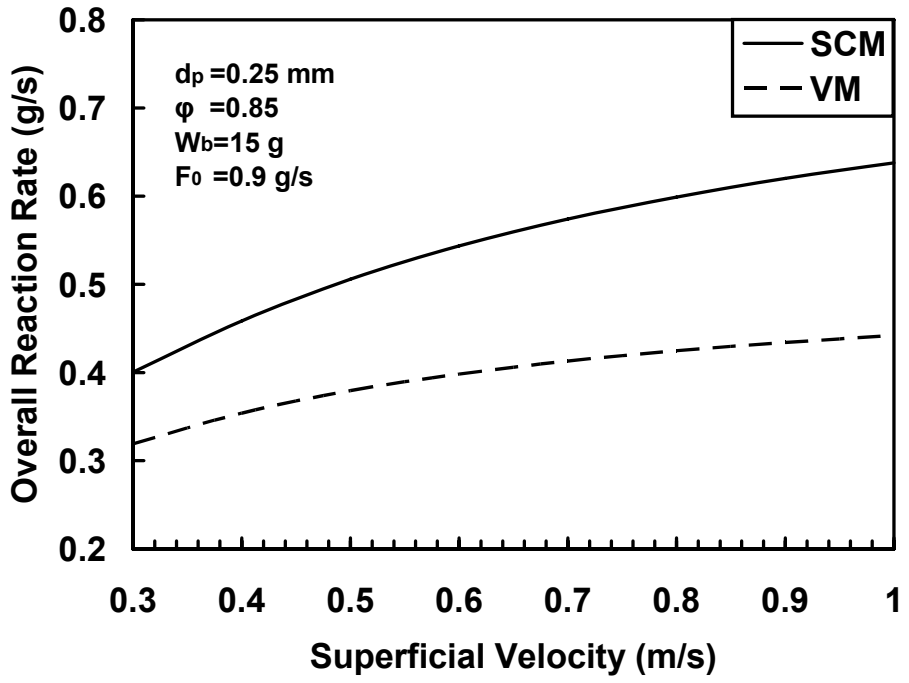

Fig. 5.30: Comparison of predictions of SCM and VM in terms of the overall reaction rate (bench-scale bed).

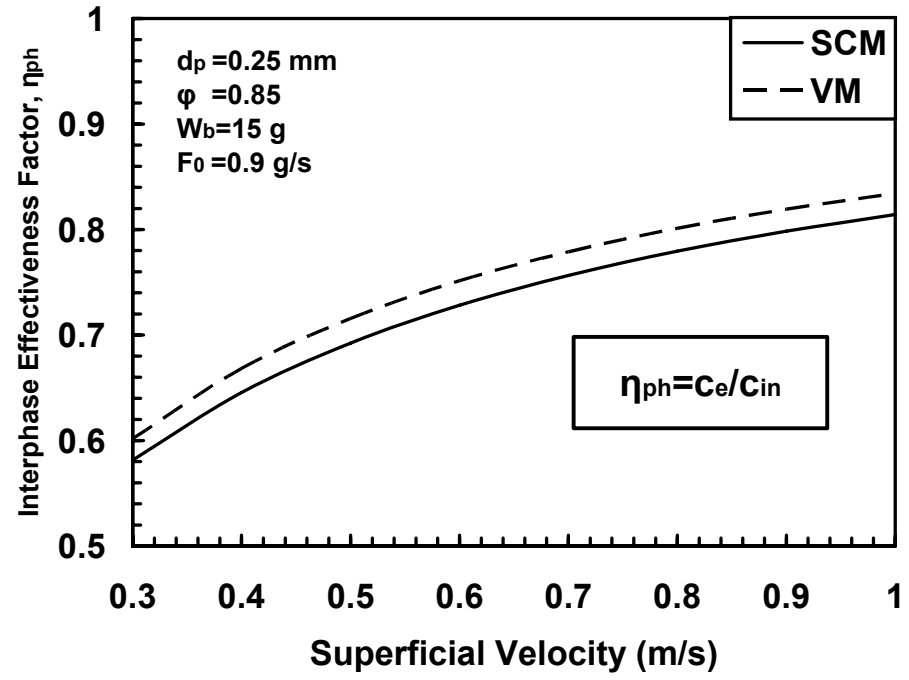

Fig. 5.31: Comparison of predictions of SCM and VM in terms of inter-phase effectiveness factor (bench-scale bed).

The bed temperature affects the reaction kinetics, gaseous reactant concentration and thermophysical properties, as well as conversions of $CuCl_2$ particles and conversion of steam as represented in Fig. 5.32, based on both SCM and VM for a certain process condition. An interesting result from this figure is that the reaction temperature may affect solid particle conversion, while it has no significant effect of conversion of the fluidizing gas. Figure 5.32 suggests that lowering the reaction temperature would improve the conversion of cupric chloride particles.

Finally, the bed effectiveness profiles predicted by SCM and VM are compared at a varying superficial velocity, bed inventory and bed temperature in Figs. 5.33 to 5.35, respectively. In these figures, the profiles of SCM are higher than those of VM. In Fig. 5.33, at higher gas velocities (almost greater than 0.6 m/s), the bed effectiveness based on VM is approximately independent of velocity, whereas SCM still grows at higher velocities. Moreover, from Fig. 5.34, at a lighter bed inventory (less than 10 g), the prediction of both models is almost the same. As discussed in Figs. 5.22 and 5.28, a lower bed temperature may improve the bed effectiveness, due to the conversion of solid particles (Fig. 5.32). An illustrative example of SCM and VM predictions of η_{bed} versus temperature is depicted in Fig. 5.35

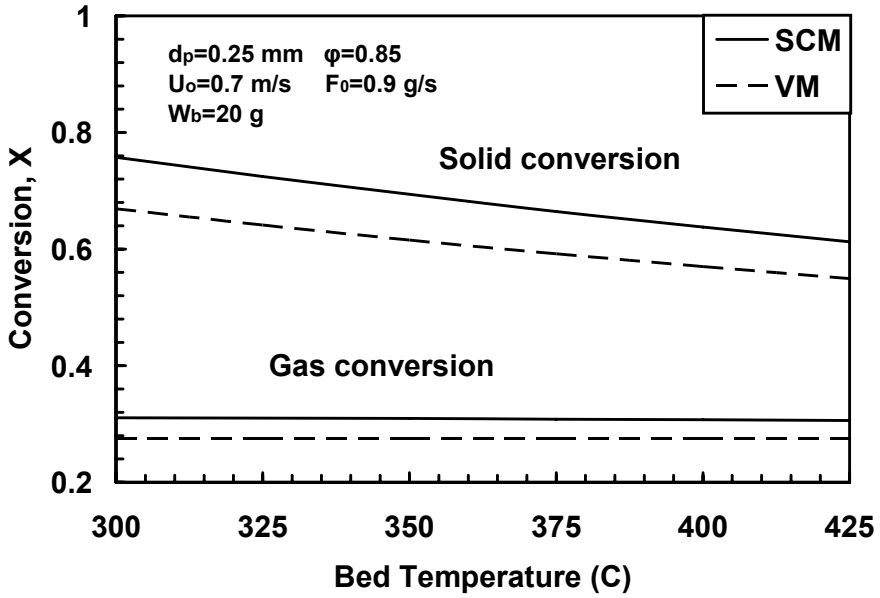

Fig. 5.32: Effects of bed temperature on conversion of cupric chloride particles and steam within a bench-scale bed, based on SCM and VM.

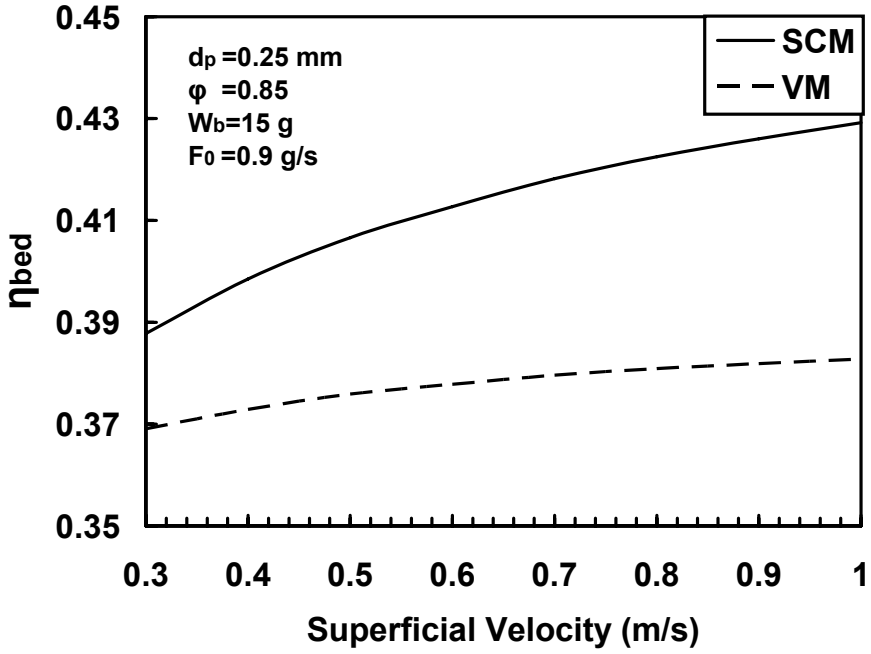

Fig. 5.33: Comparison of SCM and VM predictions, in terms of bed effectiveness versus superficial velocity, within a bench-scale bed.

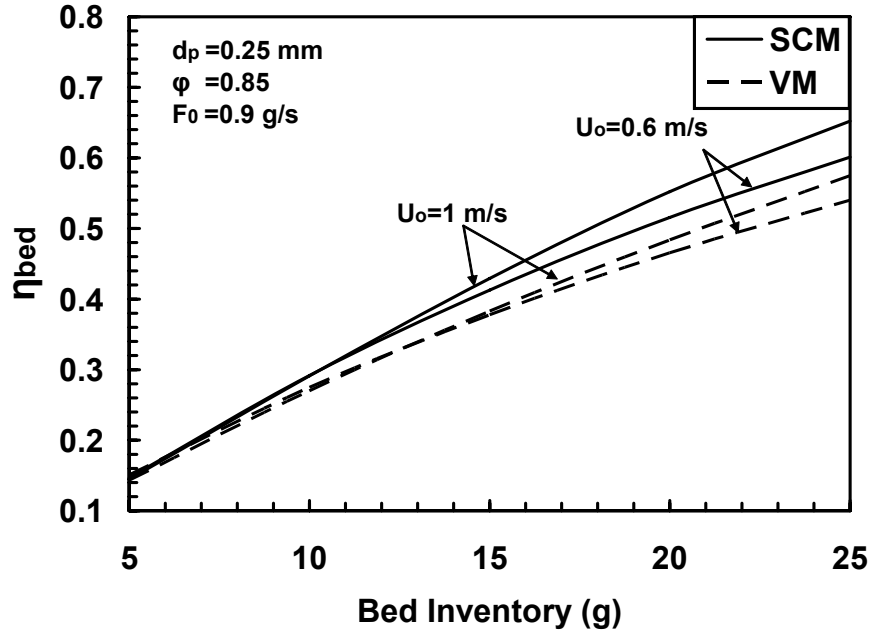

Fig. 5.34: Comparison of SCM and VM predictions, in terms of bed effectiveness versus inventory, within a bench-scale bed.

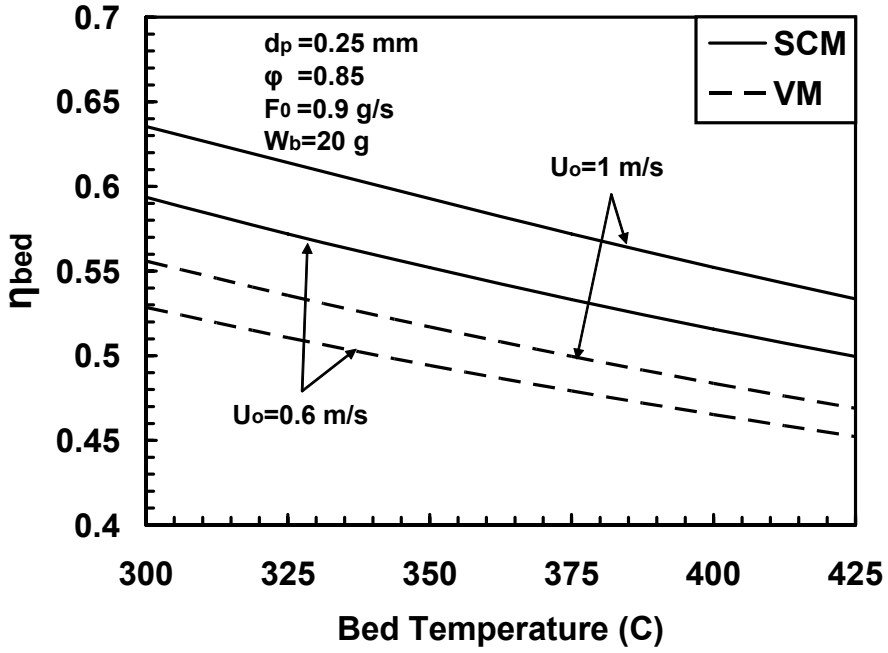

Fig. 5.35: Comparison of SCM and VM predictions, in terms of bed effectiveness versus bed temperature, within a bench-scale bed.

In summary, various parameters have been studied in hydrodynamics behaviour of a bed, where cupric chloride particles react with superheated steam. The interactions of different properties were also investigated. The results of a hydrodynamics solution algorithm have been checked by presenting the results for a bench-scale bed, as well as a full-scale bed. The influences of superficial steam velocity, bed inventory, particle diameter and spherecity on bed height at various fluidizing conditions, average bubble diameter, and bed voidage, were numerically observed. The results indicate that increasing the superficial velocity and/or bed inventory causes an increase in bed height (both at fluidization at process conditions and the minimum fluidization condition) and average bubble diameter. On the other hand, however, the bed voidage may decrease at a higher superficial velocity and/or bed inventory. Further results involve the influence of particle diameter. Increasing the solid particle diameter may result in a shorter bed height, smaller average bubble diameter and lower values for bed voidage. Interestingly, for larger particles the reductions of the above parameters are sharper. Moreover, when the particle spherecity varies, only a slight change in bed height is observed. Further results

from the hydrodynamics analysis show that the pressure drop across the bed in a full (commercial) scale fluidized bed is significant compared to the bench-scale bed.

The results were discussed and compared for two limiting cases of kinetic models. Consistent results are obtained based on each kinetic model; the outcomes are qualitatively compatible and similar. However, SCM quantitatively over-predicts the mass transport parameters discussed below, compared to VM. In some cases such as those shown in Figs. 5.29, 5.30 and 5.31, the differences between predictions of the two models are notable.

According to the computed results, as the superficial velocity increases the conversion of solid particles improves, while conversion of steam decreases. Also, when the bed inventory is higher, both reacting species conversions increase. In addition, increasing either superficial velocity or bed inventory may result in an increase of the overall rate of reaction. A notable result from these investigations that is confirmed by both kinetic models is that cupric chloride particles conversions may be increased by lowering the bed temperature, whereas steam conversion shows no significant change.

By defining a new parameter representing the bed effectiveness, from mass a transport viewpoint which reflects conversion of both reactants, the performance of the bed reactor is further examined and the effects of various parameters are monitored. According to both SCM and VM, the bed effectiveness may be increased by increasing the superficial velocity, bed inventory or lowering the bed temperature.

Chapter 6

Conclusions and Recommendations for Future Research

6.1 FINDINGS OF THIS THESIS

The major findings in this thesis are summarized below.

6.1.1 Hydrodynamics in a Fluidized Bed

The following list shows the main concluding points from the hydrodynamics of the bed.

1) When the superficial velocity increases, the bed height, average bubble diameter and mean void fraction of the bed increase.
2) A heavier bed inventory results in a taller bed height, and larger mean bubble diameter but a smaller bed voidage.

3) Increasing the solid particle diameter may result in a smaller bed height, smaller average bubble diameter and lower values for the bed voidage. Interestingly, for larger particles, the reductions of above parameters are sharper.
4) When the particle sphericity varies, a slight change in bed height is observed.
5) The pressure drop across the bed in a full (commercial) scale fluidized bed is significant, compared to the bench-scale bed.

6.1.2 Transport Phenomena in a Fluidized Bed

The Shrinking Core Model (SCM) and Volumetric Model (VM) are two extremes models that were considered as limiting cases in the current thesis. Consistent results were obtained under the assumption of each kinetic model. The main outcomes of the mass transport analysis can be summarized as follows.

1) SCM quantitatively over-predicts the mass transport parameters compared, to VM.
2) As the superficial velocity increases, the conversion of solid particles improves, while conversion of steam decreases.
3) When the bed inventory is higher, both reacting species conversions increase.
4) Increasing either the superficial velocity or bed inventory may result in an increase in the overall rate of reaction.
5) As confirmed by both kinetic models, cupric chloride particle conversions may be increased by lowering the bed temperature, whereas steam conversion shows no significant change.
6) A new parameter called the “bed effectiveness” may be increased by raising the superficial velocity, bed inventory or lowering the bed temperature.

6.2 RECOMMENDATIONS FOR FUTURE RESEARCH

The findings of this research work will be useful when assembling the fluidized bed reactor in the hydrogen production plant. The methodology presented in the thesis will be helpful in determining the optimum values for desirable bed and processes parameters which have been examined in this thesis. These optimizations are recommended for future research. Furthermore, during construction of the reactor, the predictions can be

improved by performing experimental measurements to find out the proper kinetic models, which best describe consumption of cupric chloride particles. Thus, experimental studies of fluidized bed processes are also recommended for future research. Furthermore, additional areas of recommended future research include chemical reaction rate analysis, impact of impurities, sizing models and detailed effects of pressure, temperature, and hydrodynamic properties of the bed on product yields.

References

[1] Dincer I., "Technical, Environmental and Exergetic Aspects of Hydrogen Energy Systems", *International Journal of Hydrogen Energy*, vol. 27, no. 3, 2002, pp. 265-285.

[2] Rosen M. A., “Thermodynamic comparison of hydrogen production processes”, *International Journal of Hydrogen Energy*, vol. 21, no. 5, 1996, pp. 349-365.

[3] Rosen M. A., Naterer G. F., Sadhankar R., Suppiah S., "Nuclear-based hydrogen production with a thermochemical copper-chlorine cycle and supercritical water reactor", *Canadian Hydrogen Association Workshop*, Quebec, October 19 - 20, 2006.

[4] Yildiz B., Kazimi M. S., “Efficiency of Hydrogen Production Systems using Alternative Energy Technologies”, *International Journal of Hydrogen Energy*, vol. 31, 2006, pp. 77-92.

[5] Forsberg C. W., “Hydrogen, Nuclear Energy and Advanced High-Temperature Reactor”, *International Journal of Hydrogen Energy*, vol. 28, 2003, pp. 1073-1081.

[6] Naterer G. F., "Heat Transfer in Single and Multiphase Systems", *CRC Press*, Boca Raton, FL, 2002.

[7] Forsberg C. W., "Hydrogen, nuclear energy, and the advanced high-temperature reactor", *International Journal of Hydrogen Energy*, vol. 28, 2003, pp. 1073-1081.

[8] Kasahara S., Hawang G. J., Nakajima H., Choi H. S., Onuki K., Nomura M., "Effects of process parameters of the IS process on total thermal efficiency to produce hydrogen from water", *Journal of Chemical Engineering of Japan*, vol. 36, no. 7, 2003, pp. 887-899.

[9] Kasahara S., Kubo S., Onuki K., Nomura M., "Thermal efficiency evaluation of HI synthesis/concentration procedures in the thermochemical water splitting IS process", *International Journal of Hydrogen Energy*, vol. 29, 2004, pp. 579 – 587.

[10] Nomura M.,, Fujiwara S., Ikenoya K., Kasahara S., Nakajima H., Kubo S., Hwang G. J., Choi H. S., Onuki K., "Application of an electrochemical membrane reactor to the thermochemical water splitting IS process for hydrogen production", *Journal of Membrane Science*, vol. 240, 2004, pp. 221–226.

[11] Kubo S., Nakajima H., Kasahara S., Higashi S., Masaki T., Abe H., Onuki K., "A demonstration study on a closed-cycle hydrogen production by the thermochemical water-splitting iodine–sulfur process", *Nuclear Engineering and Design*, vol. 233, 2004, pp. 347–354.

[12] Nomura M., Kasahara S., Okuda H., Nakao S. I., "Evaluation of the IS process featuring membrane techniques by total thermal efficiency", *International Journal of Hydrogen Energy*, vol. 30, 2005, pp. 1465 – 1473.

[13] Nomura M., Okuda H., Kasahara S., Nakao S. I., "Optimization of the process parameters of an electrochemical cell in the IS process", *Chemical Engineering Science*, vol. 60, 2005, pp. 7160 – 7167.

[14] Kasahara S., Onuki K., Nomura M., Nakao S. I., "Static analysis of the thermochemical hydrogen production IS process for assessment of the operation

parameters and the chemical properties", *Journal of Chemical Engineering of Japan*, vol. 39, no. 5, 2006, pp. 559-568.

[15] Sakaba N., Kasahara S., Ohashia H., Teradab A., Kubob S., Onukib K., Kunitomi K., "Hydrogen Production by using Heat from High-Temperature Gas-Cooled Reactor HTTR; HTTR-IS Plan", *Proceedings of ICAPP 06*, Reno, NV USA, June 4-8, 2006, pp. 2238-2245.

[16] Kasahara S.,, Kubo S., Hino R., Onuki K., Nomura M., Nakao S. I., "Flowsheet study of the thermochemicalwater-splitting iodine–sulfur process for effective hydrogen production", *International Journal of Hydrogen Energy*, vol. 32, 2007, pp. 489 – 496.

[17] Forsberg C. W., Peterson PER F., Pickard P. S., "Molten-salt–cooled advanced high-temperature reactor for production of hydrogen and electricity", *Nuclear Technology*, vol. 144, 2003, pp. 289-302.

[18] Yildiz B., Hohnholt K. J., Kazimi M. S., "Hydrogen production using high-temperature steam electrolysis supported by advanced gas reactors with supercritical CO_2 cycles", *Nuclear Technology*, vol. 155, 2006, pp. 1-21.

[19] Summers W. A., Gorensek M. B., "Nuclear hydrogen production based on the hybrid sulfur thermochemical process", *Proceedings of ICAPP 06*, Reno, NV USA, June 4-8, 2006, pp. 2254-2256.

[20] McLaughlin D. F., Paletta S. A., Lahoda E. J., Kriel W., "Revised capital and operating HyS hydrogen production costs', *Proceedings of ICAPP 06*, Reno, NV USA, June 4-8, 2006, pp. 2263-2269.

[21] Smith C., Beck S., Galyean W., "Separation requirements for a hydrogen production plant and high-temperature nuclear reactor", *Proceedings of ICAPP 06*, Reno, NV USA, June 4-8, 2006, pp. 2277-2286.

[22] Lewis M. A., Masin J. G., Vilim R. B., "Development of the low temperature Cu-Cl thermochemical cycle", *International Congress on Advances in Nuclear Power Plants*, Seoul, Korea, May 15-19, 2005.

[23] Park J. W., Lee Y. J., "Development of a flow net solver for HyPEP: A hydrogen production plant efficiency calculation", *Proceedings of ICAPP 06*, Reno, NV USA, June 4-8, 2006, pp. 2295-2299.

[24] Rosen M. A., Scott D. S., "Comparative efficiency assessments for a range of hydrogen production processes", *International Journal of Hydrogen Energy*, vol. 23, no. 8, 1998, pp. 653-659.

[25] Granovskii M., Dincer I., Rosen M. A., "Exergetic life cycle assessment of hydrogen production from renewables", *Journal of Power Sources*, vol. 167, no. 2, 2007, pp. 461-71.

[26] Sadhankar R. R., Li, J, Li, H., Ryland, D. K., Suppiah, S. "Future Hydrogen Production Using Nuclear Reactors", *Engineering Institute of Canada – Climate Change Technology Conference*, Ottawa, May, 2006.

[27] Lewis M., "Cu-Cl cycle R&D", *Workshop on Thermochemical Nuclear-Based Hydrogen Production*, UOIT, Oshawa, Ontario, Canada, Dec 30, 2007.

[28] Serban M., Lewis M. A., Basco J. K., "Kinetic study of the hydrogen and oxygen production reactions in the copper-chloride thermochemical cycle", *AIChE 2004 Spring National Meeting, New Orleans*, LA, April 25-29, 2004.

[29] Crowe T. C., "Multiphase flow handbook", *CRC Press*, Boca Raton, FL, 2006, Chap. 5.

[30] Basu P., "Combustion and Gasification in Fluidized Beds", *Taylor and Francis Group LLC*, Boca Raton, FL, 2006.

[31] Kunii D., Levenspiel O., "Fluidization Engineering", 2nd edition. *Butterworth-Heinemann*, London, 1991.

[32] Grace J.R., "Contacting modes and behaviour classification of gas–solid and other two-phase suspensions", *Canadian Journal of Chemical Engineering*, vol. 64, no. 3, 1986, pp. 353-363.

[33] Yang W. C., "Handbook of Fluidization and Fluid-Particle Systems", *Taylor and Francis Group LLC*, New York, 2003.

[34] Ergun S., "Fluid flow through packed columns", *Chem. Eng. Prog.*, vol. 48, 1952, pp. 89–94.

[35] Wen C.Y., Yu Y. H., "Generalized method for predicting the minimum fluidization velocity", *AIChE J.*, vol. 12, 1966, pp. 610.

[36] Mori S., Wen C. Y., "Estimation of bubble diameter in gaseous fluidized beds", *AIChE Journa*., vol. 21, no. 1, 1975, pp. 109-116.

[37] Gómez-Barea A., Ollero P., Leckner B., "Mass transport effects during measurements of gas–solid reaction kinetics in a fluidised bed", *Chemical Engineering Science*, vol. 62, 2007, pp. 1477–1493.

[38] Thompson M. L., Bi H., Grace J. R., "A generalized bubbling/turbulent fluidized-bed reactor model", *Chemical Engineering Science* vol. 54, 1999, pp. 2175-2185.

[39] Toomey R. ., Johnstone H. P., "Gaseous fluidization of solid particles", Chemical Engineering Progress, vol. 48, 1952, pp. 220–226.

[40] Davidson J. F., Harrison D., "Fluidized Particles', *Cambridge University Press*, Cambridge, 1963.

[41] Partridge B. A., Rowe P. N., "Chemical reaction in a bubbling gas-fluidised bed', *Transaction Institute of Chemical Engineers*, vol. 44, 1966, pp.T335–T348.

[42] Chavarie C., Grace J. R. , "Performance analysis of a fluidized bed reactor. II. Observed reactor behavior compared with simple two-phase models", *Industrial and Engineering Chemistry Fundamentals*, vol. 14, no. 2, 1975, pp. 79–86.

[43] Gómez-Barea A., Leckner B., Santana D., Ollero P. "Gas-solid conversion in fluidised bed reactors", *Chemical Engineering Journal*, (In press).

[44] Gómez-Barea A., Ollero P. "An approximate method for solving gas–solid non-catalytic reactions", *Chemical Engineering Science*, vol. 61, 2006, pp. 3725-3735.

[45] Larminie J., Dicks A., "Fuel Cell Systems Explained", 2nd edition, *John Wiley & Sons Ltd*., West Sussex England, 2003.

[46] http://webbook.nist.gov/chemistry/

[47] Lewis M., “Recent advances in the Cu-Cl cycle’s developments at Argon National Laboratory”, *Workshop on Thermochemical Nuclear-Based Hydrogen Production*, UOIT, Oshawa, Ontario, Canada, May 28, 2007.